



Virginia Commonwealth University
VCU Scholars Compass

Theses and Dissertations

Graduate School

2021

BISPHOSHOGLYCERATE MUTASE: A POTENTIAL TARGET FOR SICKLE CELL DISEASE

Anfal S. Aljahdali
Virginia Commonwealth University

Follow this and additional works at: <https://scholarscompass.vcu.edu/etd>

 Part of the [Medicinal and Pharmaceutical Chemistry Commons](#), and the [Medicinal-Pharmaceutical Chemistry Commons](#)

© The Author

Downloaded from

<https://scholarscompass.vcu.edu/etd/6641>

This Dissertation is brought to you for free and open access by the Graduate School at VCU Scholars Compass. It has been accepted for inclusion in Theses and Dissertations by an authorized administrator of VCU Scholars Compass. For more information, please contact libcompass@vcu.edu.

All Rights Reserved

BISPHOSHOGLYCERATE MUTASE: A POTENTIAL TARGET FOR SICKLE
CELL DISEASE

A dissertation submitted in partial fulfillment of the requirements for the degree of Doctor of
Philosophy in Medicinal Chemistry at Virginia Commonwealth University.

By

ANFAL S. ALJAHDALI,

PharmD, Faculty of Pharmacy, King Abdulaziz University, 2013

DIRECTORS: DR. MARTIN K. SAFO,

PROFESSOR, MEDICINAL CHEMISTRY

DR. YAN ZHANG,

PROFESSOR, MEDICINAL CHEMISTRY

Virginia Commonwealth University
Richmond, Virginia

May 2021

ACKNOWLEDGMENT

First and foremost, all praises to Allah, the almighty, for his blessing throughout my Ph.D. journey. I thank God for the countless blessings, knowledge, opportunities, and strength that have been showered on me to successfully complete my research project.

I would like to express my sincere gratitude to my advisor, Dr. Martin K. Safo, for giving me the opportunity to work on this novel project, the freedom to follow my own interest, and for allowing me to grow as a research scientist. I would like to express my deepest appreciation to my second advisor, Dr. Yan Zhang, for his invaluable guidance and constructive inputs throughout this research.

I am extending my heartfelt thanks to my graduate advisory committee, Dr. Darrell Peterson, Dr. Glen E. Kellogg, and Dr. Jürgen Venitz, for their insightful comments and feedback, which pushed me to better my work. Special thanks to Dr. Peterson for generously spending precious time answering all of my questions and for having his door always open for me to discuss my data. In addition, I would like to acknowledge the assistance of Dr. Abdelsattar Omar, our collaborator from King Abdulaziz University, for conducting the molecular docking and molecular dynamic simulation experiments.

Many thanks to Dr. Mohini Ghatge for teaching me the basic lab skills when I was a newbie and helping me during my assays. Thanks to Dr. Faik N. Musayev for his significant contribution to my X-ray crystallography studies. I am so thankful for all of the assistance you both have given me over the years. Your knowledge, plentiful experience, and clear instructions have helped me achieve things I could have never accomplished on my own. Many thanks should also go to my

fellow lab mates for encouraging me through the ups and downs of my academic research and daily life.

I am grateful to King Abdulaziz University for granting me the scholarship to be here. I also would like to express my gratitude to the Department of Medicinal Chemistry, Institute of Structural Biology Drug Discovery and Development, and School of Pharmacy at the Virginia Commonwealth University for giving me the opportunity to pursue my degree.

Above all, I owe a huge debt of gratitude to my family, who lived in every sense of this Ph.D. journey with me. I would have never gotten this far without their unconditional love and endless support. This Ph.D. is theirs as much as it is mine. Thanks to my Mom and Dad for all of the sacrifices that they have made on my behalf. Also, thank you for investing in educating me and always encouraging me to reach higher. I also would like to thank my sisters and brother, who have been side-by-side with me throughout the years. Thank you for believing in me when I had trouble believing in myself. Extra special thanks to my beloved daughter, Lulwa. You are my source of inspiration to achieve greatness. I love you to the moon and back.

I also appreciate the truly wonderful friends that I have been blessed with. Thank you for sticking up for me and showing me how to stick up for myself. Your motivating words and encouragement have helped me sail through tough times. You all deserve more than just a thank you.

Finally, my thanks go out to each and every person whose support, inspiration, and assistance were a milestone in completing this Ph.D.

TABLE OF CONTENTS

ACKNOWLEDGMENT.....	II
TABLE OF CONTENTS.....	IV
LIST OF TABLES	X
LIST OF FIGURES	XI
LIST OF ABBREVIATIONS.....	XVII
ABSTRACT.....	XXIII
1. INTRODUCTION	1
1.1. Erythrocyte glycolysis	1
1.2. The Rapoport-Luebering shunt	4
1.3. 2,3-Bisphosphoglycerate.....	5
1.4. Pathological role of 2,3-BPG in sickle cell disease	8
1.5. Sickle cell disease	9
1.5.1. Molecular and genetic bases of sickle cell disease	9
1.5.2. Pathophysiology and epidemiology of sickle cell disease.....	10
1.5.3. Current approved therapy of sickle cell disease	12
1.5.3.1. Hydroxyurea	12

1.5.3.2.	L-Glutamine	12
1.5.3.3.	Crizanlizumab-tmca (ADAKVEO)	13
1.5.3.4.	Voxelotor (GBT440).....	14
1.6.	Approaches to target HbS polymerization for sickle cell disease therapy	14
1.6.1.	Fetal hemoglobin synthesis.....	14
1.6.2.	Reduction of intracellular HbS concentration.....	15
1.6.3.	Blocking intermolecular contacts in the sickle polymer.....	16
1.6.4.	Increasing the oxygen affinity of Hb	18
1.6.5.	Reduction of 2,3-BPG concentration.....	20
1.7.	Bisphosphoglycerate mutase: target for sickle cell disease drug discovery	22
1.7.1.	Structure of Bisphosphoglycerate mutase.....	23
1.7.2.	Function of Bisphosphoglycerate mutase	24
1.7.3.	Proposed mechanisms of action.....	25
1.7.3.1.	BPGM synthase reaction.....	26
1.7.3.2.	BPGM phosphatase reaction.....	28
1.7.3.3.	BPGM mutase reaction	29
2.	RATIONALE, GOAL, HYPOTHESIS, AND SPECIFIC AIMS	30
2.1.	Rationale	30
2.2.	Hypothesis.....	32
2.3.	Specific Aims.....	32
3.	SPECIFIC AIM 1: Elucidate the kinetics of the synthase and phosphatase activities of BPGM and optimize the activity assays for compounds screening	34

3.1.	Specific Aim 1A: Kinetic characterization of BPGM synthase activity and optimization of the BPGM.GAPDH synthase coupled assay	35
3.2.	Specific Aim 1B: Kinetic characterization of BPGM phosphatase activity and optimization of the malachite green assay and GAPDH.PGK.BPGM coupled assay	39
3.2.1.	Kinetic characterization of BPGM phosphatase activity and optimization of the malachite green assay	39
3.2.2.	Kinetic characterization of BPGM phosphatase activity and optimization of PGK•GAPDH•BPGM coupled phosphatase assay	45
3.3.	Specific Aim 1C: Understand the activation mechanism of 2-PG on BPGM phosphatase activity using the GAPDH.PGK.BPGM coupled assay	49
3.4.	Discussion	52
3.4.1.	BPGM synthase activity	52
3.4.2.	BPGM phosphatase activity	54
3.4.3.	2-Phosphoglycolate activation mechanism of BPGM phosphatase activity	56
4.	SPECIFIC AIM 2: Pursue X-ray crystallography studies to elucidate the atomic binding of 2-PG, 2,3-BPG and/or citrate with BPGM	59
4.1.	Results	61
4.1.1.	Crystallographic study of BPGM in complex with 2,3-BPG and 2-PG ..	61
4.1.2.	Crystallographic study of BPGM in complex with 2-phosphoglycolate .	68
4.1.3.	Crystallographic study of BPGM in complex with citrate.....	75
4.1.4.	Identification of allosteric sites on BPGM surface using FTMap	81

4.2.	Discussion.....	84
4.2.1.	Overall structure comparison of the unliganded BPGM, binary BPGM•2-PG complex and ternary BPGM•3-PGA•2-PG complex.....	84
4.2.2.	Active site comparison of the unliganded BPGM and ternary BPGM•3-PGA•2-PG complex.....	87
4.2.3.	Citrate complex with BPGM.....	92
4.2.4.	Computational solvent mapping of BPGM using FTMap.....	93
5.	SPECIFIC AIM 3: Identify BPGM synthase inhibitors and/or phosphatase activators that can be used as leads for SCD drug discovery.....	94
5.1.	Specific Aim 3A: Identification of BPGM modulators against the active site.	94
5.1.1.	Pharmacophore- based virtual screening and molecular docking.....	94
5.1.2.	Machine-learning based virtual screening by <i>Atomwise</i>	98
5.1.3.	PGM1-004A.....	98
5.2.	Specific Aim 3B: Identification of BPGM allosteric modulators.....	99
5.2.1.	Molecular docking against BPGM dimer interface.....	99
5.2.2.	Molecular dynamic simulation of the top scoring docked compounds with BPGM	100
5.3.	Specific Aim 3C: Examination of the modulators effect of BPGM phosphatase and synthase activities.....	101
5.3.1.	Compound screening using malachite green assay.....	102
5.3.2.	Compound screening using PGK•GAPDH•BPGM phosphatase coupled assay	107

5.3.3.	Compound screening with GAPDH.BPGM coupled Synthase Assay ..	109
5.4.	Specific Aim 3D: Elucidate the X-ray crystallographic binding between BPGM and PGMI-004A.....	111
5.5.	Discussion.....	114
6.	SUMMARY AND CONCLUSION	118
7.	EXPERIMENTAL SECTION	122
7.1.	BPGM expression and purification:.....	122
7.2.	BPGM synthase activity:	124
7.3.	BPGM phosphatase activity:.....	125
7.3.1.	Malachite green assay	125
7.3.2.	PGK. GAPDH.BPGM coupled phosphatase assay.....	127
7.4.	X-ray crystallographic studies	129
7.4.1.	Crystallization of the ternary BPGM•3-PGA•2-PG complex structure.	129
7.4.2.	Crystallization of the binary BPGM•2-PG complex structure.....	129
7.4.3.	Crystallization of binary BPGM•Citrate complex structure	130
7.4.4.	Crystallization of BPGM in complex with PGMI-004A	131
7.5.	FTMap server	132
7.6.	Molecular modeling	132
7.6.1.	Pharmacophore based virtual screening.....	132
7.6.2.	GOLD docking.....	133
7.6.3.	Glide docking.....	133
7.6.4.	Molecular dynamic simulation	133

REFERENCES 134

VITA..... 160

LIST OF TABLES

Table 1. BPGM synthase activity and specific activity in presence and absence of 2-PG.	39
Table 2. BPGM phosphatase activity and steady-state kinetic parameters in the presence and absence of 2-PG.	43
Table 3. BPGM phosphatase activity and steady-state kinetic parameters in the presence and absence of 2-PG.	47
Table 4. Enzyme kinetic parameter of 2,3-BPG hydrolysis by BPGM phosphatase in the presence of 2-PG.	50
Table 5. Crystallization and refinement parameters of ternary BPGM•3-PGA•2-PG complex structure.	63
Table 6. Crystallization and refinement parameters of BPGM•2-PG complex structure.	70
Table 7. Crystallization and refinement parameters of BPGM•citrate complex structure.	77
Table 8. Crystallization and refinement parameters of BPGM•PGMI-004A complex.	113

LIST OF FIGURES

Figure 1. Erythrocyte glycolysis.....	3
Figure 2. Rapoport-Luebering shunt.....	5
Figure 3. (A) The oxygen dissociation curve. (B) Binding of 2,3-BPG to deoxygenated Hb.....	7
Figure 4. Model of the involvement of 2,3-BPG in SCD pathogenesis.....	9
Figure 5. Pathophysiology and epidemiology of SCD.	11
Figure 6. Hemoglobin-based anti-sickling agents. (A) Schematic representation of Hb tetramer showing the binding sites of aromatic aldehydes, thiols, and 2,3-DPG. The α and β subunits are shown in cyan and gray, respectively. (B) Schiff-base interaction between aromatic aldehyde and N-terminal α Val1 nitrogen at the α -cleft of Hb. (C) A disulfide bond between thiol and β Cys93 sulfhydryl group at the β -subunit of Hb.....	18
Figure 7. Effect of BPGM modulation in sickle cell disease.....	22
Figure 8. The Three enzymatic reactions of BPGM; synthase activity (Reaction 1), phosphatase activity (Reaction 2), mutase activity (Reaction 3).....	25
Figure 9. Mechanism of action of the BPGM synthase activity.	27
Figure 10. Mechanism of action of BPGM phosphatase activity.	29
Figure 11. (A) BPGM synthase coupled assay reactions. (B) BPGM synthase progress curve; blue line corresponds to 1,3-BPG production and black line corresponds to 2,3-BPG production.	37
Figure 12. Dependence of the synthase reaction velocity on the enzyme concentrations.	38

Figure 13. The principle of the malachite green assay.	40
Figure 14. Time-dependent of BPGM phosphatase activity in the presence and absence of 2-PG.	41
Figure 15. Linear dependence of the non-activated phosphatase reaction velocity on enzyme concentrations in the absence of 2-PG.	42
Figure 16. Linear dependence of the activated phosphatase reaction velocity on enzyme concentrations in the presence of 2-PG.	42
Figure 17. Michaelis-Menten plot of 2,3-BPG on the phosphatase reaction velocity in the absence of 2-PG.	44
Figure 18. Michaelis-Menten plot of 2,3-BPG on the phosphatase reaction velocity in the presence of 2-PG.	44
Figure 19. Linear dependence of the non-activated phosphatase reaction velocity on enzyme concentration.	46
Figure 20. Michaelis-Menten plot of 2,3-BPG on the phosphatase reaction velocity in the absence of 2-PG.	48
Figure 21. Michaelis-Menten plot of 2,3-BPG on the phosphatase velocity in the presence of 2-PG.	48
Figure 22. Michaelis-Menten nonlinear regression plot of substrate-velocity curves at five different activator concentrations.	49
Figure 23. (A) The relationship between the V_{\max} and 2-PG concentrations (B) The relationship between the apparent K_m and 2-PG concentrations (C) The relationship between the apparent k_{cat} and 2-PG concentrations.	52

Figure 24. Overall structure of BPGM with bound 3-PGA in the active site of monomer A, 2-PG in the active site of monomer B, and 2-PG at the dimer interface. 62

Figure 25. (A) Electron density map of BPGM with 3-PGA bound at monomer A active site. **(B)** Electron density map of BPGM with 2-PG bound at monomer B active site. The final $2F_o - F_c$ refined electron density map contoured at 0.8σ . Note how R116 and R100 are disordered in monomer B while ordered in monomer A. 65

Figure 26. (A) Molecular interactions of 3-PGA at the monomer A active site of BPGM. **(B)** Molecular interactions of 2-PG at the monomer B active site of BPGM. 67

Figure 27. (A) Electron density map of BPGM with 2-PG bound at the dimer interface. The final $2F_o - F_c$ refined electron density map is contoured at 0.8σ . **(B)** Molecular interactions of 2-PG at the dimer interface of BPGM. 68

Figure 28. The overall structure of BPGM in complex with 2-PG at the active sites and dimer interface. 69

Figure 29. (A) Electron density map of BPGM with bound 2-PG at the active site of monomer B. **(B)** Electron density map of BPGM with bound 2-PG at the active site of monomer A. The final $2F_o - F_c$ refined electron density map contoured at 0.8σ 72

Figure 30. (A) Molecular interactions of 2-PG at the active site of monomer A. **(B)** Molecular interactions of 2-PG at the active site of monomer B. 73

Figure 31. (A) Electron density map of BPGM with bound 2-PG at the dimer interface with final $2F_o - F_c$ refined electron density map contoured at 0.8σ . **(B)** Molecular interactions of 2-PG at the dimer interface. 75

Figure 32. The overall structure of BPGM in complex with citrate at the active site and the dimer interface. 76

Figure 33. (A) Electron density map of BPGM with bound citrate at the active site of monomer A with the final $2F_o-F_c$ refined electron density map contoured at 0.8σ . (B) Molecular interactions of citrate at the active site of BPGM. 79

Figure 34. (A) Electron density map of BPGM with bound citrate at the dimer interface of BPGM with the final $2F_o-F_c$ refined electron density map contoured at 0.8σ . (B) Molecular interactions of citrate at the dimer interface of BPGM. 80

Figure 35. FTMap output (A) Bound probe molecules to consensus sites on unliganded BPGM surface (PDB ID 3NFY); CS0 (cyan, 16 probe clusters), CS1 (magenta, 13), CS2 (yellow, 12), CS3 (wheat, 12), CS4 (white, 8), CS5 (purple, 8), and CS6 (orange, 7). (B) Contact graph for hydrogen-bond interactions (C) Contact graph for nonbonded residue interactions. 83

Figure 36. (A) Superposition of the important residues in the active site of monomer A of the ternary BPGM•3-PGA•2-PG complex (cyan) and unliganded BPGM (PDB ID 3NFY; gray) structures. (B) Superposition of the important residues in the active site of monomer A of the binary BPGM•2-PG complex (cyan) and unliganded BPGM (gray) structures. 89

Figure 37. (A) Superposition of the important residues in the active site in monomer B of the ternary BPGM•3-PGA•2-PG complex (violet) and unliganded BPGM (PDB ID 3NFY; yellow). (B) Superposition of the important residues in the active site in monomer B of the binary BPGM•2-PG complex (violet) with the unliganded BPGM structure (yellow). 91

Figure 38. Superposition of the important residues in the active site in monomer B of the binary BPGM•citrate complex (cyan) and the unliganded structure of BPGM (PDB ID 3NFY; gray). 93

Figure 39. The 3D queries on 3-phosphoglycerate. 96

Figure 40. Top hits identified from the virtual screening for the active site. 97

Figure 41. Chemical structure of PGMI-004A.	99
Figure 42. Top hits identified from the molecular docking for the allosteric site.	100
Figure 43. Protein-ligand RMSD graphs for the top-ranking compounds from the molecular dynamic simulation.	101
Figure 44. The effect of compounds 1-6, 2-PG, and 3-PGA on BPGM phosphatase activity using malachite green assay.	104
Figure 45. The effect of compounds A4-B9 on BPGM phosphatase activity using malachite green assay.	105
Figure 46. The effect of compounds B10-D5 on BPGM phosphatase activity using malachite green assay.	105
Figure 47. The effect of compounds D6-E12 on BPGM phosphatase activity using malachite green assay.	106
Figure 48. The effect of compounds F1-B11, 2-PG, and 3-PGA on BPGM phosphatase activity using malachite green assay.	106
Figure 49. The effect of compounds A5, A10, B6, C7, C8, E7, and F2 on BPGM phosphatase activity using PGK•GAPDH•BPGM phosphatase coupled assay.	108
Figure 50. The effect of compounds A5, A10, B6, C7, and C8 on BPGM synthase activity using GAPDH•BPGM synthase coupled assay.	110
Figure 51. Dose-response curve of PGMI-004A on BPGM synthase activity	110
Figure 52. Overall structure of BPGM in complex with PGMI-004.	112
Figure 53. (A) Superposition of the BPGM•PGMI-004A dimer (lime green) with the unliganded BPGM dimer (PDB ID 3NFY, light purple). (B) Superposition of the active site residues of monomer A of BPGM•PGMI-004A and the unliganded BPGM structures.	117

Figure 54. SDS-PAGE analysis of BPGM expressed in E.coli **(1)** E.coli crude extract **(2)**
Purified BPGM fractions **(3)** Molecular weight standards. 123

LIST OF ABBREVIATIONS

Å	Angstrom
°C	Degree Celsius
°	Degree
1,3-BPG	1,3-bisphosphoglycerate
2-PG	2-phosphoglycolate
2-PGA	2-phosphoglycerate
2,3-BPG	2,3-bisphosphoglycerate
2,3-DPG	2,3-diphosphoglycerate
3-PGA	3-phosphoglycerate
3D	3-dimensions
5-HMF	5-Hydroxymethyl-2-furfural
A	Absorbance
AEH	Allosteric effectors of hemoglobin
AIMS	Artificial intelligent molecular screen
Arg	Arginine
Asn	Asparagine
Asp	Aspartic acid
ATP	Adenosine Triphosphate
AU	Absorbance Unit
BPGM	Bisphosphoglycerate mutase

C-terminus	Carboxyl-terminus
Ca ²⁺	Calcium
cdB3	Band 3 membrane protein
Cl ⁻	Chloride
clogP	Partition coefficient
cm	centimeter
Cys	Cysteine
DMSO	Dimethyl sulfoxide
E. coli	Escherichia coli
EMP	Embden - Meyerhof -Parnas Pathway
Fc	Calculated structure factor
FDA	Food and drug administration
Fe ²⁺	Ferrous
Fe ³⁺	Ferric
Fo	Observed structure factor
FPLC	Fast protein liquid chromatography
FTT	Fourier transform
g	Gram
GAP	Glyceraldehyde-3-phopshate
GAPDH	Glyceraldehyde-3-phopshate dehydrogenase
Gln	Glutamine
Glu	Glutamate

GSH	Glutathione
h	hours
HA	Non-hydrogen heavy atoms
Hb	Hemoglobin
HbA	Normal adult hemoglobin
HbF	Fetal hemoglobin
HbS	Sickle hemoglobin
His	Histidine
HMP	Hexose monophosphate shunt
HU	Hydroxyurea
IC ₅₀	Half-maximal inhibitory concentration
Ile	Isoleucine
IPTG	Isopropyl β-D-1-thiogalactopyranoside
K ⁺	Potassium
k _{cat}	Catalytic constant
KCl	Potassium chloride
kDa	Kilodalton
Kg	Kilogram
KH ₂ PO ₄	Monobasic potassium phosphate
K _i	Inhibitory constant
K _m	Michaelis Menten constant
LB	Luria-Bertani

LE	Ligand efficiency
Leu	Leucine
Lys	Lysine
MD	Molecular dynamic
mg	Milligram
Mg ²⁺	Magnesium
MgCl ₂	Magnesium chloride
min	Minutes
mL	Milliliter
mM	Millimolar
mm Hg	Millimeter of mercury
mmol/l	Millimole per liter
MSCS	Multiple solvent crystal structures
NaCl	Sodium chloride
NAD	Nicotine adenine dinucleotide
NADH	Reduced nicotine adenine dinucleotide
NADPH	Nicotinamide adenine dinucleotide phosphate
nm	nanometer
NPT	Isothermal-isobaric
Ns	nanoseconds
O ₂	Oxygen
OD	Optical density

ODC	Oxygen dissociation curve
OEC	Oxygen equilibrium curve
P ₅₀	Oxygen partial pressure
PDB ID	Protein data bank identifier
PEG	Polyethylene glycol
PGAM	Phosphoglycerate mutase
PGAM1	Phosphoglycerate mutase 1
PGK	Phosphoglycerate kinase
Phe	Phenylalanine
P _i	Inorganic phosphate
PKR	Pyruvate kinase-R
pO ₂	Oxygen partial pressure
PSGL-1	P-selectin glycoprotein ligand 1
QM/MM	Quantum mechanics/molecular mechanics
RMSD	Root mean square deviation
R-state	Relaxed-state
RBCs	Red blood cells
s	seconds
S1P	Sphingosine-1-P
SCD	Sickle cell disease
SDS-PAGE	Sodium dodecyl sulfate polyacrylamide gel electrophoresis

Ser	Serine
sO ₂	Oxygen saturation of hemoglobin
SP	Standard precision
T-state	Tense-state
Thr	Threonine
Tris-HCl	Tris(hydroxymethyl)aminomethane Hydrochloride
Trp	Tryptophan
Tyr	Tyrosine
U	Unit
UV-Vis	Ultraviolet-Visible
Val	Valine
V _s	Versus
V _{max}	Maximum Velocity
α	Alpha
β	Beta
γ	Gamma
ε	Epsilon
ΔG	Free energy
μM	Micromolar

Abstract**BISPHOSHOGLYCERATE MUTASE: A POTENTIAL TARGET FOR SICKLE
CELL DISEASE**

By Anfal S. Aljahdali, Ph.D.

A dissertation submitted in partial fulfillment of the requirements for the degree of Doctor of
Philosophy in Medicinal Chemistry at Virginia Commonwealth University.

Virginia Commonwealth University, 2021.

Directors: Dr. Martin K. Safo

Professor, Department of Medicinal Chemistry

Dr. Yan Zhang

Professor, Department of Medicinal Chemistry

Bisphosphoglycerate mutase (BPGM) is a part of the erythrocyte glycolysis system. Specifically, it is a central enzyme in the Rapoport-Leubering pathway, a side glycolytic pathway involved in the regulation of the concentration of the natural allosteric effector of hemoglobin (Hb), 2,3-bisphosphoglycerate (2,3-BPG). BPGM catalyses the synthesis and hydrolysis of 2,3-BPG through its synthase and phosphatase activities. The synthase activity is the main role of BPGM, while the phosphatase activity is low and is activated by the physiological effector, 2-phosphoglycolate (2-PG) with the latter mechanism poorly understood.

BPGM activity and 2,3-BPG levels in red blood cells (RBCs) have a significant role in sickle cell disease (SCD) pathology. SCD patients experience a constant state of hypoxia that results in increasing the level of 2,3-BPG as a compensatory mechanism to enhance oxygen delivery to tissues. However, the abnormal increase in 2,3-BPG in RBCs of SCD patients exacerbates the disease's primary pathophysiology, which is the hypoxia-driven deoxygenated-sickle hemoglobin (HbS) polymerization, that in turn leads to RBCs sickling and consequent numerous downstream multi-organ adverse effects.

Reducing the levels of 2,3-BPG by activating BPGM phosphatase activity using 2-PG has been proposed as a potential therapeutic approach for SCD as 2-PG was found to have an anti-sickling property. Nonetheless, the actual activation mechanism of 2-PG on the phosphatase activity or the binding mode of 2-PG to BPGM is not clear. Moreover, no drug screening studies have been performed to identify small molecules against BPGM for therapeutic purposes.

The objectives of this project are to characterize the steady-state kinetics of BPGM synthase and phosphatase activities, understand the mechanism of phosphatase activation, and elucidate the atomic interaction of BPGM with 2-PG and other effectors such as citrate that can provide valuable insight into their mechanism of actions and provide a framework for developing small molecules with potential SCD therapeutic benefit. In addition, we aim to identify ligands that modulate either BPGM phosphatase and/or synthase activity to reduce 2,3-BPG concentration in RBCs.

First, the steady-state kinetics of BPGM synthase and phosphatase activities were characterized using the previously reported coupled spectrophotometric synthase and phosphatase activities assays. These assays were also optimized for drug screening experiments. Both assays

have limitations and proved challenging for drug screening. We also employed the colorimetric malachite green assay to study BPGM phosphatase activity, as well as for compound screening.

Next, we elucidated the mechanism of phosphatase activity activation by 2-PG using kinetic and X-ray crystallography studies. The kinetic study showed the mechanism of 2-PG activation of BPGM to be mixed-type of noncompetitive and competitive, suggesting the binding of 2-PG to the active site and to an allosteric or non-catalytic site of the enzyme. The crystal structures of BPGM with 2-PG in the presence and absence of the substrate 2,3-BPG showed binding of the 2-PG and/or 3-PGA (the reaction product of 2,3-BPG) at the expected active site, and at a novel non-catalytic site at the dimer interface, in agreement with the kinetic analysis. The structural studies of BPGM also showed conformational nonequivalence of the two monomeric active sites: one site in a close catalytic conformation, and the second site in an open conformation, with the residues at the entrance of the active site, including Arg100, Arg116, and Arg117, and the C-terminus region disordered, which we propose to be induced by the dimer interface binding.

In order to gain further insight into the BPGM mechanism of action, we also co-crystallized BPGM with citrate, a known BPGM phosphatase inhibitor. The co-crystal structure of BPGM with citrate showed citrate binding to only one of the dimer active sites and to the dimer interface. The kinetic and crystallographic findings suggest for the first time an allostereism or cooperativity across monomers, in which the binding of a ligand at the dimer interface induces negative cooperativity affecting the affinity of ligand binding at the second active site. In the BPGM•citrate binary complex, an extreme form of negative cooperativity, where half of the site reactivity is observed, shows that only one active site appears to be functional.

Toward the objective of identifying small molecules modulators of BPGM activity for therapeutic purposes, we identified several compounds that target the active site of BPGM using

(1) *in-house* pharmacophore-based virtual screening and molecular docking; (2) machine learning-based molecular screening in collaboration with the pharmaceutical company *Atomwise*, and (3) PGM1-004A, a known inhibitor of the homologous enzyme, phosphoglycerate mutase 1 (PGAM1). The compounds were tested for their effect on BPGM synthase and phosphatase activities. Unfortunately, the compounds did not show any modulation except for PGMI-004A, which shows a dose-dependent synthase inhibition with IC_{50} ($50 \pm 11 \mu\text{M}$). Several attempts were made to co-crystallize BPGM with PGMI-004A but were unsuccessful. The novel allosteric site at the dimer interface was also docked against a library of compounds, which identified several potential binders. The top-scoring compounds will be obtained and tested in the near future.

CHAPTER 1

1. INTRODUCTION

1.1. Erythrocyte glycolysis

The major role of an erythrocytes or red blood cell (RBC) during its 120 days life span is to transport oxygen (O_2) from the lungs to the body tissues and deliver carbon dioxide from the tissues back to the lungs as a waste product.¹ RBCs need the energy to maintain their cellular function. The main source of RBC's energy is through anaerobic glycolysis since it lacks the intracellular organelles such as nucleus and mitochondria.^{1,2}

Glucose is consumed through the Embden-Meyerhof-Parnas (EMP) pathway and hexose monophosphate shunt (HMP), which depend on the different O_2 tensions between the lungs and the tissues (Figure 1).^{1,3} In the lung, high O_2 tension leads to a release of high O_2 reactive species, putting the RBCs in oxidative stress. Consequently, the glycolysis diverts into the HMP shunt at the Glucose-6-phosphate step of the EMP pathway to generate nicotinamide adenine dinucleotide phosphate (NADPH), which in turn generates a reduced form of glutathione (GSH) to protect RBCs from oxidative stress (Figure 1). Also, during glycolysis, a reduced form of nicotinamide adenine dinucleotide (NADH) is generated at the glyceraldehyde 3-phosphate dehydrogenase (GAPDH) step of the EMP pathway to help maintain RBCs in the reduced state, as the high O_2 reactive species will oxidize the hemoglobin (Hb) bound iron from the ferrous state (Fe^{2+}) to the ferric state (Fe^{3+}), forming methemoglobin. Methemoglobin lacks the ability to perform the normal function of Hb, which is carrying O_2 to the tissues. Thus, NADH functions to reduce Fe^{3+} back to Fe^{2+} state, restoring the normal function of Hb.

In contrast, in tissues where O₂ tension is low, glucose is consumed mainly via the EMP pathway, in which glucose is converted into lactate leading to the production of high energy phosphate compounds, adenosine triphosphate (ATP), and NADH (Figure 1).⁴ In addition, the glycolytic metabolite, 1,3-bisphosphoglycerate (1,3-BPG), bypasses the ATP producing step and shunt into a side pathway called the Rapoport-Luebering pathway to synthesize 2,3-bisphosphoglycerate (2,3-BPG), which is a potent allosteric effector of Hb that is responsible for decreasing the affinity of Hb for O₂, facilitating the unloading of O₂ to tissues (Figure 1).

It should be noted that erythrocyte glycolysis is limited by the availability of the main glycolytic enzymes in the cytosol. Under normal O₂ tension, all the main glycolytic enzymes such as GAPDH, aldolase, phosphofructokinase, pyruvate kinase, and lactate dehydrogenase form a complex with the Band 3 membrane protein (cdB3) in the RBCs membrane, rendering the enzymes inactive. However, in low O₂ tension, deoxygenated Hb binds to cdB3, displacing the glycolytic enzymes, and releasing them into the cytosol, thereby activating glycolysis.³

Erythrocyte Glycolysis

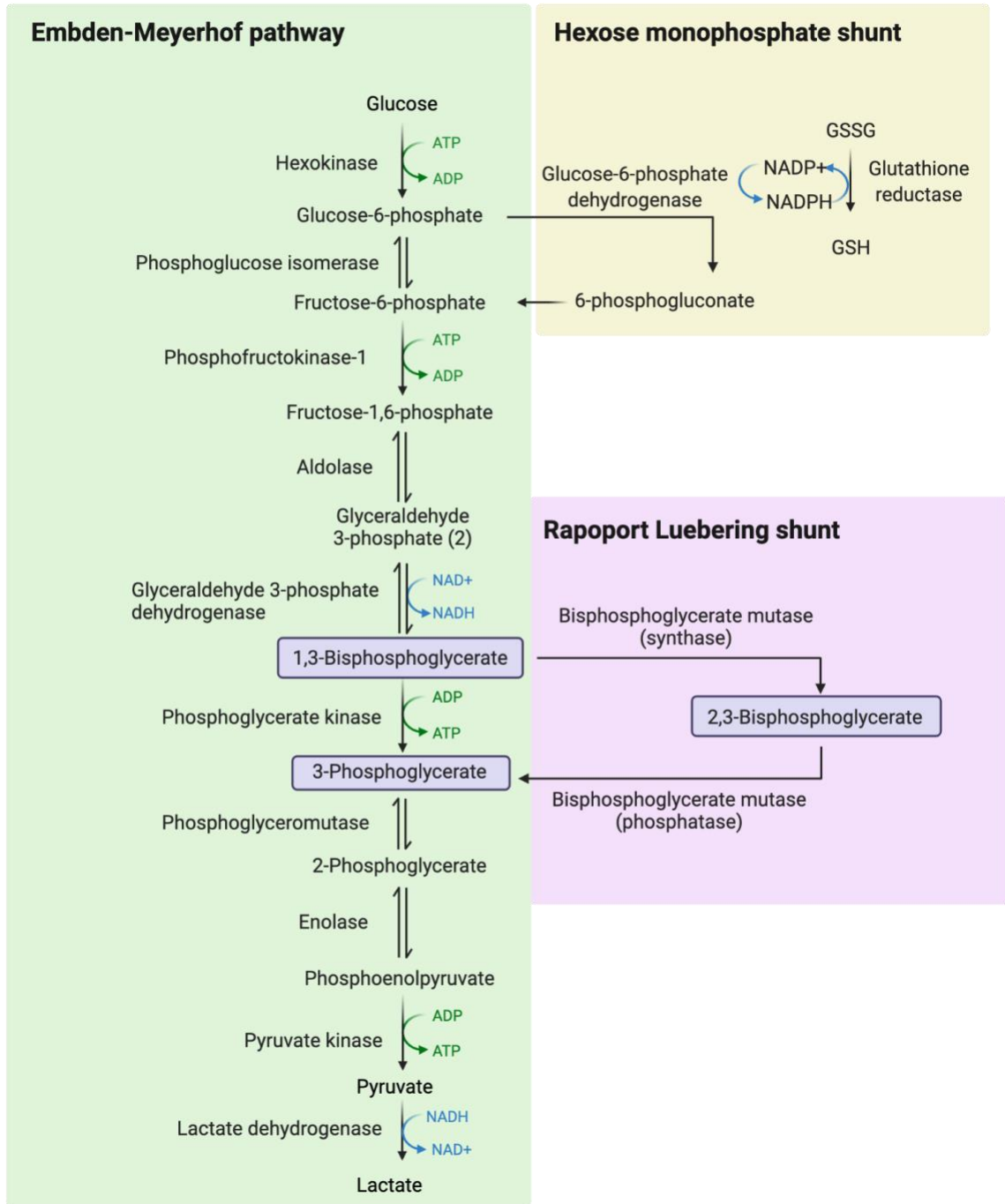


Figure 1. Erythrocyte glycolysis.

1.2. The Rapoport-Luebering shunt

The Rapoport-Luebering shunt (also known as Bisphosphoglycerate shunt) is a side biochemical pathway that was first described by Samuel Mitja Rapoport and his assistant Jane Luebering in 1952.^{5,6} This side shunt is exclusive to mammalian RBCs and placenta and is regulated by a single erythrocyte specific multifunctional enzyme, bisphosphoglycerate mutase (BPGM).⁷ The reactions catalyzed in this pathway involve converting the glycolytic intermediate, 1,3-BPG, to its isomer 2,3-BPG, followed by conversion of 2,3-BPG to 3-phosphoglycerate (3-PGA) in the EMP glycolytic pathway (Figures 1 and 2).⁷⁻⁹

At normal O₂ saturation level, RBC glycolytic activity is balanced between ATP generation to maintain cellular energy requirements and 2,3-BPG production for modulating the oxygenation/deoxygenation status of Hb. However, in some instances, such as hypoxemia, low O₂ tension activates glycolysis, which in turn increases the synthesis of 1,3-BPG, resulting in increased production of 2,3-BPG in the erythrocyte. This adaptation mechanism influences the efficiency of O₂ dissociation from hemoglobin and optimizes O₂ delivery to tissues.

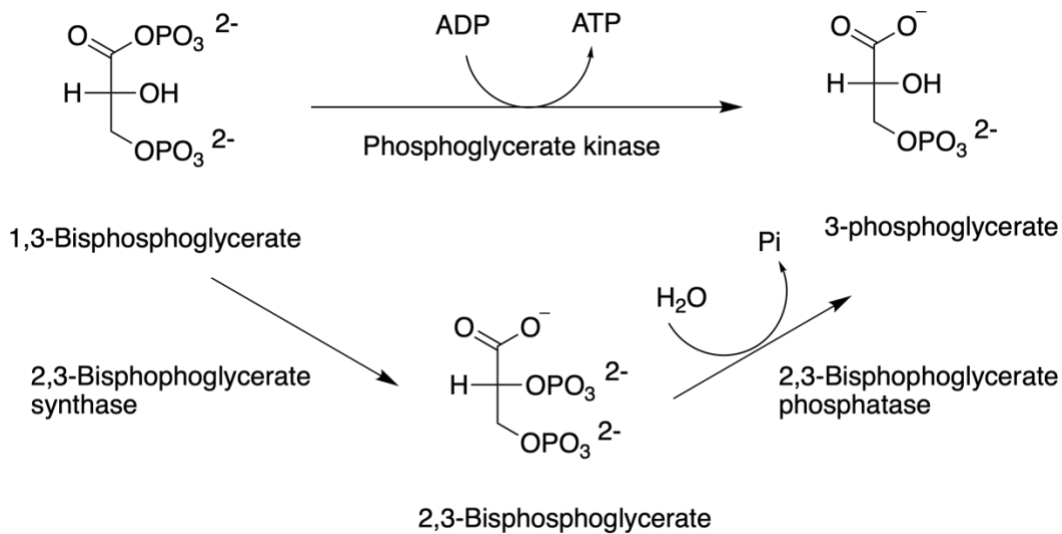


Figure 2. Rapoport-Luebering shunt.

1.3. 2,3-Bisphosphoglycerate

2,3-BPG, also known as 2,3-diphosphoglycerate (2,3-DPG), is an organic phosphate compound and was first identified by Greenwald in 1925 as a normal constituent in mammalian erythrocytes.¹⁰ The physiological function of 2,3-BPG was determined 40 years later by the Sutherland research group to be a cofactor for phosphoglycerate mutase 1 (PGAM1), a glycolytic enzyme that catalyzes the interconversion of 3-PGA to 2-phosphoglycerate (2-PGA) in the cellular glycolysis.¹¹ Later, a second physiological function of 2,3-BPG was identified to be an allosteric regulator of Hb to facilitate the release of bound O₂ from Hb to tissues.¹²⁻¹⁴ 2,3-BPG exists in the RBCs with an equimolar concentration to Hb, approximately 5 mmol/L.¹⁵

Hb is a tetrameric allosteric protein, which undergoes different conformational changes during the oxygenation and deoxygenation processes to allow binding and releasing of O₂,

respectively. The two main conformational states of Hb are the T (tense) state, which possesses a low O₂ affinity (aka deoxygenated Hb), and the R (relaxed) state, which is a high affinity state (aka oxygenated Hb). The R-state is an ensemble of several conformational states, including the R2, R3, RR2, RR3, and the classical R.^{16,17}

The allosteric effect of 2,3-BPG on Hb oxygen affinity is represented by the oxygen dissociation curve (ODC) or the oxygen equilibrium curve (OEC) (Figure 3). This curve plots the percent of O₂ saturation of hemoglobin (sO₂) against the O₂ partial pressure in the blood (pO₂). The PO₂ at 50% sO₂ is expressed as P₅₀ and measures the O₂-affinity for Hb. The curve is sigmoidal in shape due to the cooperative binding of O₂ to Hb, meaning that the binding of one molecule of O₂ to one subunit of Hb tetramers facilitates the binding of O₂ to the other subunits. The position of the curve determines the affinity of O₂ to oxygen. If the affinity of Hb to O₂ is increased, the OEC is shifted to the left, and the P₅₀ value is decreased from the normal value of 26-27 mmHg PO₂ (Figure 3). If the affinity of hemoglobin to O₂ decreased, the P₅₀ value is increased, and the OEC is shifted to the right. 2,3-BPG stabilizes the T-state conformation of Hb by binding to the central water cavity between the two β-globin chains (Figure 3). Unlike oxygenated Hb, the β-cleft is more accessible to 2,3-BPG in the deoxygenated Hb; thereby, 2,3-BPG preferentially binds to deoxygenated Hb to stabilize the T-state. This causes a right shift of the OEC, decreasing Hb affinity for O₂ (i.e., increasing P₅₀) and increasing the release of O₂ to tissues.^{13,18-20} During the T-to-R transition, the pocket becomes smaller, and 2,3-BPG is expelled, allowing Hb to easily transition to the high-O₂ affinity R-state that easily binds oxygen.

1.4. Pathological role of 2,3-BPG in sickle cell disease

The production of 2,3-BPG is increased during hypoxia and/or low O₂ tension conditions, such as high altitude, respiratory distress, congestive heart disease, ischemia, and sickle cell disease (SCD). The increase in 2,3-BPG level is a compensatory adaptation mechanism that facilitates the release of O₂ from Hb to tissues that need O₂ the most. In SCD, 2,3-BPG is abnormally high, presumably due to chronic hypoxia.²¹ The high 2,3-BPG concentration of RBCs increases the proportion of the deoxygenated sickle Hb (HbS), which causes the primary pathophysiology of SCD by inducing HbS polymerization and the concomitant RBCs sickling.²²

On a molecular level, during the hypoxic condition, 2,3-BPG, in conjunction with sphingosine-1-P (S1P), an intracellular hypoxia-responsive biolipid, binds to deoxygenated HbS, forming a ternary complex that has been suggested to promote anchoring of deoxygenated HbS to the RBCs membrane protein, cdB3, displacing the glycolytic enzymes (Figure 4).²³⁻²⁵ The release of the main glycolytic enzyme GAPDH from cdB3 protein to the cytosol activates glycolysis through the EMP pathway and suppresses the HMP shunt, resulting in enhancement of 2,3-BPG production with a concomitant increase in oxidative stress, as well as increased concentration of deoxygenated HbS,^{23,25} thereby, worsening HbS polymerization and RBCs sickling.

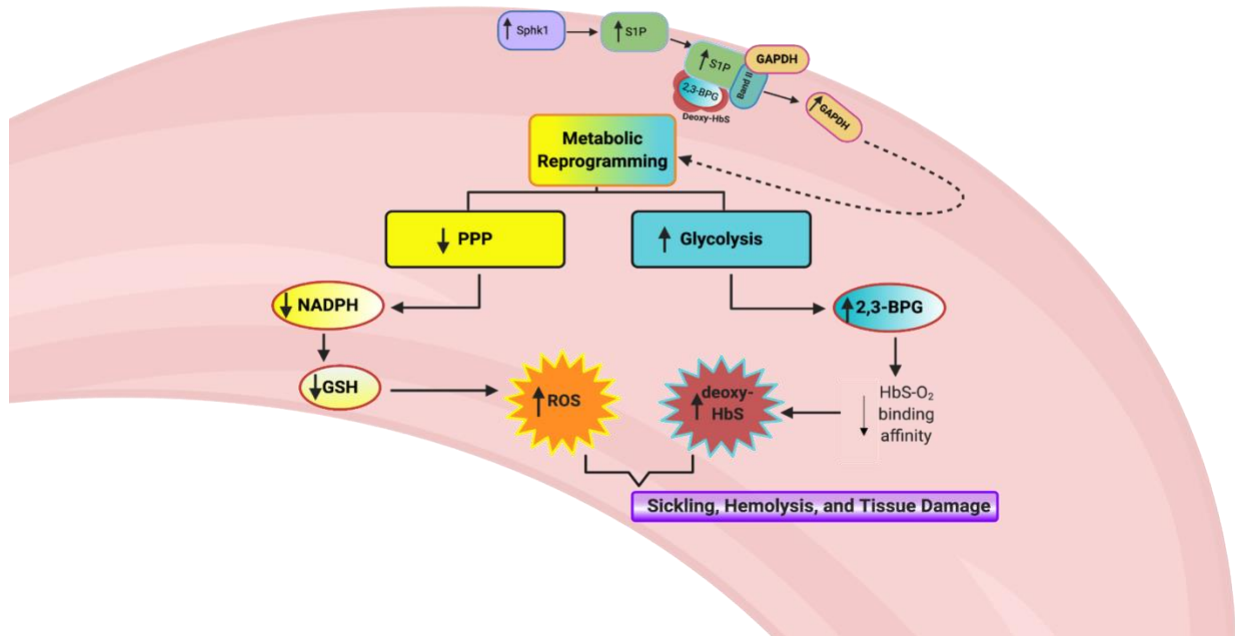


Figure 4. Model of the involvement of 2,3-BPG in SCD pathogenesis.

1.5. Sickle cell disease

1.5.1. Molecular and genetic bases of sickle cell disease

SCD is a hereditary hematological disorder caused by a single base-pair point mutation at the sixth position of the Hb β -globin gene, resulting in the expression of dysfunctional HbS. In HbS, the hydrophilic glutamic acid residue at the surface of the β subunit (β Glu6) is mutated to the hydrophobic Valine residue (β Val6).^{26,27} Under normal O₂ saturation levels, both Hb and HbS have an identical structure.^{28,29} However, during the hypoxic state, when HbS is deoxygenated, the side-chain of the mutated β Val6 of a Hb tetramer protrudes out to form intermolecular contacts with the hydrophobic acceptor pocket (β_2 Ala70, β_2 Phe85, and β_2 Leu88) of an adjacent

deoxygenated HbS to form a polymer,^{26,28–31} leading to the formation of long, rigid, and insoluble 14 stranded fibers.^{26,30,32–36} The fiber integrity is further stabilized by secondary interactions with adjacent HbS polymers, distorting the shape of RBCs from flexible biconcave disc cells into rigid crescent sickle-shaped cells (Figure 5).^{26,27}

1.5.2. Pathophysiology and epidemiology of sickle cell disease

SCD has a complex pathophysiology that involves nearly all organ systems. Hypoxia-induced HbS polymerization is the hallmark of the disease and represents the primary pathophysiological events that lead to subsequent secondary adverse effects (Figure 5).³⁷ HbS undergo multiple cycles of deoxygenation-induced polymerization and reoxygenation-induced depolymerization resulting in the formation of irreversibly sickled RBCs, and subsequently the initiation and propagation of downstream pathophysiological cascades, including deformability of RBCs into crescent shape, dehydration of sickled RBCs,³⁸ and damage of the sickled RBC's membranes.^{27,39} The damaged RBCs membranes release free Hb to the plasma leading to secretion of pro-inflammatory and adhesive cytokines, activation of the coagulation system,⁴⁰ and depletion of nitric oxide level,⁴¹ which facilitate vaso-occlusion events. Recurrent vaso-occlusion episodes can be manifested as serious complications, such as acute chest syndrome, leg ulcers, priapism, painful crisis, and multi-organ damage or death (Figure 5).^{42,43}

SCD is a global public health burden affecting over 100,000 people in the US, most of whom are African-Americans and, to a lesser degree, Hispanic-Americans, and over 15 million people worldwide.⁴⁴ The number of affected people is expected to increase by 30% by 2050.⁴⁵ Individuals with SCD experience 20-30 years shorter life expectancy than people without SCD.^{43,44} In addition, SCD presents an economic burden with estimated annual lifetime costs of more than \$1 million per patient in the US alone (Figure 5).

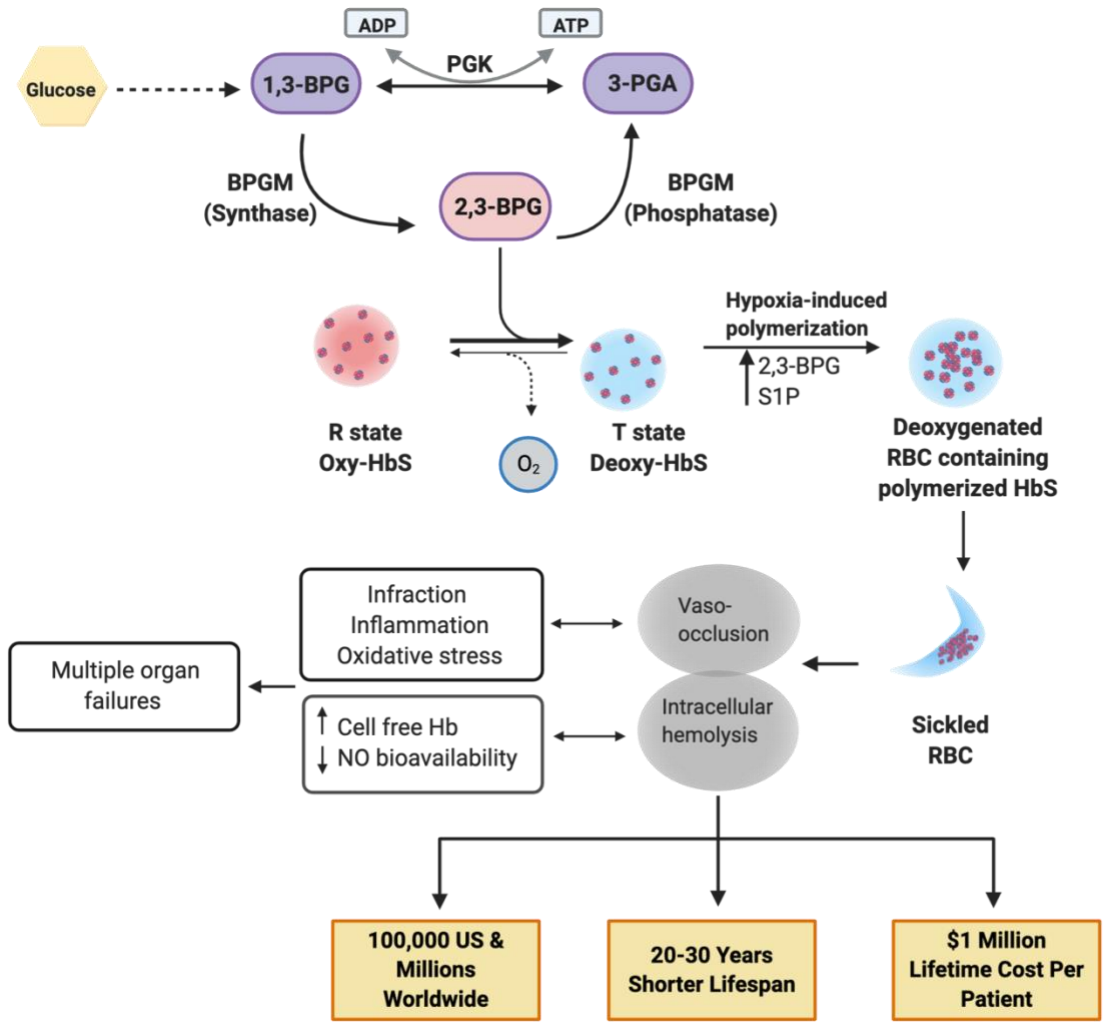


Figure 5. Pathophysiology and epidemiology of SCD.

1.5.3. Current approved therapy of sickle cell disease

Currently, four drugs have been approved by the FDA for the management of SCD. These include Hydroxyurea,⁴⁸ L-glutamine,⁴⁹ Crizanlizumab-tmca,⁵⁰ and Voxelotor.⁵¹ The approved drugs work by targeting multiple critical points in the pathophysiology of SCD.

1.5.3.1. Hydroxyurea

Hydroxyurea (HU) is the first drug approved by the FDA for the treatment of SCD. It has been the standard and ideal therapeutic agent since its approval in 1998.⁴⁸ HU was originally developed as an antineoplastic agent to treat myeloproliferative disorder. Later, it was found to activate the production of fetal Hb (HbF), which does not polymerize, by inducing stress erythropoiesis.⁵² HbF has a higher affinity to O₂ compared to HbS. Therefore, increasing the concentration of HbF will delay the HbS polymerization process and increase the solubility of sickled RBCs.⁵³ HU can also activate the synthesis of HbF through other mechanisms, such as acting as a nitric oxide donor that results in an enhancement of cellular cyclic guanosine monophosphate level and activation of protein kinase, which ultimately induces HbF production.^{54,55} Additionally, HU was found to reduce inflammation, improves red cell rheology, reduces adhesion and hemolysis of sickled RBCs.^{48,56} Despite its activity on multiple pathways, as well as its clinical efficacy in both children and adults, HU exhibits a variation in SCD patients' responses, and some patients have been reported to be refractory to HU therapy.⁵⁷ Also, the reported poor compliance and the serious side effects such as myelosuppression tend to limit its use.⁴⁸

1.5.3.2. L-Glutamine

The second approved therapy is L-glutamine (Endari), which is a precursor of GSH and NAD. L-glutamine acts as an antioxidant, increasing the intracellular level of glutamine and

enhancing the synthesis of NADH level to neutralize the oxidative stress in sickle RBCs.^{58,59} The mechanism of action of L-glutamine only involves reduction of oxidative stress, and it has no effect on HbS polymerization.^{58,60,61} In a multicenter, randomized, double-blind, phase III trial, results demonstrated that oral L-glutamine supplementation twice daily at 0.3 g/kg dose for a total of 48 weeks decrease the pain crises in adults and children over 5 years with SCD.^{62,63} L-glutamine was approved by the FDA in 2017 for acute complication of SCD in both adult and pediatric patients older than 5 years.^{49,64} Nonetheless, the European regulatory body recommended against approval of the medication due to limited evidence of efficacy in phase III trials.^{65,66}

1.5.3.3. Crizanlizumab-tmca (ADAKVEO)

Crizanlizumab-tmca is a humanized monoclonal antibody against the adhesion molecule P-selectin. P-selectin lies on the surface of activated endothelium and platelets, and contributes to the pathophysiology of SCD by initiating the vaso-occlusion process through promoting the adhesion of leukocytes to the endothelium and platelets via P-selectin glycoprotein ligand 1 (PSGL-1).^{67,68} The anti-adhesive mechanism of crizanlizumab is through inhibiting the interaction between P-selectin and PSGL-1, thereby increasing the blood flow and reducing vaso-occlusion. Crizanlizumab has been shown to decrease the frequency of painful vaso-occlusive crises of SCD patients in clinical trials from 2.98 per year (with placebo) to 1.63 per year in treated SCD patients, a 45% overall decrease.^{69,70} It was approved by the FDA as an intravascular infusion to reduce the frequency of vaso-occlusive events in adults and children with SCD.⁵⁰ However, it is unclear if this level of vaso-occlusive crises reduction (~1 per year) is sufficient to improve quality of life, and the durability of long-term outcomes is uncertain. In addition, monoclonal antibodies are expensive to produce and require monthly visits to an infusion clinic, which may limit patient acceptance.

1.5.3.4. Voxelotor (GBT440)

Voxelotor (GBT440) is a Hb allosteric effector that inhibits the HbS polymerization by forming a Schiff-base interaction with the α Val1 amine of HbS, stabilizing the non-polymer forming R-state Hb, thereby increasing Hb O₂ affinity with concomitant anti-sickling effect.^{51,71–74} Voxelotor has been demonstrated to prolong RBCs half-life, delay HbS polymerization, and inhibit RBCs sickling in sickle mice model and human.^{75,76} Voxelotor was approved by the FDA in 2019 for adults and pediatric patients of 12 years of age and older with sickle cell disease.^{51,75,77,78} Voxelotor is the only approved drug that directly acts to interfere with the HbS polymerization process.⁷² FDA approval of Voxelotor for SCD was based on increased Hb levels and reduced hemolysis in the HOPE trial and has yet to show significance on vaso-occlusion.

1.6. Approaches to target HbS polymerization for sickle cell disease therapy

The need for new and more effective therapy for SCD is high. Several research efforts have been made or ongoing to explore different therapeutic approaches aimed to develop anti-HbS polymerization agents. Among them are (1) HbF synthesis, (2) reduction of intracellular HbS concentration, (3) blocking intermolecular contacts in the sickle polymer, (4) increase O₂ affinity of Hb, and (5) reduction of 2,3-BPG concentration.

1.6.1. Fetal hemoglobin synthesis

HbF, a predominant form of Hb in fetal life, is a tetramer composed of two α -globin chains and two γ -globin chains ($\alpha_2\gamma_2$). HbF binds to O₂ with greater affinity than normal adult Hb (HbA; $\alpha_2\beta_2$), facilitating O₂ uptake by the fetus in the womb. After birth, γ -globin gene expression is

silenced and gradually replaced by β globin to produce HbA.⁷⁹ The beneficial role of elevated HbF level in sickle cell disease patients was recognized in 1948 by pediatrician Janet Watson as she observed the lack of SCD clinical complications in children in their first year.⁸⁰ Also, it was observed that SCD patients, who carry a ‘hereditary persistence of fetal Hb’ gene, which is a condition in which the RBCs have an increased amount of HbF than normal RBCs, have mild symptoms, and they are less prone to sickle cell crises due to persistent γ -globin expression through their adulthood.⁸¹ These observations, along with other biochemical studies that reported the benefits of HbF in delaying the polymerization and improving the solubility of HbS, led to the utilization of this approach as a therapeutic strategy for SCD treatment.⁵³ HbF induction appears to form hybrid heterotetramers with Hb S ($\alpha_2\beta^s\gamma$) that lack the ability to incorporate into the HbS polymer and thus reducing HbS polymerization.⁸² A number of agents have been reported to induce HbF synthesis via their cytotoxic effect and epigenetic regulatory enzyme modification. The cytotoxic agent, HU, is the typical HbF inducing agent and was the first drug approved for the treatment of SCD.⁴⁸ Epigenetic enzymes modulators have been investigated as an alternative means to treatment with HU.^{83,84} The mechanism of action for HbF induction include reactivating γ globin gene expression through inhibiting enzymes involved in HbF gene silencing. These enzymes are DNA methyltransferase-1,⁸⁵⁻⁸⁷ histone deacetylase,⁸⁸⁻⁹⁵ and lysine demethylase-1.⁹⁶⁻¹⁰¹ A number of these enzymes’ inhibitors have shown to increase γ -globin expression in vitro, in vivo and are under clinical trial for the treatment of SCD.¹⁰²⁻¹⁰⁵

1.6.2. Reduction of intracellular HbS concentration

Studying the kinetics of hypoxia-induced HbS polymerization showed that HbS experiences a delayed time until it polymerizes. This delayed time is strongly dependent on the intracellular concentration of HbS. Therefore, a small reduction of HbS concentration can lead to

potential improvement of HbS polymerization.^{38,106} One of the strategies to reduce the intracellular concentration of HbS is by improving sickled RBCs hydration status through targeting the membrane ion exchange channels, such as Gardose channels and/ or K-Cl cotransporter.¹⁰⁷ The activation of the membrane ion transporter in SCD increases the level of Ca^{2+} in sickled RBCs resulting in the activation of the Gardose pathway, which is Ca^{2+} activated K^+ channel. The activation will affect the permeability of the transport system resulting in the efflux of K^+ and Cl^- along with loss of water.¹⁰⁸⁻¹¹¹ Gardose pathways can be inhibited through several compound, such as clotrimazole, a known antifungal agent. Studies with clotrimazole showed improvement in sickled RBCs hydration. Nevertheless, the clinical study was terminated because of dose-dependent toxicity.^{111,112} Senicapoc, a novel Gardose channel blocker, improved sickled RBCs hydration and reduced hemolysis.^{113,114} However, despite its efficacy, the clinical study was terminated due to a lack of improvement in the frequency of vaso-occlusive crises in SCD patients.¹¹⁵ Inhibition of KCl cotransporter has been achieved with a divalent cation, and increasing intraerythrocytic Mg^{2+} content with Magnesium pidolate is under investigation as an SCD therapy, either alone or in combination with HU.^{116,117}

1.6.3. Blocking intermolecular contacts in the sickle polymer

The polymerization of HbS is triggered by the single amino acid mutation on the surface of β subunit ($\beta 6\text{Glu} \rightarrow \beta 6\text{Val}$) via primary interactions between $\beta 6\text{Val}$ of one HbS molecule and a hydrophobic pocket of a proximate HbS molecule. The polymer is further stabilized by several secondary contacts.^{28,29,31,33,118} The molecular details of the fiber structure using X-ray crystallography and light electron microscopy have led to the identification of the residues located on the HbS surface that participate in the secondary polymer interactions.^{34,119,120} It has been observed that the Hb variant Stanleyville II ($\alpha\text{Asn78} \rightarrow \alpha\text{Lys78}$) increases HbS solubility and

prevents HbS polymerization, resulting in a benign disease state.^{28,29,31,33,36,118} This observation and others show that the abrogation of the secondary interpolymer contacts can lead to alleviation of SCD symptoms. The disruption of the interpolymer secondary interactions by non-covalent inhibitors has been studied as routes to develop potential therapeutic agents for SCD. These inhibitors include alkyl urea,^{121–123} dichloromethane,¹²⁴ aromatic amino acids, such as tryptophan, phenylalanine, and phenylalanine and their derivatives.^{125–128} However, none of these compounds showed promising results. The major drawback of this approach is that a high concentration of drugs is required to bind non-covalently to HbS and/or also these compounds lack specificity. Moreover, the interaction sites on the HbS surface are flat with no deep pockets in which compounds can tightly bind.¹²⁹

Also, efforts have been made to design peptide-based inhibitors targeting the primary intermolecular polymer contacts, which include the N-terminal segments of the β -globin chain of Hb (β Phe85/ β Leu88 or/and β 4Thr– β '73Asp). These peptide inhibitors have been shown to inhibit HbS polymerization and improve the gelation of HbS. They overcame the challenges presented with the flat surface of HbS as they can mimic the protein surface and interfere with the polymer contacts.^{130–132} However, challenges remain, especially with respect to the high concentration of compound required to reach the polymerization inhibitory potential.

Efforts are currently ongoing by several investigators to use covalent modifiers of Hb to overcome the weak interactions of the non-covalent binders. Some of the compounds include aromatic aldehydes, thiols, isothiocyanates, etc.^{21,133}

1.6.4. Increasing the oxygen affinity of Hb

Increasing the O₂ affinity of HbS by covalent Hb allosteric effectors (AEH) has been shown to be a viable strategy for inhibiting the hypoxia-induced HbS polymerization and preventing RBCs sickling. Stabilization of the non-polymer forming R-state Hb by AEHs shifts the OEC to the left, inducing an allosteric conformational change to produce Hb with high-affinity to O₂ that is resistant to polymerization. In contrast, stabilization of T-state by other class of AEHs shifts the OEC to the right, producing low-affinity Hb that readily releases O₂ to the tissues. Such compounds obviously are not useful for treating SCD.

Different classes of AEH have been investigated and studied for their anti-sickling properties, such as aromatic aldehydes, isothiocyanates, thiols, azolylacryloyl derivatives, and ethacrynic acid derivatives.^{21,133,134} The most promising anti-sickling agents are the R-state stabilizing aromatic aldehydes that bind to the α -cleft of the central water cavity of Hb and the T-state destabilizing thiols that predominantly bind to the β -cleft on the surface of the Hb molecule (Figure 6).

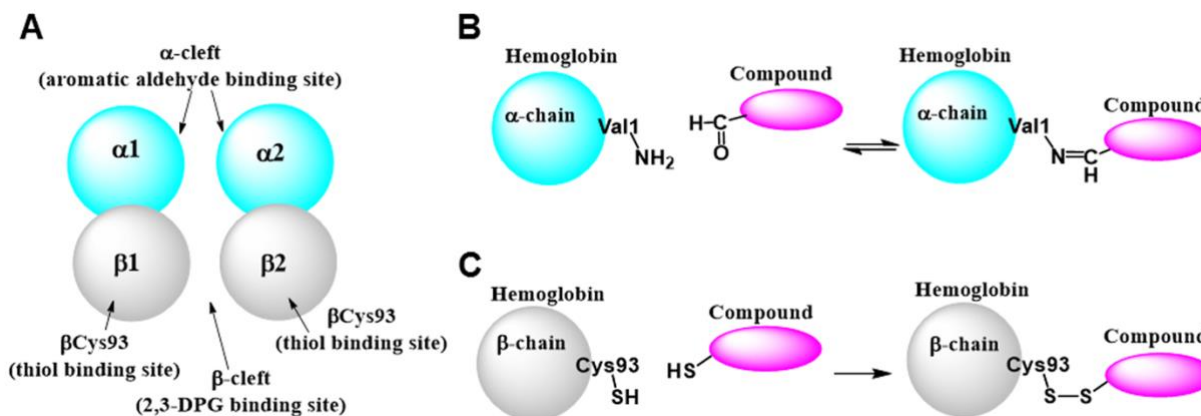


Figure 6. Hemoglobin-based anti-sickling agents. (A) Schematic representation of Hb tetramer showing the binding sites of aromatic aldehydes, thiols, and 2,3-DPG. The α and β subunits are

shown in cyan and gray, respectively. **(B)** Schiff-base interaction between aromatic aldehyde and N-terminal α Val1 nitrogen at the α -cleft of Hb. **(C)** A disulfide bond between thiol and β Cys93 sulfhydryl group at the β -subunit of Hb.

Aromatic aldehyde is the most studied class of the AEHs. The earliest studied aromatic aldehydes are the natural product vanillin and the synthetic benzaldehydes molecules Valesresol¹³⁵ and Tucaresol.¹³⁶ These compounds have been reported to stabilize the R-state of HbS by covalently binding to the N-terminal α Val1 nitrogen through Schiff base formation (Figure 6).^{21,137,138} The less than desirable pharmacokinetics and/or pharmacodynamics properties of Vanillin and Valeresol led to the termination of their preclinical and clinical phase 1 studies, respectively. On the other hand, Tucaresol exhibited an improved pharmacodynamics properties, yet a phase II clinic trial was terminated due to immune system-related side effects.^{136,139} The results of Vanillin, Valeresol, and Tucaresol encouraged the subsequent structural based drug discovery studies that led to the discovery of 5-hydroxymethyl-2-furfural (5-HMF) as a potential anti-sickling agent.^{137,140} 5-HMF showed significant anti-sickling properties *in vitro* and *in vivo*, yet the phase II clinical study was terminated due in part to limited bioavailability as a result of metabolic oxidation of the aldehyde moiety.¹⁴¹ Using the vanillin pharmacophore, several pyridyl derivatives of e.g. INN-312, INN-298, etc.,^{138,142} were synthesized and studied. These compounds were shown to exhibit dual anti-sickling properties by possessing a stereospecific inhibition of the polymer interaction via binding to the Hb α F-helix surface, in addition to their primary hypoxia-induced anti-sickling effect. The α F-helix is known to stabilize the polymer through secondary interactions between adjacent deoxygenated HbS molecules.¹³⁸ Furthermore, several novel anti-sickling agents such as TD, VZHE, and PP derivatives have been synthesized and shown to have superior anti-polymerization properties than the previous aromatic aldehydes.^{143–146}

Structural modification of INN-312 by a Global Blood Therapeutics scientist resulted in the discovery of the FDA approved medication, Voxelotor, that showed superior anti-sickling properties compared to all other aromatic aldehydes. Unlike the previous aromatic aldehydes that bind to Hb in a 2:1 ratio, Voxelotor binds to HbS tetramer in 1:1 stoichiometry reducing the dosing requirement to achieve the therapeutic effect. Nevertheless, unlike VZHE and PP compounds that are able to prevent sickling under complete anoxia (O_2 -independent anti-sickling effect), in addition to their primary O_2 -dependent anti-sickling activities, Voxelotor only shows an O_2 -dependent anti-sickling effect. Thus, while VZHE-039 and the PP compounds will be able to achieve disease-modifying benefits at low O_2 environments or areas of local hypoxia that are commonly seen in microvascular occlusion in SCD, Voxelotor cannot, making these compounds superior.

Triazole Sulfide is the second class of the promising AEH, forming a disulfide bond to β Cys93 on the surface of Hb (Figure 6).¹⁴⁷ This interaction leads to destabilization of the T state Hb by preventing the formation of the T-state salt bridge interaction between β Asp94 and β His146, thereby left-shifting the HbS allosteric equilibrium to the non-polymerizing high O_2 -affinity HbS.^{148,149} TD-1, is the example of this class, and was demonstrated to increase HbS oxygenation and reduce RBC sickling.¹⁴⁷

1.6.5. Reduction of 2,3-BPG concentration

2,3-BPG is a glycolytic intermediate found in high concentration in the erythrocytes. The main function of 2,3-BPG is to lower the O_2 affinity of Hb by binding with high affinity to deoxygenated Hb, allowing O_2 release to tissues. In SCD, the concentration of 2,3-BPG is abnormally elevated as a response to hypoxia. The high 2,3-BPG concentration contributes to the

SCD pathology by exacerbating HbS polymerization and RBCs sickling.^{22,150} For this reason, reducing the concentration of 2,3-BPG has been proposed as a strategy to treat SCD.

There are two proposed approaches to decrease 2,3-BPG levels in erythrocytes. One is by targeting BPGM enzyme, which is the enzyme responsible for the synthesis and hydrolysis of 2,3-BPG in erythrocyte. The second approach is by targeting the erythrocyte pyruvate kinase-R (PKR), which is the rate-limiting enzyme in glycolysis that catalyzes the interconversion of phosphoenolpyruvate to pyruvate and ATP in the last step of the glycolytic pathway (Figure 1).

Recent efforts by FORMA therapeutics have identified a novel allosteric activator for PKR named (FT-4202). The activation of PKR activity resulted in lowering the upstream 2,3-BPG level, increasing Hb's O₂ binding capacity in sickled RBCs, and decreasing vaso-occlusive crises.¹⁵⁴ Currently, FT-4202 is undergoing phase 1 clinical trials to evaluate the safety, pharmacokinetics, and pharmacodynamics profile in SCD patients (NCT03815695).¹⁵¹

Direct targeting of BPGM with compounds is yet to be fully investigated. An earlier study showed that activation of BPGM phosphatase activity by divalent anion metabisulfite and the physiological activator, 2-phosphoglycolate (2-PG), lead to a decrease in the 2,3-BPG level.¹⁵²⁻¹⁵⁴ Additionally, another study showed that *in vitro* manipulation of the phosphatase activity by incubating RBCs with exogenous glycolate resulted in decrease of the 2,3-BPG level that consequently improved the solubility and sickling tendency of sickled RBCs.^{150,155} This study also concluded that decreasing 2,3-BPG level by modulating BPGM activity inhibits HbS polymerization through three different mechanisms: (1) direct inhibition by elevation of the equilibrium solubility; (2) indirect inhibition by increasing O₂ affinity and stabilizing the oxygenated R-state Hb conformation; (3) decrease intracellular Hb concentration.^{150,155} Also, a recent study has evaluated the effect of 2,3-BPG elimination on SCD pathology by a complete

knockout of the BPGM gene in Townes model mice. The results showed that complete knockout of BPGM showed increased Hb O₂ affinity and improve RBCs sickling.¹⁵⁶

From the foregoing, it is clear that 2,3-BPG concentration in RBCs can be directly modulated through targeting the BPGM phosphatase/synthase activities. Thus, reducing the 2,3-BPG level is a potential approach to inhibit HbS polymerization and reduce RBCs sickling (Figure 7). This approach will be further investigated in this project.

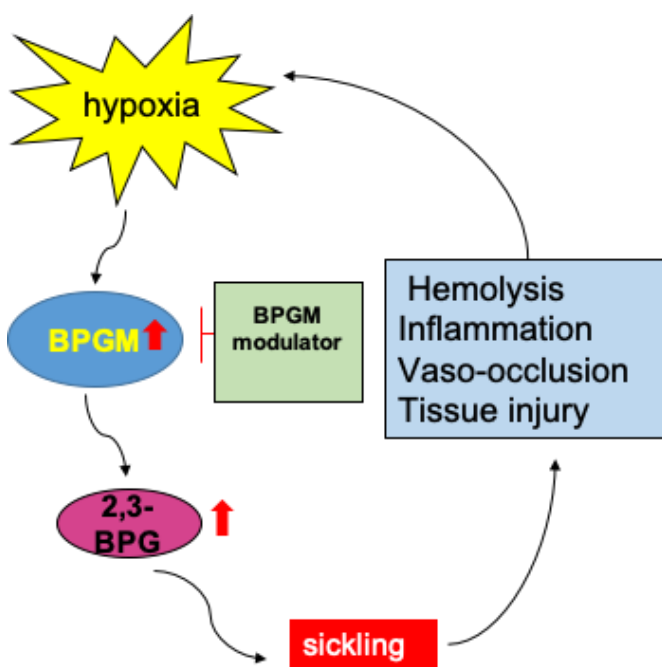


Figure 7. Effect of BPGM modulation in sickle cell disease.

1.7. Bisphosphoglycerate mutase: target for sickle cell disease drug discovery

Bisphosphoglycerate mutase (BPGM) is a member of the phosphoglycerate mutase (PGAM) enzymes family, which is a group of glycolytic enzymes essential for cell glycolysis and

regulation of 2,3-BPG. In mammals, there are two types of phosphoglycerate mutases: 2,3-BPG-dependent PGAM, also known as phosphoglycerate mutase 1 (PGAM1), and BPGM. These enzymes are closely related to each other, share a 50% sequence identity, and catalyze the same three intermolecular phosphoryl transfer reactions (synthase, phosphatase, and mutase) with a relatively different catalytic rates and substrate specificities.¹⁵⁷ Unlike PGAM1, which is expressed in nearly all tissues, BPGM is specifically expressed in erythrocytes and placenta¹⁵⁸ making it crucial for the regulation of 2,3-BPG in erythrocytes.^{5,159}

1.7.1. Structure of Bisphosphoglycerate mutase

BPGM is a homodimer with a molecular weight of 60 kDa.¹⁶⁰ Each monomer of BPGM has two domains, which consist of 10 α helices (named α 1- α 10) and 6 β sheets (named β A- β F). The BPGM catalytic core is made up of five parallel (β A, β B, β C, β D, and β F) and one anti-parallel (β E) β sheets flanked by six α helices.¹⁶⁰ The active site of BPGM on each monomer is a hollow shape and defined by His11, His188, Arg10, and Arg62 that reside at the bottom of the pocket. The mouth of the active cleft is composed of Lys18, Asn20, Arg100, Arg116, and Arg117 on one side and Ile208, Asn209, and Thr211 on the other side. The active site has a positive electrostatic potential due to the presence of several basic residues, such as Arg10, Arg62, Arg90, Arg100, Arg116, and Arg117, to accommodate the negatively charged substrates (1,3-BPG, 2,3-BPG, and 3-PGA).^{160,161} The C-terminus of BPGM lies on the rim of the entrance of the active site pocket with the side-chain of Gln251 incorporated inside the active site pocket, accommodating the binding of substrate, as well as facilitating the phosphorylation process and stabilizing the phosphoenzyme form. Therefore, the C-terminus plays an important role in the functional properties of the enzyme.¹⁶⁰ Deletion of the last 7 residues of the C-terminal tail residues has been shown to abolish the three catalytic activities of the protein.¹⁵⁹

The two monomers of BPGM are related by two-fold non-crystallographic symmetry. The dimer interface is formed by the interaction between the surface of β C-sheet and an α 2-helix of each monomer.¹⁶⁰ The dimer interface is stabilized with hydrogen-bond interactions between residues that are conserved in BPGM enzymes, including Glu51, Phe52, Asp53, His65, Glu77, and Arg140. The side-chains of Ile64, Trp68, Leu69, Leu71, and Val81 from each monomer form the hydrophobic dimerization core of the enzyme.¹⁶⁰

1.7.2. Function of Bisphosphoglycerate mutase

The BPGM enzyme was first studied by Rapoport and Luebering from rabbit erythrocyte.^{5,6} At first, it was believed that the three catalytic reactions of BPGM were regulated by multiple different enzymes due to the irreversible nature of the synthase and the phosphatase reactions.^{162,163} Later, it was concluded that the three catalytic activities are catalyzed by a single multifunctional enzyme and at the same active site.^{9,164,165} The regulatory mechanism of BPGM and its catalytic properties have been extensively studied from human RBCs by the Rosa, Rose, and Sasaki research groups.^{9,154,166-169} Rosa et al. further studied the properties and the kinetics of BPGM by developing a recombinant human BPGM expressed in *Escherichia coli* (*E.coli*).^{159,170-172}

BPGM regulates the intraerythrocytic level of 2,3-BPG by catalyzing the two irreversible reactions that are responsible for the synthesis (synthase) and degradation (phosphatase) of 2,3-BPG. 2,3-BPG synthase activity (Figure 8: Reaction 1) is the main reaction of the enzyme, and it is inhibited by its own product, 2,3-BPG, with a K_i of 0.85 μ M. However, the consequent binding of 2,3-BPG to deoxygenated Hb protects the BPGM from the product feedback inhibition.^{162,173} The phosphatase activity (Figure 8: Reaction 2), which is responsible for the hydrolysis of 2,3-BPG to the glycolytic intermediate 3-PGA, is lower than the synthase activity and is stimulated by several effectors, including chloride, sulfite, inorganic phosphate, and most potently, 2-PG, a

physiological activator that exists in RBCs with 2-5 μM concentration.¹⁵⁴ Also, the BPGM enzyme has been shown to exhibit, to a lesser extent, a mutase activity (Figure 8: Reaction 3), which is responsible for the interconversion of 3-PGA to 2-PGA.^{154,159} However, the mutase activity of the enzyme has been reported to be physiologically insignificant.¹⁶²



Figure 8. The Three enzymatic reactions of BPGM; synthase activity (Reaction 1), phosphatase activity (Reaction 2), mutase activity (Reaction 3).

1.7.3. Proposed mechanisms of action

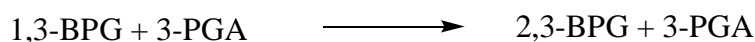
The mechanism of action of the three catalytic activities of BPGM was reported to operate via a double displacement (ping pong) mechanism that involves the formation of His-phosphorylated enzyme as an intermediate in the catalytic reaction.^{7,159,172,174} In such a mechanism, the first step requires the binding of the substrate 1,3-BPG or 2,3-BPG to the free enzyme. The second step involves the phosphorylation process of the active site residue His11, converting the enzyme into an active phosphoenzyme intermediate and 3-PGA as a first product. The last step is the transfer of phosphate group from the His11 residue to the 3-PGA, synthesizing 2,3-BPG in the

case of the synthase reaction or transfer of phosphate group from the His11 residue to a water molecule, hydrolyzing the phosphoenzyme in the case of the phosphatase reaction.¹⁷²

The three catalytic reactions of BPGM have been reported to occur at the same active site with two distinct binding sites for the substrates, one for bisphosphoglycerate (1,3-BPG and 2,3-BPG) and another for monophosphoglycerate (3-PGA and 2-PG).¹⁷⁴ However, based on the crystal structure of BPGM in complex with 2,3-BPG (PDB ID 2H4Z), as well as BPGM in complex with 3-PGA (PDB ID 2H4X), the two substrates have appeared to have similar binding mode and interactions at the active site.¹⁶¹

1.7.3.1. BPGM synthase reaction

The synthase reaction is the primary activity of BPGM. The stoichiometry of the synthase activity of BPGM has been reported as follows ¹⁶⁶



The synthase reaction starts with the binding of 1,3-BPG to the free BPGM in the first step. The second step is the transfer of the 1-phosphate group of 1,3-BPG to the active site residue His11 forming a phosphorylated His11 and the hydrolysis product, 3-PGA. There is a discrepancy in the literature regarding whether the 3-PGA dissociates from the active site to allow the binding of a second 3-PGA molecule to complete the synthesis reaction or if 3-PGA stays in the active site as an intermediate and undergo re-phosphorylation to be converted to 2,3-BPG.

Early reports by Rose et al. postulated that the release of 3-PGA from the active site after the dephosphorylation of 1,3-BPG, followed by the binding of another molecule of 3-PGA as a second substrate/cofactor.^{7,175} Then, the phosphoryl group transfers from His11 to 2-hydroxyl group of 3-PGA, synthesizing 2,3-BPG. In addition, Rose reported that the rate-limiting step for

the synthase reaction is the phosphorylation of His11.⁸ However, a recent study by Chu et al.¹⁷⁶ using a combination of classic molecular dynamic (MD) and quantum mechanics/molecular mechanics (QM/MM) metadynamics and the umbrella sampling method reported that the rate-limiting step of the synthase reaction is the re-phosphorylation of 3-PGA into 2,3-BPG. According to Chu, the synthase reaction includes three steps catalyzing the conversion of 1,3-BPG to 2,3-BPG with the formation of 3-PGA as an intermediate (Figure 9). The first step involves the fast phosphorylation of His11 by the acyl phosphate group of 1,3-BPG. Then, the hydroxyl group of 3-PGA rotates toward the glutamic acid residue (Glu89) to allow for proton transfer from the hydroxyl group of 3-PGA to the carboxylic group of Glu89 (Figure 9). Next, the electrostatic repulsion between the negatively charged phosphoryl oxygen atom of His11 and the negatively charged carboxyl group of 3-PGA helps to position the 2-hydroxyl group of 3-PGA for re-phosphorylation to form 2,3-BPG.¹⁷⁸

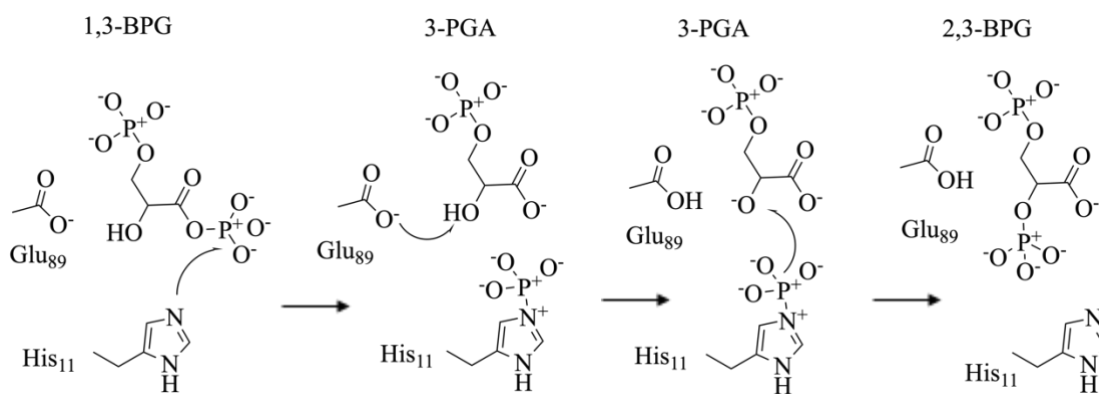


Figure 9. Mechanism of action of the BPGM synthase activity.

1.7.3.2. BPGM phosphatase reaction

The phosphatase reaction of the enzyme involves the hydrolysis of 2,3-BPG into 3-PGA and inorganic phosphate (Figure 8: Reaction 2). The hydrolysis product, 3-PGA, has been demonstrated to dissociate from the active site after the enzyme phosphorylation. Then, the activated water molecule at the active site acts as a second substrate hydrolyzing the phosphoenzyme.¹⁵⁴ The high-resolution crystal structures of BPGM in complex with 2,3-BPG shed light on the actual catalytic mechanism of the phosphatase activity.¹⁶¹ The co-crystal structures revealed snapshots of the histidine phosphorylation process that follows SN2 reaction, which entails the imidazolium ring of His11 acting as a nucleophile to attack and remove the 2-phosphate group of 2,3-BPG to form a phosphoenzyme intermediate.¹⁶¹ The MD/QM/MM study of the phosphatase reaction performed by Chu et al. provides support to the described crystallographic study of BPGM in complex with 2,3-BPG (Figure 10).¹⁷⁶ According to Chu, His11 first attacks the 2-phosphate group of 2,3-BPG. As a result, the oxygen atom of 3-PGA will carry a negative charge that attracts the proton transfer from Glu89 to 3-PGA to be liberated.^{14,27} Following, the negatively charged Glu89 activates a water molecule in the catalytic site to accept the phosphate group from the phosphorylated His11, thereby hydrolyzing the phosphoenzyme. In the case of stimulated phosphatase activity by the activator 2-PG, the exact mechanism of activation is not conclusive, but it has been proposed that 2-PG binds to the active site as a second substrate, facilitating the dephosphorylation of phosphoenzyme to the water molecule.^{154,166}

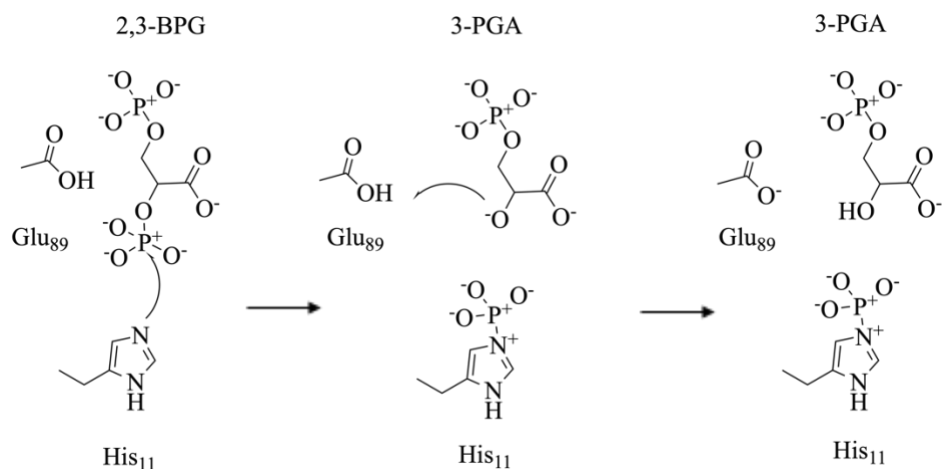


Figure 10. Mechanism of action of BPGM phosphatase activity.

1.7.3.3. BPGM mutase reaction

The mutase reaction is responsible for the interconversion of 3-PGA to 2-PGA in the main glycolysis pathway (Figure 8: Reaction 3). The steady-state kinetics of the mutase reaction of BPGM have not been studied in detail, like the synthase and phosphatase reactions. It is assumed that the mutase reaction operates by the same mechanism as that of the homologous PGAM1, which is the enzyme that mainly catalyzes this reaction.¹⁶²

CHAPTER 2

2. RATIONALE, GOAL, HYPOTHESIS, AND SPECIFIC AIMS

2.1. Rationale

Sickle Cell Disease (SCD) has been known for over 100 years, yet the development of safe and effective treatment of the disease still poses significant challenges. For example, although Hydroxyurea (HU) is the most proven therapeutic approach for SCD as evidenced by the sustained clinical use for over two decades, a reported lack of response to HU in up to 30% of patients and poor compliance, tends to limit its use.⁴⁸ Though L-glutamine (Endari) is approved by the FDA to treat SCD in the US, the European Union has recommended against approval due to limited evidence of efficacy in phase III trials.^{65,66} The recently FDA approved medication for SCD, Voxelotor, is based on increased hemoglobin (Hb) levels and reduced hemolysis in patients without improving pain or vaso-occlusion.¹⁷⁷ These surrogate end-points are thus not long-term clinical outcomes. Therefore, the limited availability of SCD treatment calls for an urgent need for new targeted therapies.

SCD has complex pathophysiology with a single root cause, the polymerization of deoxygenated sickle Hb (HbS), which is exacerbated by 2,3-bisphosphoglycerate (2,3-BPG) elevation in red blood cells (RBCs) as a result of glycolysis activation in response to hypoxia.^{22,150,178} Therefore, a logical approach to treat SCD is to target bisphosphoglycerate (BPGM) enzyme, an enzyme responsible for the regulation of the 2,3-BPG concentration in the erythrocyte.

BPGM is a multifunctional enzyme in the Rapoport-Leubering pathway that regulates the intraerythrocytic level of 2,3-BPG by catalyzing two irreversible reactions responsible for the synthesis (synthase) and degradation (phosphatase) of 2,3-BPG that occur at the same active site.⁹

The pharmacological inhibition of the 2,3-BPG synthase activity, or activation of 2,3-BPG phosphatase activity, or both, may be an intriguing approach to decrease 2,3-BPG level in erythrocyte. However, despite the long-standing knowledge about the involvement of 2,3-BPG in SCD pathophysiology, this approach has not been well studied for the treatment of SCD due, in part, to a lack of understanding of the BPGM catalytic mechanisms. Therefore, one objective of this study is to understand the kinetics of BPGM synthase and phosphatase activities.

The synthase activity of BPGM is the main activity of the enzyme. The phosphatase activity of BPGM is low (approximately 1,000-fold lower than the synthase activity), but it is physiologically activated by the endogenous substance, 2-phosphoglycolate (2-PG).¹⁵⁰ The mechanism involved in the phosphatase activation by 2-PG is a long-standing puzzle that is yet to be explored. Thus, the second objective of this study is to understand the mechanism of phosphatase activation, as well as the atomic interaction of BPGM with 2-PG, which is expected to provide valuable insight and foundation for design of small molecule phosphatase activators or synthase inhibitors with potential therapeutic benefit.

Activation of BPGM phosphatase activity has been studied by incubating sickle RBCs with exogenous glycolate, which resulted in a reduction of 2,3-BPG levels and inhibition of RBC sickling.¹⁵⁰ These observations suggest that the synthase/phosphatase activity of BPGM could be potential targets for achieving anti-sickling effect. Therefore, the third objective of this project is to identify and screen for active site modulators of BPGM for potential treatment of SCD.

Reported biochemical assays for the synthase and phosphatase activities, such as radioactive and spectrophotometric coupled activity assays possess challenges, especially for high-throughput screening purposes.^{154,166,170,171,175,179} As such, the fourth objective of this project is to develop a direct, fast, and convenient assay suitable for compounds screening.

In conclusion, the ultimate research goal is to identify BPGM modulators that reduce the concentration of 2,3-BPG in RBCs to prevent pathological hypoxia-induced HbS polymerization and RBC sickling for the treatment of sickle cell disease.

2.2. Hypothesis

Inhibitors of synthase and/or activators of phosphatase activities of BPGM may decrease the level of 2,3-BPG and prevent hypoxia-induced HbS polymerization and RBCs sickling.

2.3. Specific Aims

Specific Aim 1: Elucidate the kinetics of the synthase and phosphatase activities of BPGM and optimize the activity assays for compounds screening.

Specific Aim 1A: Kinetic characterization of BPGM synthase activity and optimization of the BPGM.GAPDH synthase coupled assay.

Specific Aim 1B: Kinetic characterization of BPGM phosphatase activity and optimization of the malachite green assay and GAPDH.PGK.BPGM coupled assay.

Specific Aim 1C: Understanding 2-PG activation mechanism of BPGM phosphatase activity using GAPDH.PGK.BPGM coupled assay.

Specific Aim 2: Elucidate the atomic interaction of BPGM phosphatase with its effectors, and identify allosteric binding site(s) of BPGM.

Specific Aim 2A: X-ray crystallography studies of BPGM in complex with 2-PG or citrate.

Specific Aim 2B: The use of the computational solvent mapping tool (FTMap) to identify allosteric binding sites of BPGM.

Specific Aim 3: Identification of BPGM synthase inhibitor and/or phosphatase activators that can be used as leads for SCD drug discovery.

Specific Aim 3A: Identification of BPGM modulators targeting BPGM active site.

Specific Aim 3B: Identification of BPGM modulators targeting BPGM dimer interface.

Specific Aim 3C: Investigation of modulators effect on BPGM phosphatase and synthase activity.

Specific Aim 3D: Elucidate the X-ray crystallographic binding between BPGM and PGMI-004A.

CHAPTER 3

3. SPECIFIC AIM 1: Elucidate the kinetics of the synthase and phosphatase activities of BPGM and optimize the activity assays for compounds screening

Bisphosphoglycerate mutase (BPGM) enzyme plays a major role in regulating hemoglobin (Hb) oxygen affinity by controlling the concentration of 2,3-bisphosphoglycerate (2,3-BPG) level in human red blood cells (RBCs) through its synthase and phosphatase activities in a pathway called the Rapoport-Leubering pathway.^{6,7,13} As previously noted, 2,3-BPG is the major allosteric modulator for Hb, binding preferentially to deoxygenated Hb to shift the protein's allosteric equilibrium from high-oxygen-affinity relaxed (R) state to the low-oxygen-affinity Tense (T) state, facilitating tissues oxygenation.^{12,18}

BPGM is the central enzyme of the Rapoport-Leubering pathway, mainly catalyzing the irreversible synthesis of 2,3-BPG from the glycolytic intermediate 1,3-bisphosphoglycerate (1,3-BPG) (Figure 8; Reaction 1), referred to as synthase activity. Interestingly, BPGM also regulates the concentration of 2,3-BPG in the cell through a phosphatase activity by catalyzing the hydrolysis of 2,3-BPG to the glycolytic metabolite, 3-phosphoglycerate (3-PGA), and inorganic phosphate (P_i) (Figure 8; Reaction 2).^{7,8,154,170,179} This phosphatase activity is activated by a physiological activator, 2-phosphoglycolate (2-PG).¹⁵⁴ In addition, BPGM has a minor mutase activity that catalyzes the reversible interconversion of 3-PGA to 2-phosphoglycerate (2-PGA) (Figure 8; Reaction 3) in the main glycolytic pathway, a reaction mainly catalyzed by the homologous enzyme phosphoglycerate mutase 1 (PGAM1).⁹ One objective is to gain further insight into the mechanisms of both the phosphatase and synthase activities that are not yet fully

understood. Another objective of this study is to elucidate 2-PG activation mechanism and binding mode to BPGM.

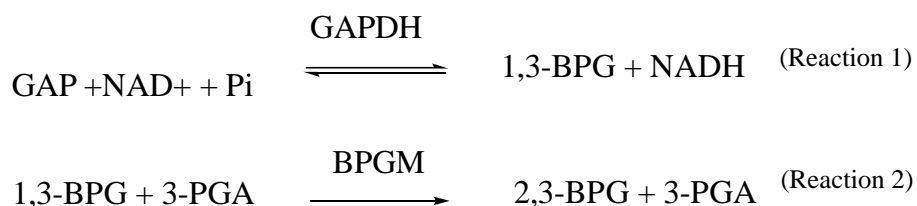
Due to BPGM is central and important role in physiological regulation of 2,3-BPG, it is recognized that modulation of BPGM activity to decrease 2,3-BPG concentration would have an important clinical implication for sickle cell disease (SCD).^{150,180,181} People with SCD have unusually high levels of 2,3-BPG, which is implicated in the disease pathophysiology by promoting hypoxia-induced HbS polymerization and RBC sickling.^{22,150} Another objective of this project is to identify lead compounds to inhibit the synthase activity and/or activate the phosphatase activity of BPGM to reduce 2,3-BPG concentration, which potentially could be developed for SCD therapy. Achieving this goal requires availability of direct and simple assays for drug screening.

The BPGM synthase and phosphatase activities have been studied using two main methods: a continuous coupled enzymatic activity assay and a radiolabeled activity assay.^{152,154,166,167,170,179} In order to find a suitable assay for screening of potential BPGM modulators, the activity and kinetic characterizations of the synthase and the phosphatase activities of BPGM were studied using previously reported coupled assays.^{152,154,166,167,170,179} Furthermore, in an alternative to the radiolabeled activity assay, a direct non-radioactive colorimetric assay, malachite green assay, was also utilized for measuring BPGM phosphatase activity.

3.1. Specific Aim 1A: Kinetic characterization of BPGM synthase activity and optimization of the BPGM.GAPDH synthase coupled assay.

The synthase activity of BPGM was tested in a continuous, spectrophotometric, enzyme-coupled assay in which the production of 2,3-BPG is coupled with the activity of glyceraldehyde-

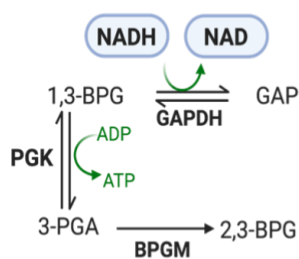
3-phosphate dehydrogenase (GAPDH), catalyzing the reduction of nicotinamide adenine dinucleotide (NAD) to the reduced form (NADH), that can be detected spectrophotometrically at A_{340} nm. The overall reactions of the assay are as follow:



Since the substrate of BPGM synthase, 1,3-BPG, is commercially unavailable due to its instability and propensity to rapidly isomerize to 2,3-BPG, the first step of this assay is to enzymatically synthesize 1,3-BPG. 1,3-BPG was synthesized from glyceraldehyde-3-phosphate (GAP) by GAPDH (Reaction 1). GAPDH catalyzes the synthesis of 1,3-BPG by reducing NAD to NADH and this conversion is monitored spectrophotometrically by the increase in the absorbance signal at A_{340} nm. The reaction course is followed until it reaches a plateau, which indicates a steady-state formation of 1,3-BPG. Following, an aliquot of BPGM is added to the reaction mixture and further increase of the absorbance signal is observed (Reaction 2). The formation of NADH following the addition of BPGM corresponds to 2,3-BPG production and BPGM synthase activity. In this assay, the auxiliary enzyme GAPDH (2 U/mL), GAPDH substrates, GAP (3 mM), and NAD (1 mM) were in high concentrations to ensure that the saturation condition of the assay mixture is achieved for the BPGM to be the only limiting factor for the assay. The reported K_m values of GAP and NAD for GAPDH are 77 μM and 57 μM , respectively; thus, the concentrations of the substrates used in the assay were in high excess.¹⁸²

In the first step of the assay reaction (Reaction 1), only 0.1% of the initial concentration of GAP (3 mM) was utilized to synthesize 1,3-BPG. Then, the addition of BPGM to the assay mixture consumed the initially formed 1,3-BPG to synthesize 2,3-BPG (Figure 11). Thereafter, the consumption of 1,3-BPG forces the remaining GAP and GAPDH in the reaction mixture to proceed in the forward direction reaction producing more 1,3-BPG that is directly related to 2,3-BPG synthesis (Figure 11).

A



B

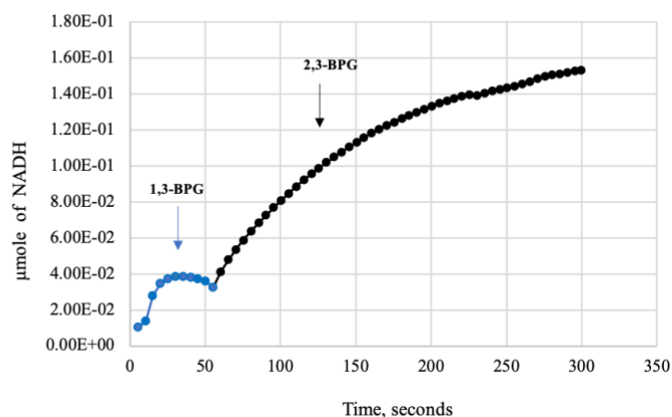


Figure 11. (A) BPGM synthase coupled assay reactions. **(B)** BPGM synthase progress curve; blue line corresponds to 1,3-BPG production and black line corresponds to 2,3-BPG production.

The assay was performed in a 1 mL final assay volume in a quartz cuvette using Agilent 8453 UV-VIS spectrophotometer. A time-dependent reaction was assessed to select the linear region of the enzymatic reaction to study the enzymatic activity. From the reaction progress curve, the assay duration was set to 300 s (Figure 11).

BPGM activity was measured by varying the concentration of BPGM (0.1 -2.5 μM) and the result showed a linear dependence of the activity to the enzyme concentrations (Figure 12). BPGM activity was measured by calculating the slope of the tangent line in the reaction progress curve (Figure 11 B). A concentration of 0.3 μM was selected as a standard concentration to be used in studying the enzyme activity and subsequent compounds screening assay. The assay was validated by determining the effect of 2-PG on the synthase activity. 2-PG has been reported as an inactivator of the synthase activity.¹⁶⁶

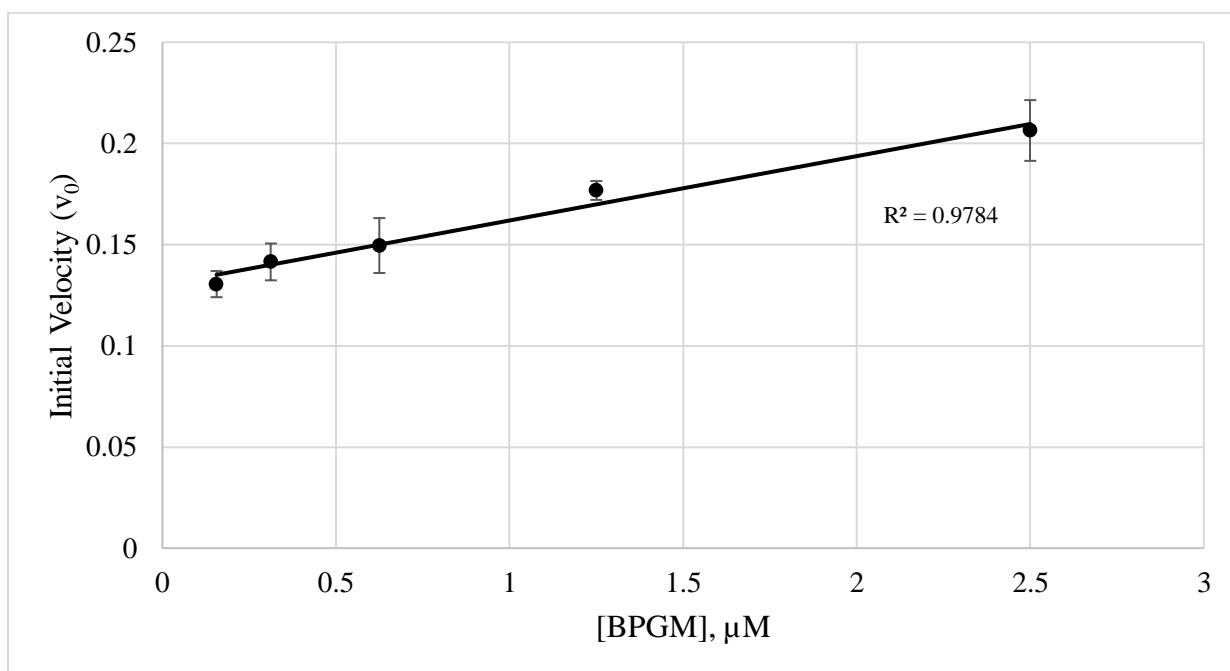


Figure 12. Dependence of the synthase reaction velocity on the enzyme concentrations.

The activity of the enzyme was determined to be 0.07 μmole of NADH/min and in the presence of 1 mM of 2-PG, the activity was reduced by half to 0.03 μmole of NADH/min (Table 1).

Table 1. BPGM synthase activity and specific activity in presence and absence of 2-PG.

	Enzyme activity	Specific activity
	μmole of NADH/min	μmole of NADH/min/mg
Control	0.07 ± 0.01	8 ± 0.5
With 1mM 2-PG	0.03 ± 0.02	3.3 ± 0.8

The Michaelis-Menten constant of 1,3-BPG for BPGM could not be obtained due to the high instability of 1,3-BPG.¹⁷² Since 1,3-BPG has to be enzymatically synthesized at the time of the assay, and it was difficult to vary the concentration of 1,3-BPG to measure the K_m value. Regardless of this limitation, the synthase coupled activity assay will be used for screening BPGM modulators. However, due to its cumbersome nature, it cannot be used for high-throughput screening, but rather as a hit confirmatory assay.

3.2. Specific Aim 1B: Kinetic characterization of BPGM phosphatase activity and optimization of the malachite green assay and GAPDH.PGK.BPGM coupled assay

3.2.1. Kinetic characterization of BPGM phosphatase activity and optimization of the malachite green assay

BPGM phosphatase activity was studied using a commercially available malachite green assay kit, a colorimetric assay that quantifies liberated inorganic phosphate (P_i) upon 2,3-BPG hydrolysis to 3-PGA. The P_i released from the reaction forms a green complex with the ammonium molybdate in the malachite green reagent and then is detected spectrophotometrically at an

absorbance of A_{620} nm. The concentration of phosphate is then calculated using a P_i calibration curve (Figure 13).

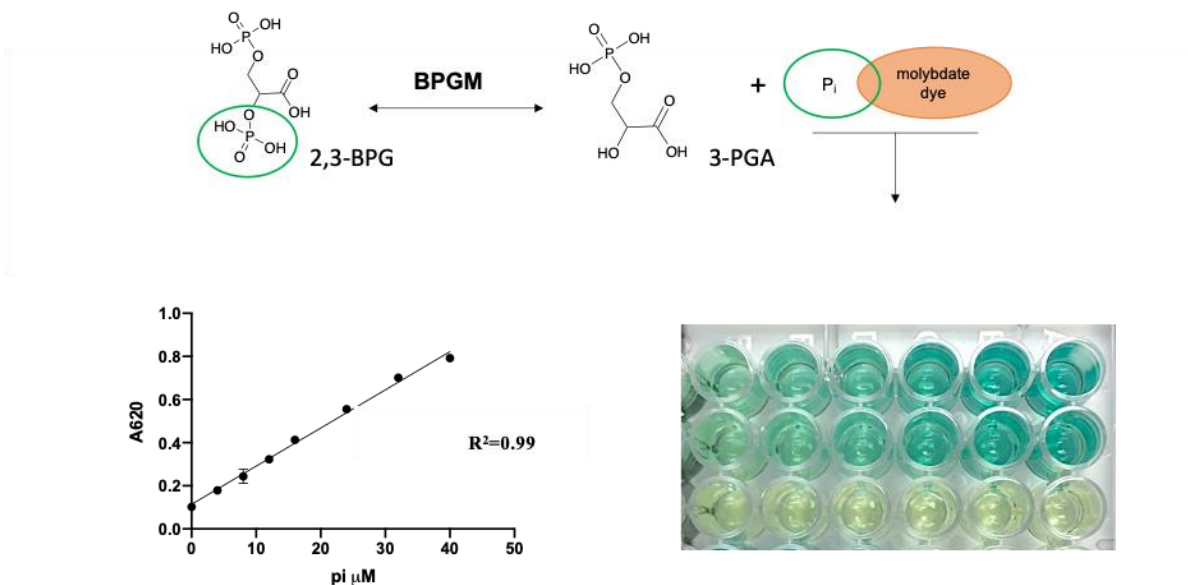


Figure 13. The principle of the malachite green assay.

The phosphatase activity of BPGM is inherently low, and as a result, the potent phosphatase activator, 2-PG, has frequently been used for its detection.^{8,171} Thus, BPGM phosphatase activity will be determined in the presence and absence of 2-PG.

A time-dependent assay was first performed to select the optimum assay duration. The reaction was left for 80 min, and every 10 min, an aliquot of the assay mixture was taken and the absorbance for the released P_i was measured as per assay protocol.

The non-activated phosphatase showed a slower reaction compared to the 2-PG activated reaction (Figure 14). From the time-dependent experiment, the duration of the assay was set within the linear range of the activity. Therefore, the assay time duration for the non-activated reaction was set to 50 min, while the 2-PG activated assay time duration was set to 20 min (Figure 14).

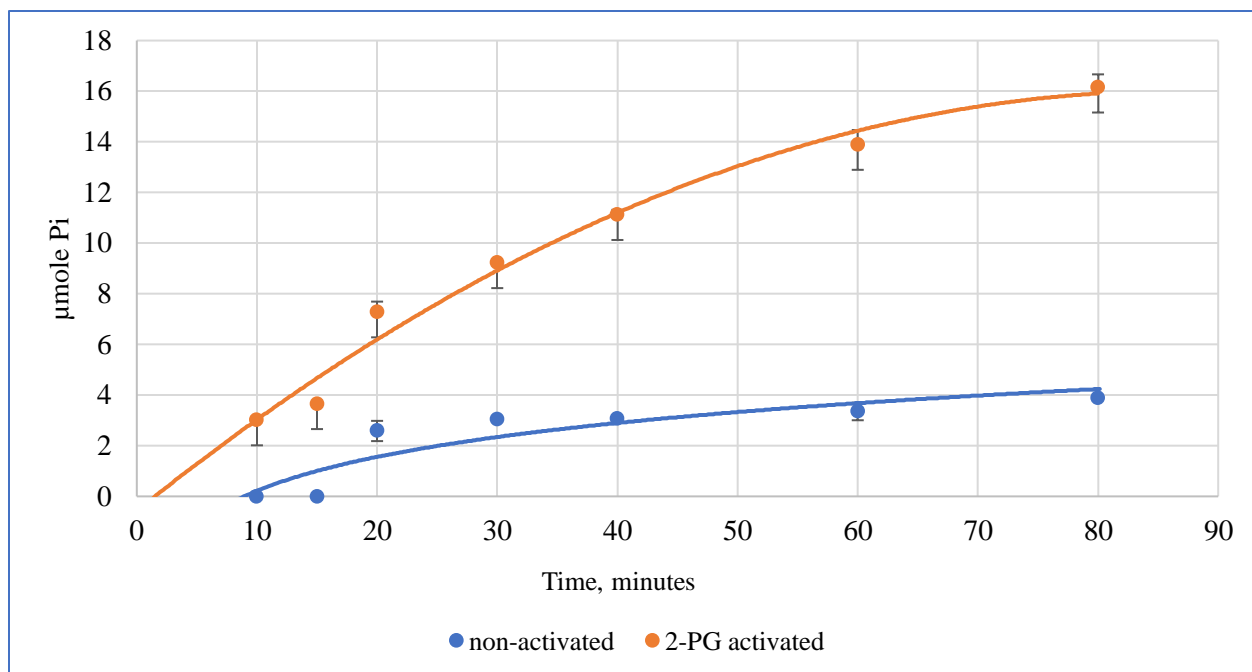


Figure 14. Time-dependent of BPGM phosphatase activity in the presence and absence of 2-PG.

BPGM phosphatase activity was measured using varying enzyme concentrations (0.6-10 μM), and the result showed a direct relationship between the velocity and the enzyme concentrations for both non-activated and activated phosphatase reactions (Figure 15, 16). Conditions that yield linear results with respect to time and enzyme concentration were used for the enzyme steady-state kinetic analysis. All subsequent phosphatase assays were performed using 5 μM as a standard BPGM concentration in the non-activated reaction and 2 μM in the 2-PG activated reaction.

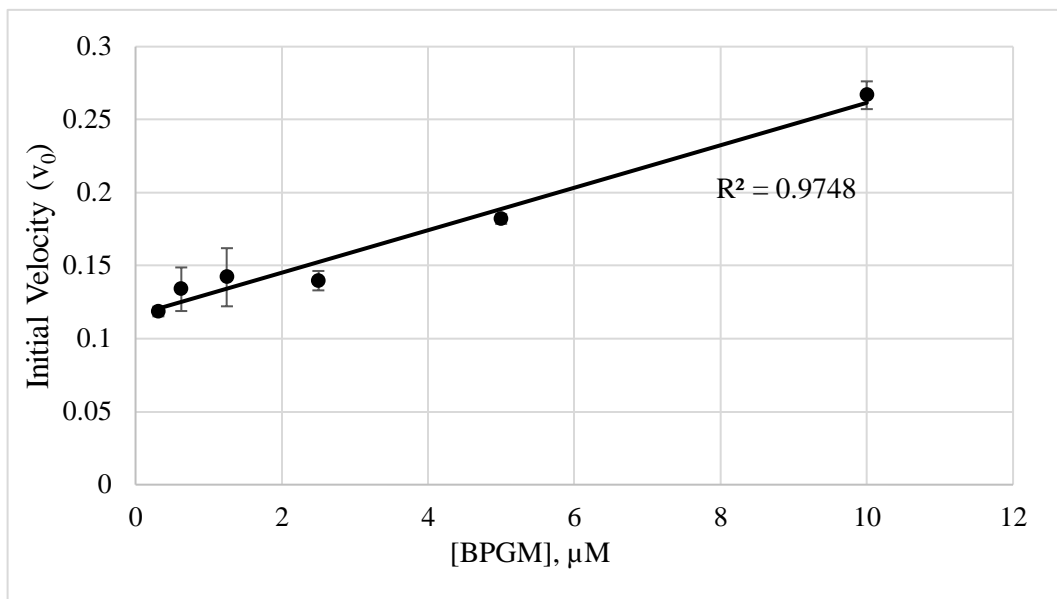


Figure 15. Linear dependence of the non-activated phosphatase reaction velocity on enzyme concentrations in the absence of 2-PG.

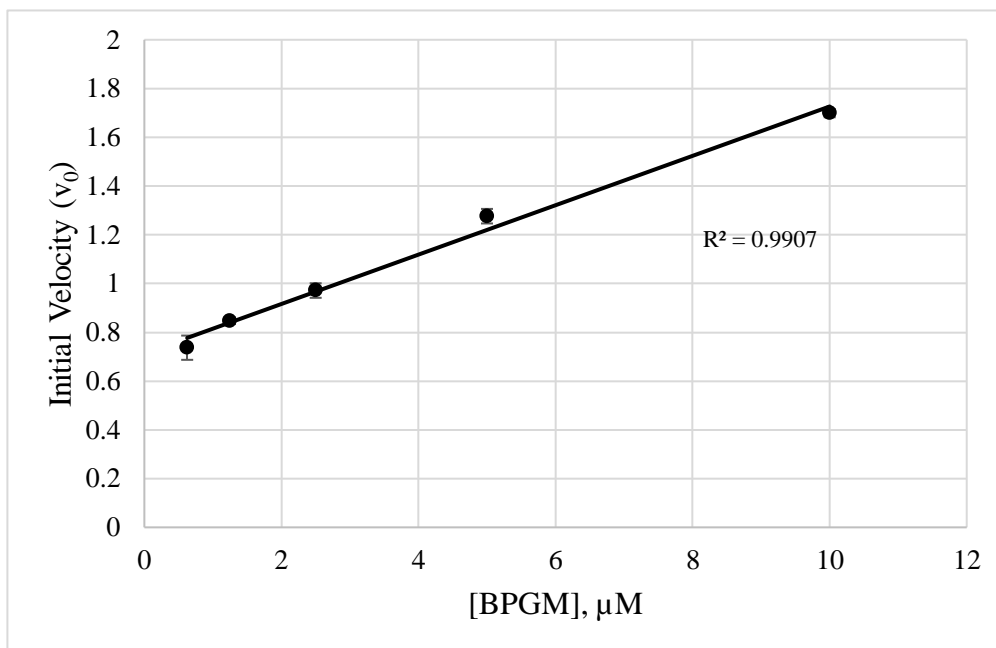


Figure 16. Linear dependence of the activated phosphatase reaction velocity on enzyme concentrations in the presence of 2-PG.

The phosphatase activity of the enzyme was measured in the presence and absence of 2-PG, and the activity was defined as $\mu\text{mole P}_i$ released per min. In the presence of 5 μM 2-PG, the phosphatase activity was enhanced to 1.3 $\mu\text{mole P}_i/\text{min}$ compared to the control (non-activated phosphatase, without 2-PG) of 0.18 $\mu\text{mole P}_i/\text{min}$ (Table 2).

The K_m value of 2,3-BPG for the enzyme in the non-activated reaction was $97 \pm 7 \mu\text{M}$ and the V_{max} was 0.2 $\mu\text{mole P}_i/\text{min}$ using 5 μM BPGM (Table 2, Figures 17). The apparent K_m and V_{max} for the activated reaction (in the presence of 5 μM 2-PG) were $39 \pm 13 \mu\text{M}$ and 0.7 $\mu\text{mole P}_i/\text{min}$ respectively using 2 μM BPGM (Table 2, Figure 18).

In summary, the malachite green assay is considered to be a direct, fast assay that can be easily adopted for high-throughput screening of BPGM phosphatase activators.

Table 2. BPGM phosphatase activity and steady-state kinetic parameters in the presence and absence of 2-PG.

	Enzyme activity $\mu\text{mole P}_i / \text{min}$	$K_m, \mu\text{M}$	$V_{\text{max}},$ $\mu\text{mole P}_i/\text{min}$	$k_{\text{cat}}, \text{min}^{-1}$
Control (without 2-PG)	0.200 ± 0.003	97 ± 7	0.20 ± 0.04	0.04 ± 0.02
With 5μM 2-PG	1.30 ± 0.03	39 ± 13	0.7 ± 0.2	0.3 ± 0.1

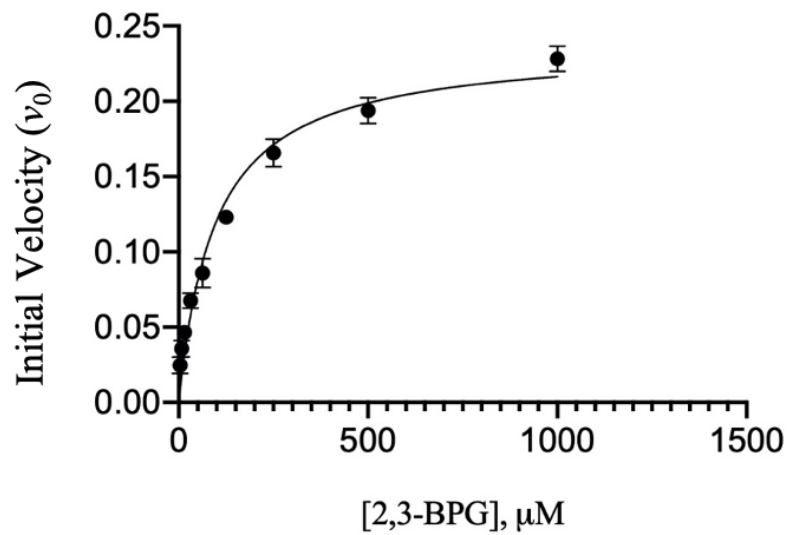


Figure 17. Michaelis-Menten plot of 2,3-BPG on the phosphatase reaction velocity in the absence of 2-PG.

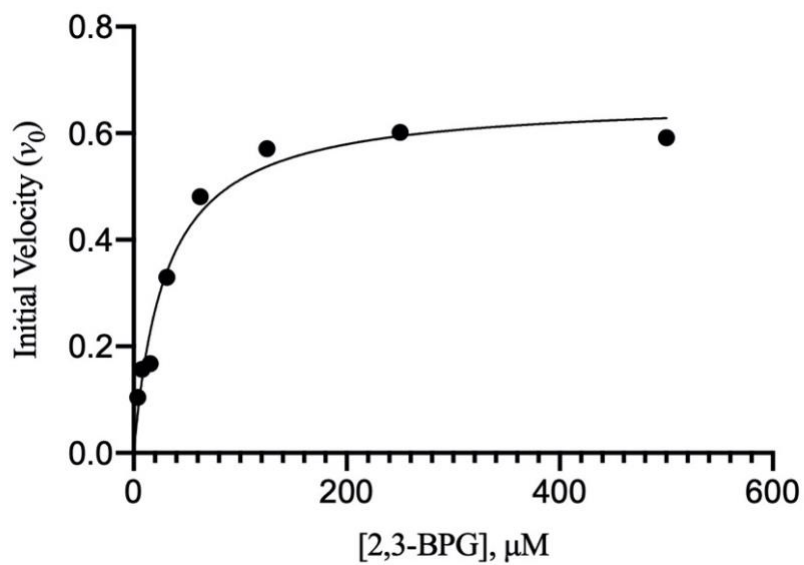
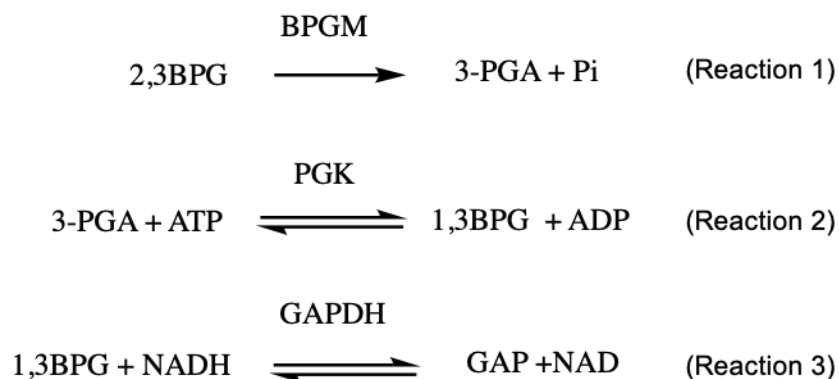


Figure 18. Michaelis-Menten plot of 2,3-BPG on the phosphatase reaction velocity in the presence of 2-PG.

3.2.2. Kinetic characterization of BPGM phosphatase activity and optimization of PGK•GAPDH•BPGM coupled phosphatase assay

A second assay used to study the BPGM phosphatase activity is the PGK•GAPDH•BPGM phosphatase coupled enzymatic assay in which the BPGM phosphatase activity is coupled with Phosphoglycerate kinase (PGK) and GAPDH enzymes activities that is detectable spectrophotometrically at absorbance of A_{340} nm. The overall reactions of the assay are as follow:



The assay reaction starts with the hydrolysis of 2,3-BPG by BPGM into 3-PGA (Reaction 1), which is the substrate for the PGK. In the presence of ATP, PGK consumes 3-PGA and ATP to catalyze the formation of 1,3-BPG and ADP (Reaction 2). The formed 1,3-BPG is then hydrolyzed by GAPDH into GAP with subsequent oxidation of NADH to NAD detected at A_{340} nm (Reaction 3). The phosphatase activity of BPGM is directly proportional to NADH oxidation, which can be observed as a reduction in NADH absorbance at 340 nm as the reaction progresses.

From the phosphatase reaction progress curve, the duration of the assay was set to 30 min in the absence of 2-PG, and 10 min in the presence of 2-PG. BPGM phosphatase activity was

studied with various concentrations of BPGM (1-10 μM) and the results showed a linear dependence of the reaction velocity with the enzyme concentrations (Figure 19).

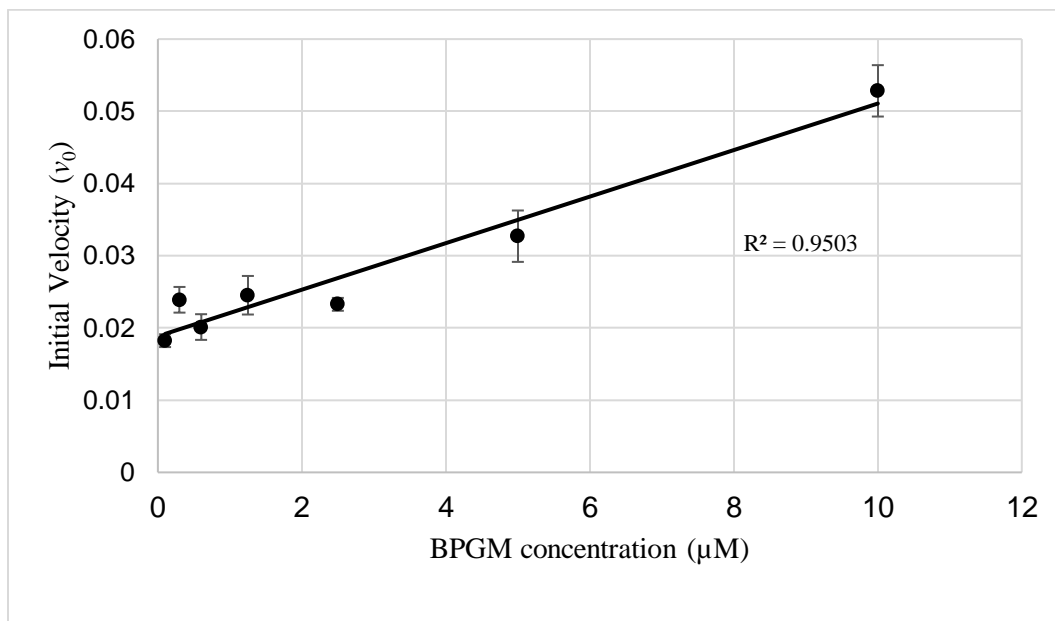


Figure 19. Linear dependence of the non-activated phosphatase reaction velocity on enzyme concentration.

The phosphatase activity at saturating concentration of 2,3-BPG (0.8 mM) in the presence and absence of 2-PG was measured, and the results are summarized in (Table 3). The results show that the phosphatase activity using 5 μM BPGM in the absence of 2-PG was 0.03 μmole of NADH/min. In the presence of 10 μM 2-PG, the phosphatase activity was stimulated to 0.3 μmole NADH/min. These values can be compared with the data obtained using the malachite green assay that showed an activity of 0.2 μmole P_i /min in the absence and 1.3 μmole P_i /min in the presence of 5 μM 2-PG (Table 2).

The K_m value of 2,3-BPG for the enzyme in the absence of 2-PG was $77.9 \pm 1.7 \mu\text{M}$ and the V_{max} was $0.2 \mu\text{mole NADH/minute}$ (Table 3). These values compare with the K_m and V_{max} of $97 \pm 7 \mu\text{M}$ and $0.2 \mu\text{mole P}_i/\text{min}$, respectively using the malachite green assay (Table 2). The apparent K_m ($K_{m \text{ app}}$) of 2,3-BPG in the presence of $10 \mu\text{M}$ 2-PG decreased to $43 \pm 3 \mu\text{M}$ and V_{max} stimulated to $0.34 \mu\text{mole NADH/min}$ (Table 3). These compare to $39 \pm 13 \mu\text{M}$ and $0.7 \mu\text{mole P}_i/\text{min}$, respectively using the malachite green assay (Table 2). The two assays resulted in similar kinetic values.

The GAPDH.PGK.BPGM coupled assay was validated by testing the stimulating effect of 2-PG on BPGM phosphatase activity. This assay will be used for drug screening as a secondary (confirmatory) assay to the malachite green assay, which will be the primary assay.

Table 3. BPGM phosphatase activity and steady-state kinetic parameters in the presence and absence of 2-PG.

	Enzyme activity $\mu\text{mole NADH/min}$	$K_m, \mu\text{M}$	$V_{\text{max}},$ $\mu\text{mole NADH/min}$	$k_{\text{cat}}, \text{min}^{-1}$
Control	0.030 ± 0.003	77.9 ± 1.7	0.2 ± 0.1	0.05 ± 0.01
With $10 \mu\text{M}$ 2-PG	0.30 ± 0.01	43 ± 3	0.34 ± 0.01	0.340 ± 0.002

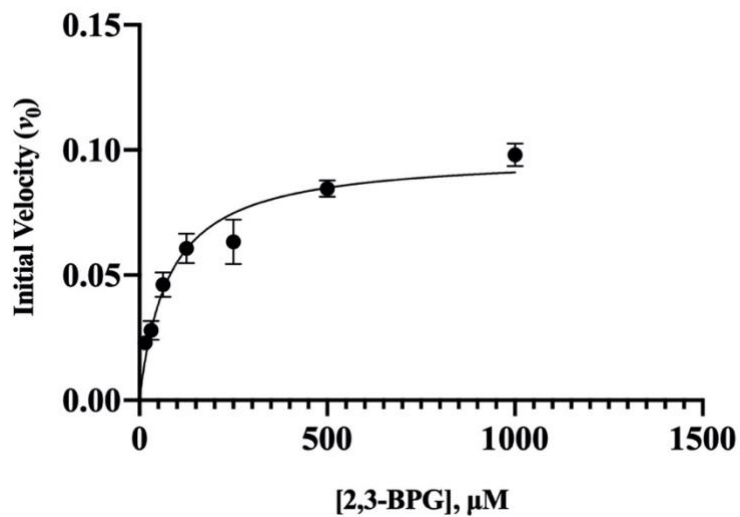


Figure 20. Michaelis-Menten plot of 2,3-BPG on the phosphatase reaction velocity in the absence of 2-PG.

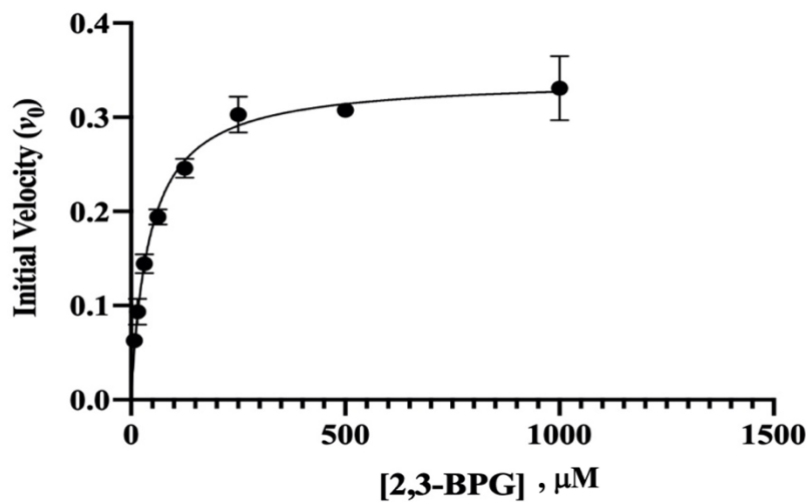


Figure 21. Michaelis-Menten plot of 2,3-BPG on the phosphatase velocity in the presence of 2-PG.

3.3. Specific Aim 1C: Understand the activation mechanism of 2-PG on BPGM phosphatase activity using the GAPDH.PGK.BPGM coupled assay

2-PG is the most potent physiological activator of BPGM phosphatase activity.¹⁵⁴ The exact activation mechanism of 2-PG is poorly understood. Achieving a full understanding of the activation mechanism would help future efforts in the design of mechanism based BPGM modulators. Therefore, the activation mechanism of 2-PG for phosphatase activity was studied using the PGK•GAPDH•BPGM coupled phosphatase assay. Data were plotted for Michaelis-Menten nonlinear regression using GraphPad prism software. The Michaelis-Menten plot showed a pattern that best fits the noncompetitive inhibition model, in which both K_m , and V_{max} values changed with increasing concentration of 2-PG from 10 – 1000 μM (Figure 22).

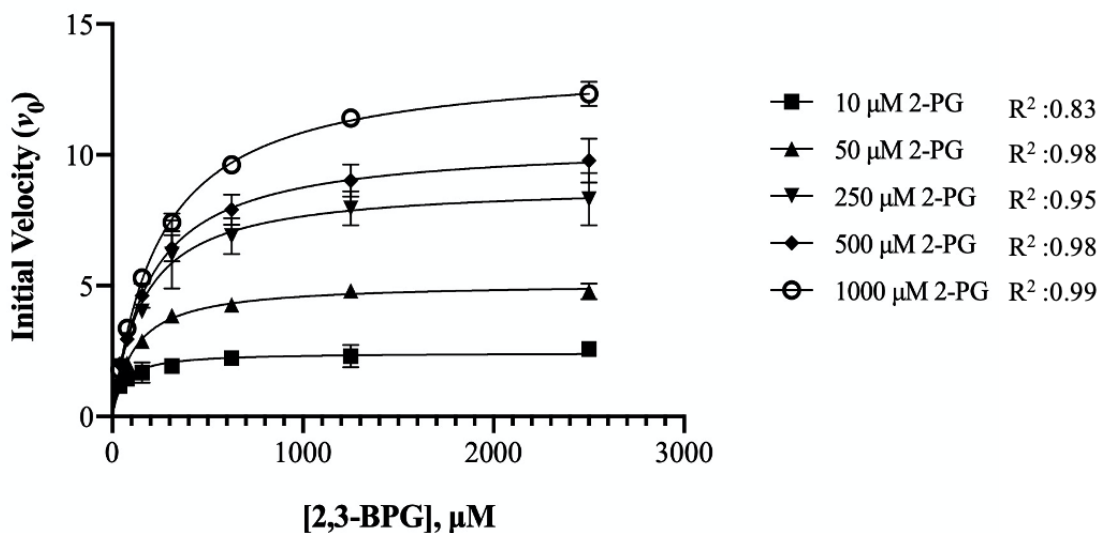


Figure 22. Michaelis-Menten nonlinear regression plot of substrate-velocity curves at five different activator concentrations.

The apparent kinetic constants were determined for each 2-PG concentration, and the results are summarized in Table 4.

Table 4. Enzyme kinetic parameter of 2,3-BPG hydrolysis by BPGM phosphatase in the presence of 2-PG.

[2-PG], μM	V_{max} , $\mu\text{mole NADH}/\text{min}$ (\pm SD)	$K_{\text{m app (2,3-BPG)}}$, μM (\pm SD)	k_{cat} , min^{-1} (\pm SD)
0	0.2 ± 0.1	77.9 ± 1.7	0.05 ± 0.01
10	0.45 ± 0.06	42 ± 18	0.18 ± 0.02
50	0.98 ± 0.03	103 ± 14	0.40 ± 0.01
250	1.66 ± 0.27	133 ± 30	0.7 ± 0.1
500	2.0 ± 0.17	225 ± 80	0.88 ± 0.07
1000	2.8 ± 0.3	267 ± 55	1.12 ± 0.11

The kinetics constants results (Table 4) showed that the affinity of 2,3-BPG to BPGM increased with the addition of 10 μM concentration of 2-PG ($K_{\text{m app}}$ 42 μM) compared to the K_{m} value of 2,3-BPG in the absence of 2-PG (K_{m} 77.9 μM). Interestingly, as the concentration of 2-PG increased beyond 10 μM , the affinity of 2,3-BPG to the enzyme starts to decrease from $K_{\text{m app}}$ of 103 μM (at 50 μM concentration of 2-PG) to $K_{\text{m app}}$ of 267 μM (at 1000 μM concentration of 2-

PG) (Figure 23). The k_{cat} and V_{max} , however, increased linearly with increasing 2-PG concentrations (Figure 23).

The decrease in the $K_{m\ app}$ of 2,3-BPG value at low 2-PG concentration may suggest noncompetitive activation by binding of 2-PG to an allosteric or non-catalytic binding site. By contrast, the increase in the $K_{m\ app}$ of 2,3-BPG observed at high 2-PG concentrations may indicate competition between 2-PG and 2,3-BPG at the active site, and one would have expected that the competition with 2,3-BPG would decrease the V_{max} and k_{cat} values. However, both the V_{max} and k_{cat} values were increased even in the presence of saturating 2,3-BPG concentration. This phenomenon can be explained by the binding of 2-PG to an allosteric or non-catalytic site at low activator concentration, while the enzyme is already bound to the substrate at the active site. However, as the concentration of 2-PG increases, 2-PG begins to compete with the substrate at the active site of the second monomer, resulting in the increase in the rate of 2,3-BPG hydrolysis on the active site of the first monomer.

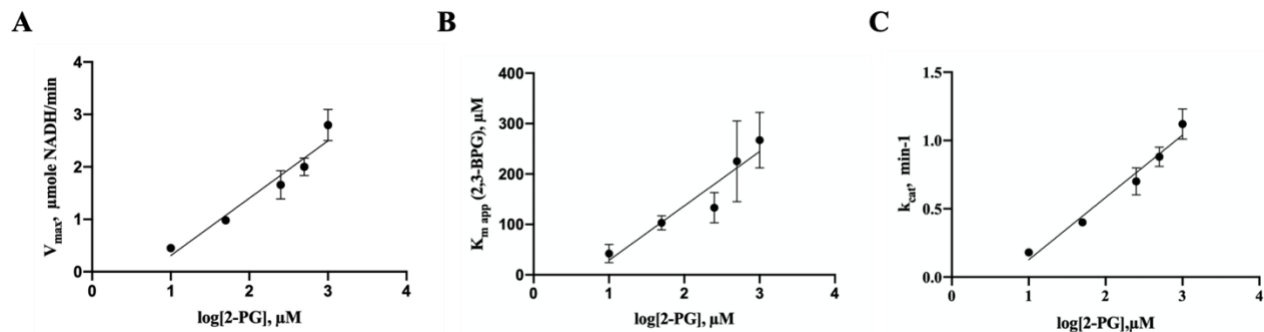


Figure 23. (A) The relationship between the V_{\max} and 2-PG concentrations (B) The relationship between the apparent K_m and 2-PG concentrations (C) The relationship between the apparent k_{cat} and 2-PG concentrations.

3.4. Discussion

3.4.1. BPGM synthase activity

The synthase activity is the main enzymatic activity of BPGM, and it proceeds with phosphorylation of His11 in the BPGM active site by the acyl phosphate substrate, 1,3-BPG.^{8,166} Following, the phosphoenzyme transfers the phosphoryl group to an acceptor molecule of 3-PGA to synthesize 2,3-BPG.^{8,9}



The synthase activity of BPGM was studied using a continuous coupled assay that coupled the BPGM activity with NADH production by GAPDH. The BPGM substrate, 1,3-BPG, is commercially unavailable as it is unstable and rapidly converts to 2,3-BPG, is synthesized in situ during the assay. GAPDH was therefore used to synthesize 1,3-BPG from a mixture of GAPDH,

GAP, and NAD. Also, the addition of 3-PGA to the reaction mixture of the assay was reported to be a requirement to maximize the synthase activity.¹⁶⁶ Hence, a concentration of 40 μM of 3-PGA was used in the assay, which is close to its physiological concentration (50-80 μM).¹⁸³

The synthase activity in our analysis was 0.07 μmole of NADH/min with specific activity of 8 μmole of NADH/min/mg, which is 2-fold lower than the reported specific activity of 16 U/mg.^{172,179} This difference may be due to different protein stock, different assay conditions or different 3-PGA concentrations used in the assay. The concentration used in our assay was 40 μM , while the reported assay used 100 μM .¹⁷⁹

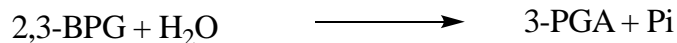
The physiological activator of BPGM phosphatase activity, 2-PG, has been reported to inactivate the synthase activity at high millimolar concentration.⁷ During our study we also observed such inhibition with 1 mM concentration of 2-PG as the synthase activity decreased from 0.07 μmole of NADH/min to 0.03 μmole of NADH/min. The inhibitory effect of 2-PG of the synthase activity was reported to be due to its binding at the active site; preventing binding of the phosphate acceptor, 3-PGA. Since the bound 2-PG does not accept phosphate molecule, it is going to stimulate the dephosphorylation of the phosphoenzyme to a neighboring active water molecule.¹⁶⁶ Also, based on our kinetic analysis of the 2-PG activation mechanism for phosphatase activity, we speculate that because the 3-PGA physiological concentration (50-80 μM) is higher than the 2-PG concentration (2-5 μM), 2-PG noncompetitively inhibits the synthase activity by binding to an allosteric site, lowering the binding affinity of 3-PGA, and stimulating the dephosphorylation of the phosphoenzyme. Thus, it inhibits the synthase activity.

The GAPDH•BPGM synthase assay has limitations in terms of studying the steady-state kinetics of the synthase activity. Michaelis-Menten kinetics for 1,3-BPG could not be obtained because of the unavailability and instability of this substrate. Also, the 1,3-BPG synthesized in situ

is not pure and might be mixed with 3-PGA, which could affect the accuracy of the kinetic analysis. However, regardless of the limitations, this assay can still be used to test the activity of the enzyme and the effect of modulators on the enzymatic activity.

3.4.2. BPGM phosphatase activity

The phosphatase activity of BPGM is inherently low unless activated by anions and 2-PG.^{154,166} The unstimulated phosphatase activity has been reported to be 1000-fold lower than the synthase activity of the enzyme.¹⁷¹ BPGM hydrolyzes 2,3-BPG into 3-PGA and P_i under certain physiological conditions to ensure regulation of 2,3-BPG level in the erythrocytes. In the literature, the phosphatase activity of BPGM was studied using radiolabeled activity assay and coupled enzymatic assay.^{170,172,179,184} In this work, BPGM phosphatase activity was measured using the previously reported PGK•GAPDH•BPGM coupled assay, and a non-radioactive malachite green colorimetric assay.



The malachite green assay is a well-established colorimetric assay that is used to quantify P_i released from phosphatase hydrolysis reaction. The assay is direct, fast and sensitive as it can detect as low as 1.6 picomoles of phosphate in the reaction mixture (Malachite Green assay kit; Sigma Aldrich). While the radioactive assay is also effective and sensitive, the use of radiolabeled substrates is expensive, and requires a laborious biochemical extraction and purification procedure for the protein substrate complex. Hence, the malachite green assay is considered the faster and cheaper alternative to the radioactive assay and it has an advantage as it can be adopted for high throughput screening.

The stimulation with low concentration of 2-PG (5 μM) resulted in 7-fold activation of the phosphatase activity (0.2 vs. 1.3 $\mu\text{mole P}_i$ /minute) (Table 2). The Michaelis Menten kinetics for 2,3-BPG in our analysis showed a K_m value of $97 \pm 7 \mu\text{M}$ and $39 \pm 13 \mu\text{M}$, in the absence and presence of 5 μM 2-PG, respectively (Table 2). The V_{max} also increased from 0.20 ± 0.04 to $0.70 \pm 0.12 \mu\text{mole P}_i/\text{minute}$ (corresponding to k_{cat} of 0.04 ± 0.02 to $0.30 \pm 0.01 \text{ minute}^{-1}$) in the absence and presence of 5 μM 2-PG (Table 2).

The second assay, the PGK•GAPDH•BPGM coupled enzymatic assay, was used as a secondary assay to test the kinetics of the phosphatase activity by coupling it to the two enzymes PGK and GAPDH. During the reaction, PGK converts 3-PGA (produced from the hydrolysis of 2,3-BPG by BPGM) to 1,3-BPG and regenerates ADP. GAPDH then consumes 1,3-BPG to oxidize NADH to NAD, which is measured spectrophotometrically by a decrease in the absorbance signal at 340 nm. Compared to the malachite green assay, this assay requires a higher concentration of enzyme and substrate for the activity to be detected. In the literature, this assay has always been carried out using 2-PG activation conditions.^{170,179}

Our study showed that phosphatase activity of 2,3-BPG hydrolysis in the absence of 2-PG was $0.030 \pm 0.003 \mu\text{mole NADH}/\text{minute}$ and it increased by 10-fold to $0.30 \pm 0.01 \mu\text{mole NADH}/\text{minute}$ in the presence of 10 μM 2-PG, clearly suggesting 2-PG to be an activator of the phosphatase activity (Table 3). The K_m , V_{max} and k_{cat} values of 2,3-BPG hydrolysis are listed in Table 3. Expectedly, BPGM affinity for 2,3-BPG increased from $77.9 \pm 1.7 \mu\text{M}$ to $43 \pm 3 \mu\text{M}$ in the absence and presence of 10 μM 2-PG, respectively. Likewise, there was a concomitant increase in V_{max} value from 0.2 ± 0.1 to 0.34 ± 0.01 (k_{cat} 0.05 ± 0.01 to $0.34 \pm 0.002 \text{ minute}^{-1}$), respectively (Table 3).

It is worth noting that steady-state kinetic parameters of the BPGM phosphatase activity in the literature vary widely depending on the assay type and condition. For example, the non-activated K_m of 2,3-BPG has been reported as 7 μM by Yu et al.,¹⁸⁴ $160 \pm 8 \mu\text{M}$ by Calvin et al.,¹⁷⁰ and 3.5 mM by Garel et al.¹⁷¹ The K_m of 2,3-BPG in the 2-PG activated system has also been reported to be 0.6 μM (with 20-60 μM 2-PG) by Rose and Liebowitz,¹⁵⁴ 25 μM (with 50 μM 2-PG) by Ravel et al.,¹⁷⁴ 41-71 μM (with 1 mM 2-PG) by Calvin et al.,^{170,171} and 25 μM (with 1.2 mM 2-PG) by Rose.¹⁸⁵ The apparent V_{max} also varies over a 500-fold range.¹⁵⁴

The results from the malachite green and PGK•GAPDH•BPGM assays used in this study also showed some significant variation to the published values above. However, the results obtained from both the malachite green assay and PGK•GAPDH•BPGM assays were within an acceptable range as the K_m for 2,3-BPG in the non-activated reaction was 97 μM and 77 μM , respectively. While in the 2-PG activated system, K_m for 2,3-BPG was 39 ± 13 (with 5 μM 2-PG in malachite green assay) compared to $43 \pm 3 \mu\text{M}$ (with 10 μM 2-PG in the coupled assay).

In conclusion, the malachite green assay will be used as a primary assay for the drug screening experiments and the PGK•GAPDH•BPGM coupled assay will be used as a confirmatory secondary assay.

3.4.3. 2-Phosphoglycolate activation mechanism of BPGM phosphatase activity

BPGM Phosphatase activity is activated by several anions such as chloride, phosphate, sulfite, and most potently, 2-PG.^{152,154} The activators' binding mode and their activation mechanisms are not clearly elucidated in the literature.^{152,154,167} The anion activated phosphatase activity showed a complex activation mechanism. Chloride and phosphate are known to stimulate

the phosphatase activity individually or in combination.¹⁵⁴ The activation by chloride and phosphate was competitively inhibited by low concentrations of 3-PGA suggesting the binding of anions in the active site.¹⁵⁴ In addition, the kinetic analysis of chloride activation in the presence of 2-PG showed that chloride acts as a noncompetitive inhibitor with respect to 2-PG activation.¹⁵⁷ Moreover, the kinetic analysis of phosphate activation in the presence of 2-PG showed a competitive inhibition against 2-PG activation.¹⁵⁴ It is noteworthy that the kinetic analysis of the phosphatase activation by phosphate alone suggested the existence of two binding sites for the phosphate, yet the second site location is yet to be determined.¹⁵⁴ Whether the binding of 2-PG is in the active site or in the second undetermined site is not conclusive.¹⁵⁴

Our kinetic analysis demonstrates that the activation mechanism by 2-PG has a mixed behavior, a combination of noncompetitive and competitive mechanism, which is in agreement with our crystallographic studies of BPGM in complex with 2-PG that will be discussed in chapter 4. In the co-crystal structures of BPGM with 2-PG, we observed two binding sites for 2-PG, one at the active site and the other at the dimer interface. Below, the activation mechanism of 2-PG is analyzed in terms of the inhibition kinetic model.

Different types of inhibitors are known to affect enzyme inhibition kinetics. Competitive inhibitors, which are in most instances structurally and chemically similar to the substrates, bind similarly as the substrate to influence the substrate binding affinity, but not the reaction velocity, which remains unchanged. In contrast, non-competitive inhibitors are usually structurally different from the substrates, binding at different site from the substrate site, resulting in reduction in the enzyme activity, while keeping the substrate binding affinity unchanged. Uncompetitive inhibitors, however, bind to the enzyme-substrate complex, influencing both the binding affinity of substrate and the catalysis of the reaction. There is a more complex system called mixed

inhibition that covers a wide range of behavior as it can result in competitive/noncompetitive or competitive/uncompetitive kinetics.

By analogy to the inhibitor model, the apparent increase in the binding affinity of 2,3-BPG with low 2-PG concentration (10 μM) with concomitant increase in V_{max} and k_{cat} (Table 4) is considered as noncompetitive activation, in which 2-PG binds to the enzyme at a site distinct than the substrate active site. However, the linear decrease in 2,3-BPG binding affinity with increasing 2-PG concentrations suggests a competitive mechanism at the active site (Figure 23B). Nevertheless, instead of the expected decrease in V_{max} and k_{cat} that usually happens during the competition of any ligand with the substrate at the active site, both V_{max} and k_{cat} values were observed to be increasing (Figure 23A and C). This observation is explained by the competition of 2-PG with the substrate binding at the active site of one monomer, rendering only the active site of the other monomer stimulated. On this basis, the activation mechanism was considered as mixed type activation, a hybrid of noncompetitive and competitive behavior. The mixed activation is complex to analyze and involves the activator binding to both free enzyme and enzyme-substrate complex with the activator having more affinity to one binding state over another. In our case, we postulate that 2-PG preferentially binds to the enzyme-substrate complex over the free enzyme since the physiological concentration of 2-PG is low (2-5 μM).^{186,187} At present, this is a working mechanism, and additional research and experiments are required to elucidate the precise mechanism of this activation.

CHAPTER 4

4. SPECIFIC AIM 2: Pursue X-ray crystallography studies to elucidate the atomic binding of 2-PG, 2,3-BPG and/or citrate with BPGM

X-ray crystallography is a powerful tool in structural biology and structure-based drug design. X-ray crystallography is used to determine the three-dimensional structure of small molecules, biological macromolecules and their complexes with other molecules. X-ray crystallography is also used as a tool in elucidating or understanding the function and mechanisms of macromolecules.¹⁸⁸

X-ray crystallography has been used to study BPGM in its unliganded form and in complex with its substrates (2,3-BPG and 3-PGA) to elucidate the enzyme reaction mechanisms, as well as determine the structural differences with its homologous glycolytic enzyme, phosphoglycerate mutase (PGAM1).^{160,161,189,190} In this chapter, structure elucidation of BPGM in complex with the phosphatase activator, 2-PG in the presence and absence of the substrate, 2,3-BPG, and the phosphatase inhibitor, citrate, will be presented. The binding mode and interaction of these two effectors with BPGM will help gain more insights into the mechanism of action of the phosphatase activity, and importantly help to design and develop potential modulators for BPGM activity for the treatment of diseases.

As pointed out previously, BPGM is an erythrocyte exclusive multifunctional enzyme whose main function is to regulate the concentration of 2,3-BPG levels in RBCs through two enzymatic activities (synthase and phosphatase). The synthase activity of BPGM is responsible for catalyzing the intermolecular phosphoryl transfer reactions to synthesize 2,3-BPG,^{8,166} while the phosphatase activity of BPGM is responsible for the hydrolysis of 2,3-BPG. The phosphatase

activity of BPGM is low and can be physiologically stimulated by the potent activator, 2-PG.¹⁵⁴ The activation mechanism of 2-PG and the mode of binding to BPGM are still not fully understood. The binding of 2-PG was postulated to be at the substrate active site.¹⁷⁴ In chapter 3, we have analyzed the kinetics of 2-PG activation mechanism, which revealed the activation mechanism of 2-PG to be a mixture of noncompetitive and competitive activation, suggesting the binding of 2-PG to the substrate active site and a second binding site. In order to understand the 2-PG stimulated phosphatase activity on atomic level and to locate the exact binding site of 2-PG, we co-crystallized the ternary complex of BPGM, 2,3-BPG and 2-PG and the binary complex of BPGM and 2-PG for structure determination.

The BPGM phosphatase inhibitor, citrate, is a red cell metabolite that has been reported to maintain erythrocyte 2,3-BPG levels when used as an additive in stored blood.¹⁹¹ Citrate is also known to be an inhibitor for other metabolic enzymes, such as 6-phosphofructo-2-kinase and isocitrate dehydrogenase.¹⁹² The exact binding mode of citrate to BPGM is unknown,¹⁹⁰ however, it has been proposed to bind at the active site of the enzyme, similar to 2,3-BPG binding mode since both ligands have similar size and electronic properties,^{190,193} and the fact that the published crystal structure of the homologous enzyme PGAM1 showed bound citrate at the active site (PDB ID 1YFK).¹⁹³ We therefore undertook structural studies to locate the exact binding site of citrate, which potentially could serve as target to design BPGM modulators.

4.1. Results

4.1.1. Crystallographic study of BPGM in complex with 2,3-BPG and 2-PG

To gain molecular insight into 2-PG activating effect on BPGM phosphatase activity, we set out to determine the ternary complex structure of BPGM with 2,3-BPG and 2-PG using X-ray crystallography. For the crystallization experiment, BPGM (30 mg/mL (1 mM)) was incubated with 3.8 mM 2,3-BPG and 7.6 mM 2-PG for 1 hour. Following, the complex was crystallized using the condition: 10% v/v Polyethylene glycol 200, 0.1 M BIS TRIS propane (pH 9), and 18% Polyethylene glycol 8000 (PEGRx 2, Hampton Research). The crystallization condition required no cryoprotectant. The X-ray diffraction data was collected at 100 K using a Rigaku MicroMax-007HF X-ray Generator and Eiger R 4 M Detector. The complex crystallized in the orthorhombic space group $P2_12_12_1$ with cell constant of $a=53.07 \text{ \AA}$, $b=70.86 \text{ \AA}$, $c=159.8 \text{ \AA}$, $\alpha=90.0^\circ$, $\beta=90.0^\circ$, $\gamma=90.0^\circ$. The data set was processed with CrysAlisPro 40.64.42a (Rigaku OD, Yarnton, Oxfordshire, England, 2015) and the CCP4 suite of programs to a resolution of 2.25 \AA .¹⁹⁴ The crystallization parameters are summarized in Table 5.

The crystal structure was determined with Phaser-MR (simple interface) molecular replacement with the Phenix software package¹⁹⁵ using the monomeric structure of BPGM complexed with 2,3-BPG (PDB ID 2H4Z) as a search model. Two monomeric molecules, forming the functional dimer were obtained per the asymmetric unit of the crystal. The solved structure underwent iterative cycles of refinement with the Phenix software along with refinement and model building using the COOT graphic program.^{195–197} The current refined structure has R_{work} and R_{free} of 20 and 27 % respectively. Detailed refinement parameters are reported in Table 5. The Ramachandran plot showed 96.3% of the residues are located in the favored area, and 3.5% in the allowed area with no outliers. As will be described later, even though BPGM was co-crystallized

with the substrate 2,3-BPG and the effector 2-PG, the resulting complex structure showed the product 3-PGA (instead of the co-crystallizing substrate 2,3-BPG) and the effector 2-PG bound to the protein. Hence, the ternary complex structure will be referred to as BPGM•3-PGA•2-PG complex.

The overall structure of the ternary BPGM•3-PGA•2-PG (Figure 24) is a homodimer with two identical monomers, A and B, that associate together by a two-fold non-crystallographic symmetry. There are two active sites that are located at the C-terminus portion of the α/β domain of each monomer. We observed significant portions of the C-termini of both monomers to be disordered and/or lack electron density, especially in monomer B. In monomer A, instead of 259 amino acids, we only observed residues from Ser2 to Val254, while in monomer B with more extensive disorder, we observed residue from Ser2 to Ile241.

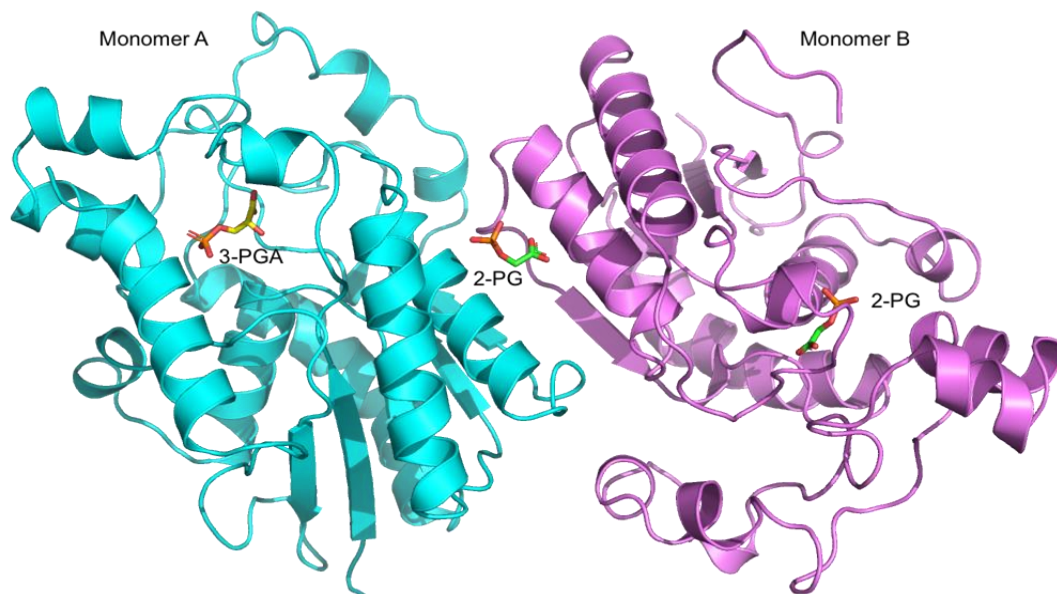


Figure 24. Overall structure of BPGM with bound 3-PGA in the active site of monomer A, 2-PG in the active site of monomer B, and 2-PG at the dimer interface.

Table 5. Crystallization and refinement parameters of ternary BPGM•3-PGA•2-PG complex structure.

Data set	BPGM•3-PGA•2-PG
Data collection	
Resolution range (Å)	26.18 - 2.25 (2.33 - 2.25) Å
Space group	P2 ₁ 2 ₁ 2 ₁
Unit cell dimensions [<i>a</i> , <i>b</i> , <i>c</i> (Å)]	53.07 70.86 159.8
Unique reflections	29143 (2912)
R _{merge} (%) ¹	13.955
Completeness (%)	98.53 (99.04)
Refinement	
R _{work}	0.20 (0.32)
R _{free} ²	0.27 (0.3)
r.m.s.d	
Bond length (Å)	0.008
Bond angles (°)	1.24
Molprobit statistics	
All atom clash score	6.1
Ramachandran plot (%)	
Favored	96.3
Allowed	3.5
Outliers	0.2
Rotamer outlier	0.00
Wilson B factor	33.23

¹ $R_{\text{merge}} = \frac{\sum_{hkl} \sum_i |I_i(hkl) - \langle I_i(hkl) \rangle|}{\sum_{hkl} \sum_i I_i(hkl)}$.

² R_{free} was calculated from 5% randomly selected reflection for cross-validation. All other measured reflections were used during refinement

The monomer A active site was well defined with a continuous electron density map; however, the monomer B active site showed significant disorder, in most part due to the lack of density at the C-terminal region that forms part of the active site. In the well-defined active site of monomer A, residues Arg100, Arg116, Arg117 (located at the entrance of the active site pocket), and the C-terminus residue, Gln251, were observed to move closer to the substrate, effectively closing the active site pocket. However, in monomer B, Arg100, Arg116 and Arg117 were disordered as evidenced by missing electron density of their side-chains. Moreover, the C-terminus residues beyond Ile241 were not resolved. It is clear that the active site of monomer B is in an open conformation while that of monomer A is in closed conformation.

Although, BPGM was co-crystallized with 2,3-BPG, in the monomer A active site, the electron density of the bound substrate clearly suggested 3-PGA (Figure **25A**), which is the hydrolysis product of 2,3-BPG. Hydrolysis of 2,3-BPG might have taken place during the complex incubation and/or during the crystallization experiment as observed by the disappearance of the 2-phosphoryl group of 2,3-BPG, as well as the unphosphorylated His11 in the active site of monomer A. As noted above, binding of 3-PGA resulted in a closed active site. Interestingly, in monomer B, where we observed an open active site conformation with significant disorder, the bound substrate corresponded to 2-PG (Figure **25B**)

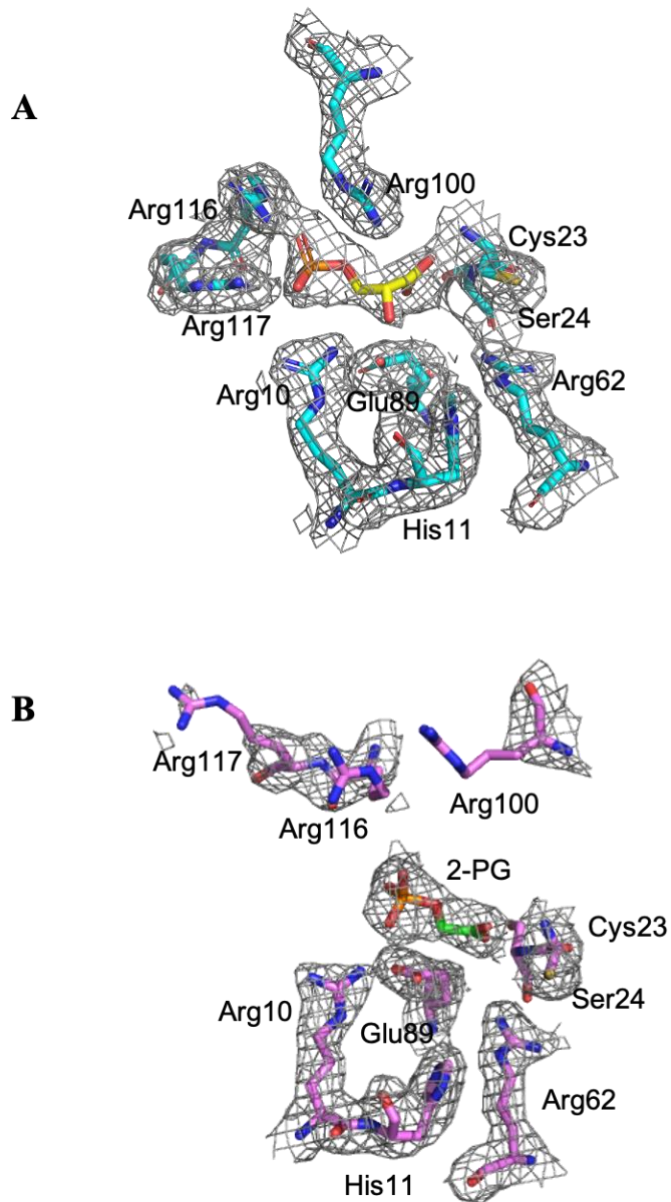


Figure 25. (A) Electron density map of BPGM with 3-PGA bound at monomer A active site. (B) Electron density map of BPGM with 2-PG bound at monomer B active site. The final $2F_o - F_c$ refined electron density map contoured at 0.8σ . Note how R116 and R100 are disordered in monomer B while ordered in monomer A.

Atomic interactions of 3-PGA with the active site residues in monomer A (Figure **26A**) were similar to the previously published binary BPGM•3-PGA co-crystal structure by Wang et al. (PDB ID 2H4X).¹⁶¹ The 3-PGA phosphoryl oxygen atoms (Figure **26A**) interact with the guanidino group of Arg116 and Arg117, the amide of Asn190, and the hydroxyl of Tyr92. In addition, the phosphoryl oxygen atom forms a direct hydrogen-bond interaction with the guanidino group of Arg100. The hydroxyl of 3-PGA makes a direct hydrogen-bond interaction with the carboxyl of Glu89, and a weak interaction with the guanidino group of Arg10. The hydroxyl of 3-PGA also interacts with the residues at the bottom of the active site, including His11, Arg62, and Glu89 through hydrogen-bond interactions mediated by three water molecules. Lastly, the carboxyl of 3-PGA forms hydrogen-bond interactions with the main-chain nitrogen atoms of Ser24 and Cys23.

Figure **26B** depicts the molecular interactions of 2-PG at the active site of monomer B. In an almost similar fashion to the bound 3-PGA in monomer A, 2-PG phosphoryl oxygen atoms form hydrogen-bond interactions with the amide of Asn190, the hydroxyl of Tyr92, and the guanidino group of Arg10. The interactions with the guanidino group of Arg116, and Arg117 observed in monomer A were missing due to the disorder in their side-chains. The carboxyl of 2-PG makes direct hydrogen-bond interactions with the guanidine group of Arg100, and the main-chain nitrogen atoms of Cys23 and Ser24. The carboxyl of 2-PG also makes water-mediated interactions with Glu89, Asn190, and Gly189. However, unlike 3-PGA, 2-PG does not make any direct hydrogen-bond interactions with Glu89, nor water-mediated hydrogen-bond interactions with His11 and Arg62 since only one water molecule was found in monomer B.

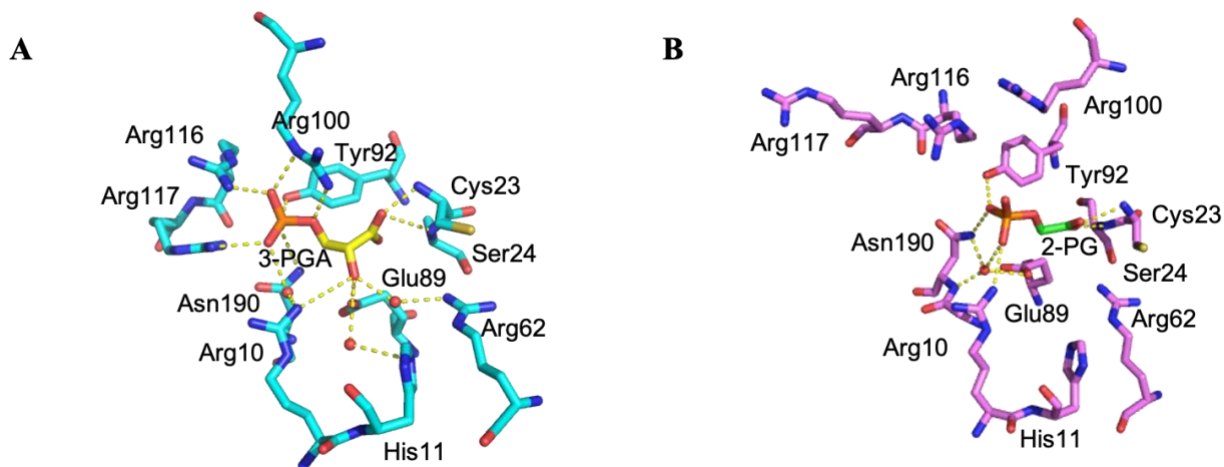


Figure 26. (A) Molecular interactions of 3-PGA at the monomer A active site of BPGM. (B) Molecular interactions of 2-PG at the monomer B active site of BPGM.

In a first of such reports, the ternary co-crystal structure showed 2-PG bound at the dimer interface of BPGM, close to the two-fold non-crystallographic axis (Figure 27A). The 2-PG makes interactions with His65 from both monomers, and Glu72 from monomer B. The phosphoryl oxygen atoms of 2-PG make direct hydrogen-bond interactions with the amide nitrogen of His65 in monomer A, and the oxygen atom of Glu72 in monomer B (Figure 27B). In addition, the carboxylate of 2-PG interacts through water-mediated interaction with the amide nitrogen atom of His65 residue in monomer B (Figure 27B).

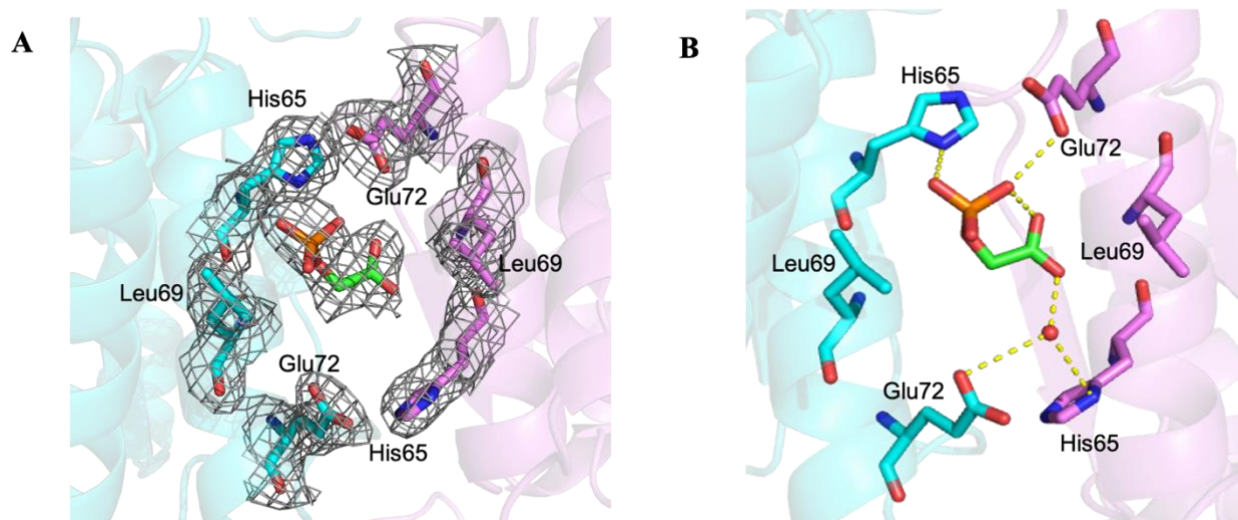


Figure 27. (A) Electron density map of BPGM with 2-PG bound at the dimer interface. The final $2F_o - F_c$ refined electron density map is contoured at 0.8σ . (B) Molecular interactions of 2-PG at the dimer interface of BPGM.

4.1.2. Crystallographic study of BPGM in complex with 2-phosphoglycolate

To confirm the binding mode of 2-PG to BPGM, we undertook a co-crystallization study of BPGM with 2-PG in the absence of 2,3-BPG. BPGM (30 mg/mL) was incubated with 2-PG (8.3 mM) for 1 hour. Following, the complex was crystallized using the same condition as described above for the ternary BPGM•3-PGA•2-PG complex, containing 10% v/v Polyethylene glycol 200, 0.1 M BIS TRIS propane (pH 9), and 18% polyethylene glycol 8000 (PEGRx 2, Hampton Research). The crystallization condition required no cryoprotectant. Like the ternary BPGM•3-PGA•2-PG complex, the binary BPGM•2-PG complex also crystallized in the orthorhombic space group of $P2_12_12_1$ with isomorphous unit cell dimension of $a=52.61 \text{ \AA}$, $b=70.95 \text{ \AA}$, $c=159.2 \text{ \AA}$, $\alpha=90.0^\circ$, $\beta=90.0^\circ$, $\gamma=90.0^\circ$. Data was collected to a resolution of 2.4 \AA . The refined ternary BPGM•3-PGA•2-PG complex without the bound ligand and water molecules was used as

a starting model to refine against the BPGM•2-PG complex data. Two molecules that form the functional dimer were found per asymmetric unit. The structure underwent iterative cycles of refinement with the Phenix software along with manual refinement and model building using the COOT program.^{195–197} Detailed crystallization and refinement parameters are summarized in Table 6.

The overall structure of the binary BPGM•2-PG complex was similar to the above described ternary BPGM•3-PG•2-PG complex structure. The activator, 2-PG, was observed bound to the active site of both monomers, A and B, and at the dimer interface of BPGM (Figure 28).

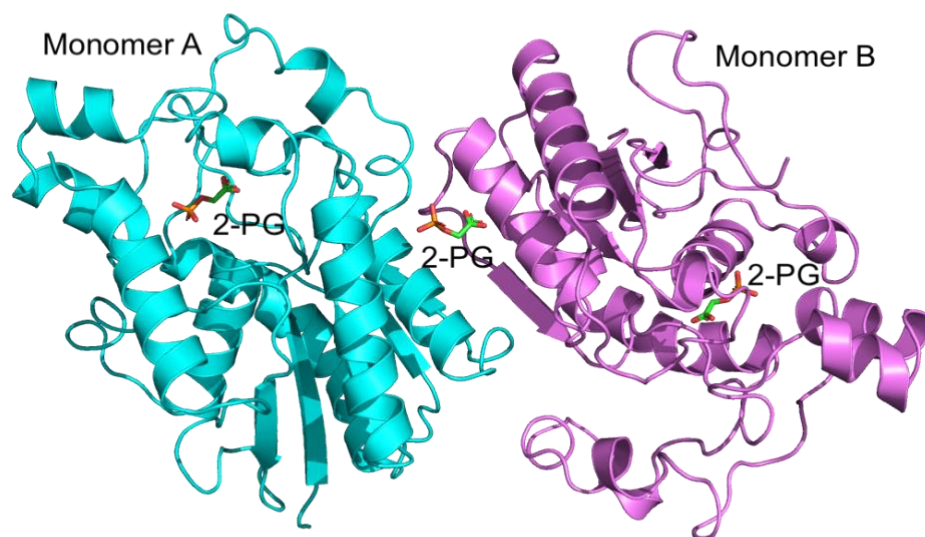


Figure 28. The overall structure of BPGM in complex with 2-PG at the active sites and dimer interface.

Table 6. Crystallization and refinement parameters of BPGM•2-PG complex structure.

Data set	BPGM•2-PG
Data collection	
Resolution range (Å)	29 - 2.48 (2.569 - 2.48) Å
Space group	P2 ₁ 2 ₁ 2 ₁
Unit cell dimensions [<i>a</i> , <i>b</i> , <i>c</i>] (Å)	52.6 70.8 159.00
Unique reflections	21758 (2115)
R _{merge} (%) ^a	12.85
Exposure time	32.85
Completeness (%)	99.65 (99.67)
Refinement	
R _{work}	0.21 (0.27)
R _{free} ^b	0.28 (0.37)
r.m.s.d	
Bond length (Å)	0.016
Bond angles (°)	1.57
Molprobit statistics	
All atom clash score	9.3
Ramachandran plot (%)	
Favored	93.29
Allowed	6.50
Outliers	0.20
Rotamer outlier	1.8

^a $R_{\text{merge}} = \frac{\sum hkl \sum i |I_i(hkl) - \bar{I}(hkl)|}{\sum hkl \sum i I_i(hkl)}$.

^b R_{free} was calculated from 5% randomly selected reflection for cross-validation. All other measured reflections were used during refinement

Like the ternary BPGM•3-PGA•2-PG complex, we also detected the absence of residues from the C-terminus of both monomers, but significant disorder was detected in monomer B as described above for the ternary BPGM•3-PGA•2-PG complex. Monomer A showed resolved residues from Ser2 to Val254, while monomer B showed only resolved residues from Ser2 to Ile245. Like the ternary BPGM•3-PGA•2-PG complex, the monomer B active site showed some disorder as evidenced by missing side-chain electron density of Arg100, Arg116, and Arg117 (Figure **29B**), while monomer A active site was well defined and ordered (Figure **29A**).

Also, as described above for the ternary BPGM•3-PGA•2-PG complex, monomer A active site in the binary BPGM•2-PG complex structure is in close conformation, trapping the 2-PG with the residues that guard the active site, including Arg100, Arg116, and Arg117, and Gln251 from the C-terminus (Figure **29A**).

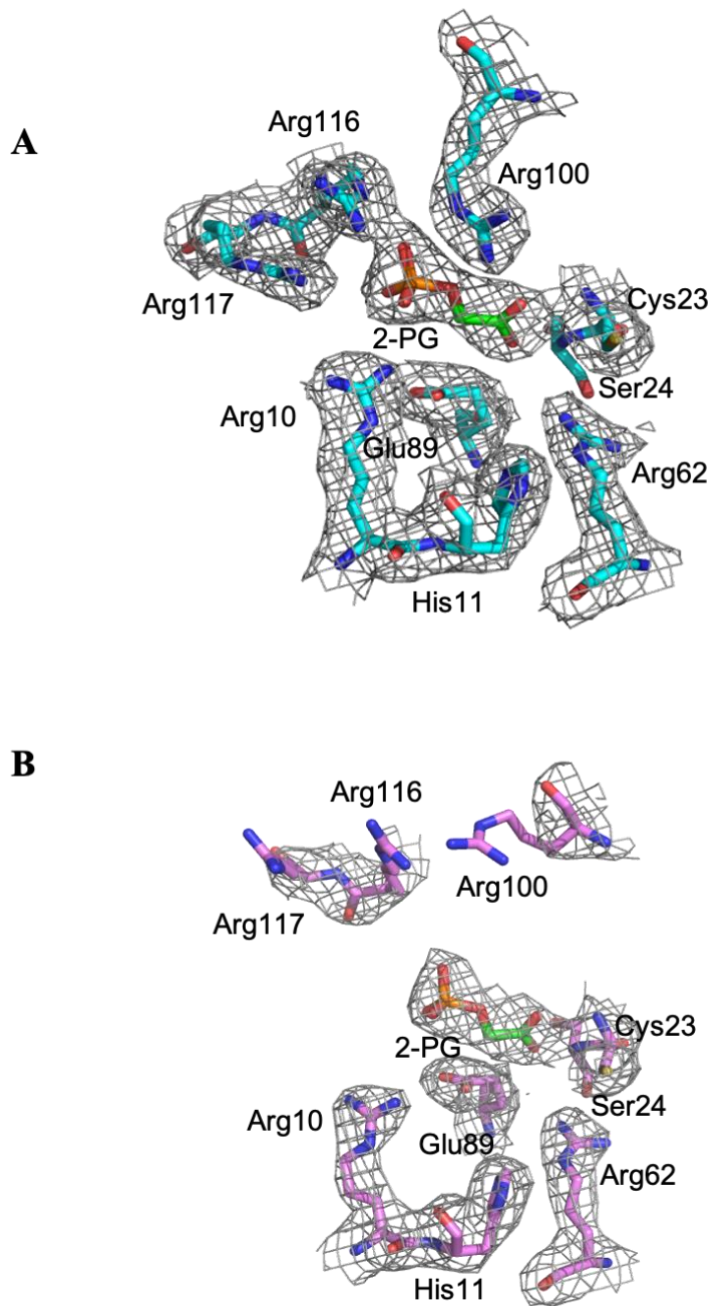


Figure 29. (A) Electron density map of BPGM with bound 2-PG at the active site of monomer B. (B) Electron density map of BPGM with bound 2-PG at the active site of monomer A. The final $2F_o - F_c$ refined electron density map contoured at 0.8σ .

Figure 30A represents the molecular interactions of 2-PG at the active site of monomer A. The 2-PG phosphoryl oxygen atoms make hydrogen-bond interactions with the guanidino group of Arg100, Arg116, Arg117, the amide of Asn190, and the hydroxyl of Tyr92. In addition, the phosphoryl oxygen atom forms water-mediated interactions with Asn190, Glu89, Arg10, and a direct hydrogen-bond interaction with the guanidino group of Arg100. The carboxyl group of 2-PG forms hydrogen-bond interactions with the main-chain nitrogen atoms of Cys23 and Ser24, and the guanidino of Arg100. As noted in monomer A of the ternary complex, two water molecules were found at the active site, facilitating the interaction between 2-PG and the residues Arg10, Glu89, Asn190, and Gln251. Unlike 3-PGA, 2-PG does not have a water-mediated interaction with Arg62 (Figure 30B).

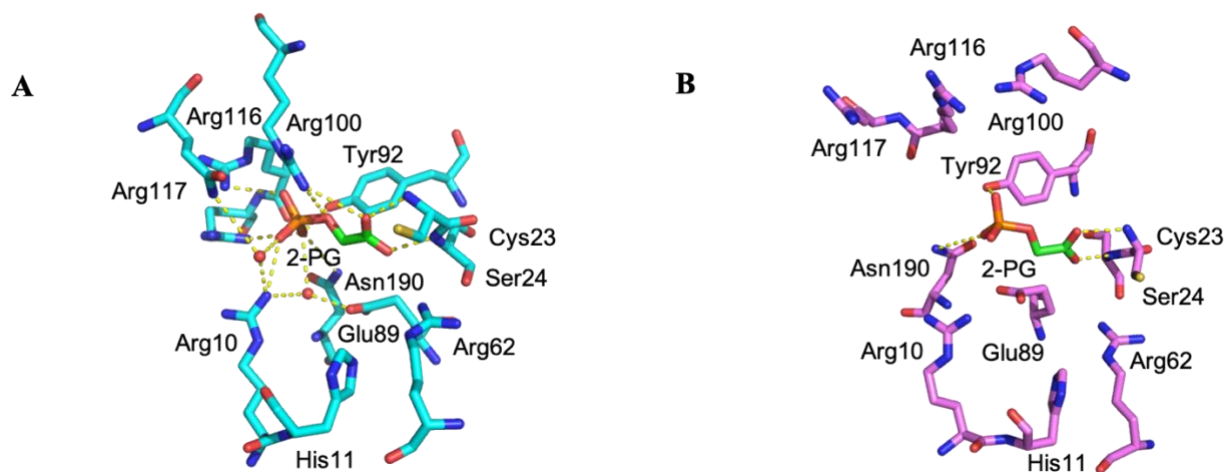


Figure 30. (A) Molecular interactions of 2-PG at the active site of monomer A. (B) Molecular interactions of 2-PG at the active site of monomer B.

In monomer B, the phosphoryl oxygen atoms of 2-PG form direct hydrogen-bond interactions with the amide of Asn190, and the hydroxyl of Tyr92 (Figure **30B**). As observed in monomer B of the ternary BPGM•3-PGA•2-PG complex, the interaction with Arg116, and Arg117 were missing due to disorder. Furthermore, the carboxyl of 2-PG makes hydrogen-bond interactions with the main-chain nitrogen atoms of Cys23 and Ser24. However, unlike 2-PG in monomer B of the ternary BPGM•3-PGA•2-PG complex, the carboxyl of 2-PG does not form any interaction with Arg100. Moreover, in a similar manner to monomer B of the ternary complex, the water-mediated interactions with the residues at the bottom of the active site, His11, Arg10 and Glu89, were not observed as the structural water molecules were missing due to disorder. It is clear that monomer B open site makes fewer interactions with 2-PG compared to the monomer A close active site.

The binary co-crystal structure also showed 2-PG bound at the dimer interface of BPGM, close to the two-fold non-crystallographic axis (Figure **31A**). It involves direct and water-mediated interactions between 2-PG and the His65 and Glu72 residues. The phosphoryl oxygen atoms interact through water-mediated hydrogen-bond interaction with the amide nitrogen atom of His65 residue in monomer A, in contrast to the direct hydrogen-bond observed in the ternary BPGM•3-PGA•2-PG complex. The carboxylate of 2-PG, however, makes water-mediated interactions with only His65 of monomer B, unlike the carboxylate of the ternary BPGM•3-PGA•2-PG complex that makes water-mediated interaction with both His65 and Glu72 (Figure **31B**).

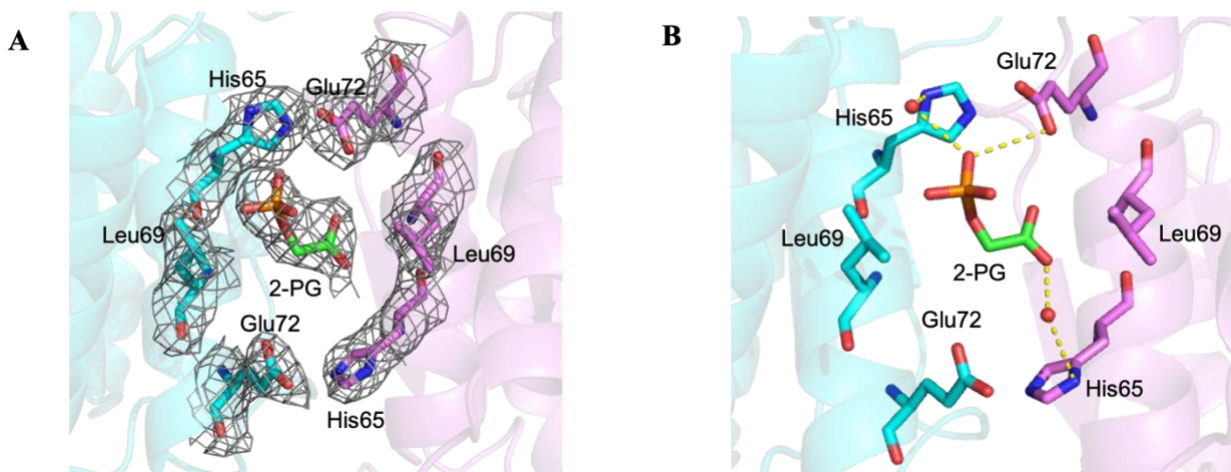


Figure 31. (A) Electron density map of BPGM with bound 2-PG at the dimer interface with final $2F_o - F_c$ refined electron density map contoured at 0.8σ . (B) Molecular interactions of 2-PG at the dimer interface.

4.1.3. Crystallographic study of BPGM in complex with citrate

Citrate has been reported to act as a BPGM phosphatase inhibitor. In order to elucidate the binding interaction of citrate to BPGM, a crystal of the binary BPGM•citrate complex was obtained with high concentrations of citrate. BPGM at a concentration of (30 mg/mL) was crystallized in 1000 mM Sodium citrate tribasic, 100 mM Sodium cacodylate/hydrochloric acid (pH 6.5) (Wizard classic 1, Rigaku). A crystal in the orthorhombic space group $P2_12_12$ space group with unit cell dimension of $a=129.3 \text{ \AA}$, $b=99.6 \text{ \AA}$, $c=38.4 \text{ \AA}$, $\alpha=90.0^\circ$, $\beta=90.0^\circ$, $\gamma=90.0^\circ$ was obtained. The crystal parameter is different from those of the previous two structures ($a=52.61 \text{ \AA}$, $b=70.95 \text{ \AA}$, $c=159.2 \text{ \AA}$, $\alpha=90.0^\circ$, $\beta=90.0^\circ$, $\gamma=90.0^\circ$). The two monomers that form the functional dimer were seen in the asymmetric unit. Data were collected to a resolution of 2.3 \AA . The structure was determined by Phaser-MR (simple interface) molecular replacement with the Phenix software

package¹⁹⁵ using the monomeric structure of BPGM in complex with 2,3-BPG (PDB ID 2H4Z) as a search model. Data collection and refinement parameters are summarized in Table 7.

Unlike the above ternary BPGM•3-PGA•2-PG and binary BPGM•2-PG complexes that showed only significant disorder at the C-terminus of monomer B, the C-terminus of both monomers of the binary BPGM•citrate complex are equally disordered, missing residues beyond Gly236. In another significant difference from the previous two structures, the structure of the binary BPGM•citrate complex showed only a bound citrate in monomer A and not monomer B (Figure 32). Like BPGM•3-PGA•2-PG and BPGM•2-PG complexes, the BPGM•citrate complex also showed bound citrate at the dimer interface, in a similar position as the bound 2-PG.

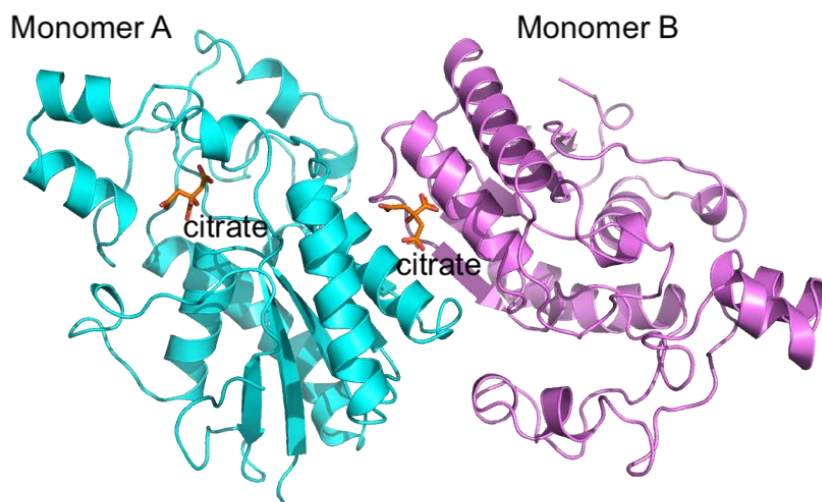


Figure 32. The overall structure of BPGM in complex with citrate at the active site and the dimer interface.

Table 7. Crystallization and refinement parameters of BPGM•citrate complex structure.

Data set	BPGM•citrate
Data collection	
Resolution range (Å)	28.68 - 2.3 (2.382 - 2.3) Å
Space group	P2 ₁ 2 ₁ 2
Unit cell dimensions [a,b, c (Å)]	129.3 99.6 38.4
Unique reflections	22872 (2263)
R _{merge} (%) ^a	15.16
Completeness (%)	99.83 (100.00)
Refinement	
R _{work}	0.21 (0.27)
R _{free} ^b	0.25 (0.35)
r.m.s.d	
Bond length (Å)	0.008
Bond angles (°)	1.01
Molprobit statistics	
All atom clash score	8.72
Ramachandran plot (%)	
Favored	95.68
Allowed	4.10
Outliers	0.22
Rotamer outlier	0.47

^a $R_{\text{merge}} = \frac{\sum hkl \sum i |I_i(hkl) - \bar{I}(hkl)|}{\sum hkl \sum i I_i(hkl)}$.

^b R_{free} was calculated from 5% randomly selected reflection for cross-validation. All other measured reflections were used during refinement

Another significant difference from the ternary BPGM•3-PGA•2-PG and binary BPGM•2-PG complex structures is that monomer A of BPGM•citrate complex with the bound citrate was in a partially closed conformation due to disorder at the C-terminus region (Figure **33A**). The atomic interactions of citrate at the active site of monomer A showed that one carboxylate group makes direct hydrogen-bond interactions with guanidino of Arg116, amide of Asn190, hydroxyl of Tyr92 (Figure **33B**). The second carboxylate group makes hydrogen-bond interactions with the guanidino of Arg10. Similarly, the third carboxylate group makes hydrogen-bond interactions with the guanidino of Arg100, and its main chain nitrogen with Ser24, Cys23 (Figure **33B**). The side-chain of Arg117 was disordered, making it difficult to locate its actual orientation. As noted above, the missing C-terminus residues beyond Gly236 resulted in a partially closed active site conformation, which is in contrast to the ternary BPGM•3-PG•2-PG and binary BPGM•2-PG complex structures that were characterized by closed active sites in monomer A. No structural water molecules were found at the active site of monomer A. In monomer B, no apparent bound citrate was found, and the side-chain of several residues in the active site, including Arg100, Arg116, and Arg117 were disordered as evidenced by lack of electron density.

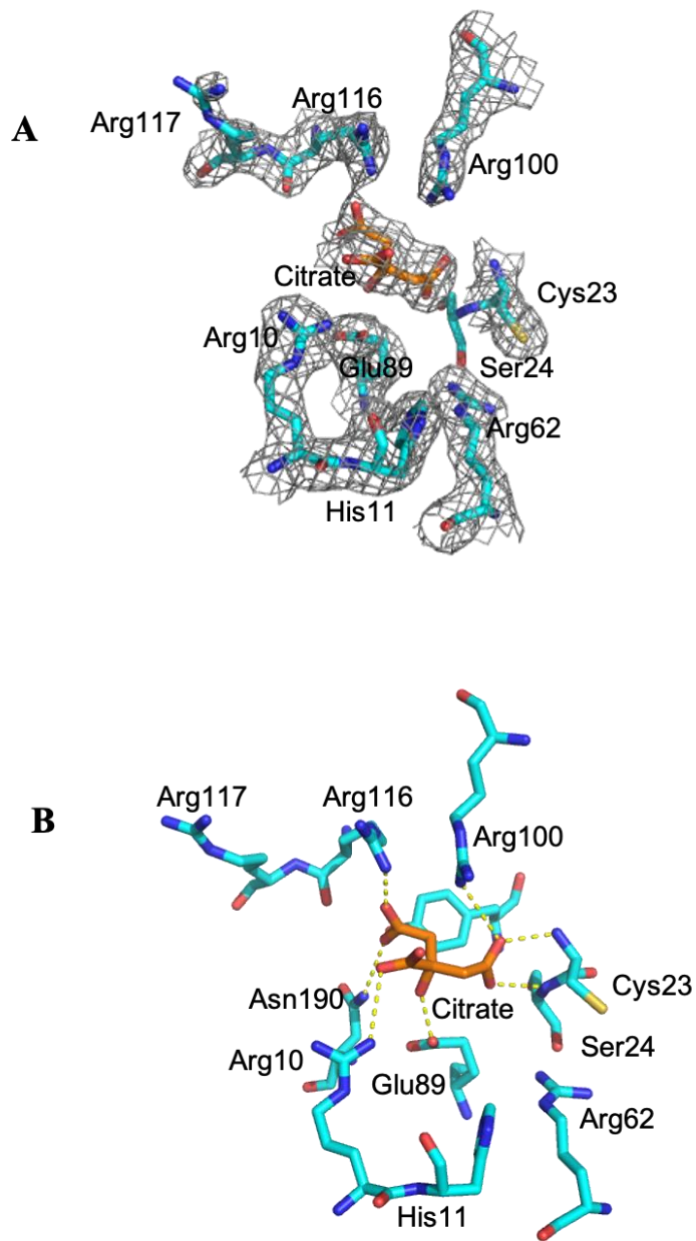


Figure 33. (A) Electron density map of *BPGM* with bound citrate at the active site of monomer A with the final $2F_o-F_c$ refined electron density map contoured at 0.8σ . (B) Molecular interactions of citrate at the active site of *BPGM*.

The bound citrate at the dimer interface is involved in direct hydrogen-bond interactions with His65 and Glu72 from both monomers (Figure 34A and B). It also makes water-mediated hydrogen-bond interaction with His65 of monomer A and a direct hydrogen-bond interaction with His65 of monomer B. In addition, citrate has direct hydrogen-bond interactions with Glu72 of both monomers. It appears that citrate makes more interactions at the dimer interface than 2-PG in the ternary BPGM•3-PGA•2-PG or binary BPGM•2-PG complex structures.

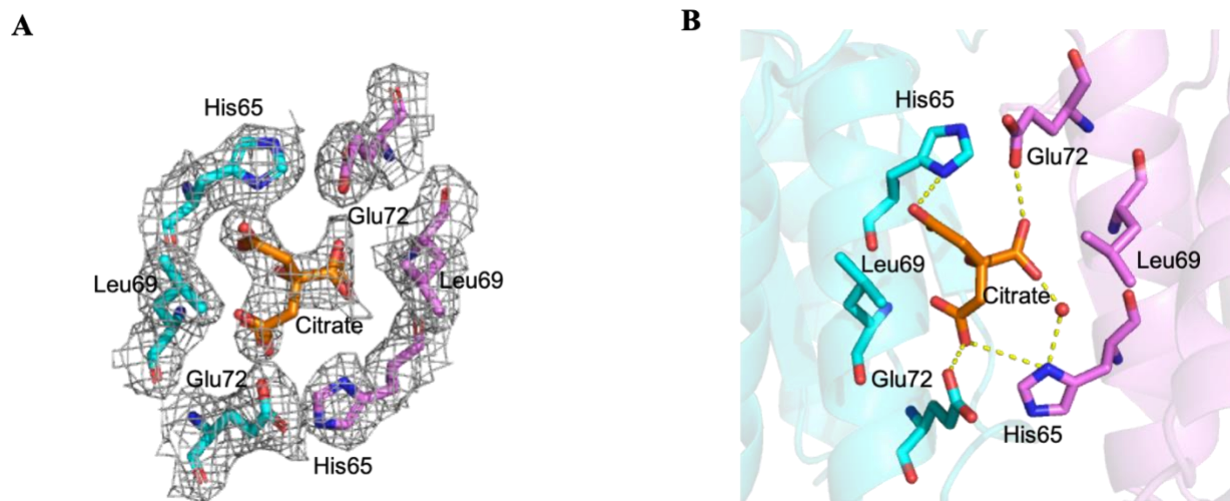


Figure 34. (A) Electron density map of BPGM with bound citrate at the dimer interface of BPGM with the final $2F_o - F_c$ refined electron density map contoured at 0.8σ . (B) Molecular interactions of citrate at the dimer interface of BPGM.

4.1.4. Identification of allosteric sites on BPGM surface using FTMap

A computational solvent mapping tool was utilized using the FTMap online server (<http://ftmap.bu.edu/>) to search for potential binding sites, including allosteric sites on the BPGM surface, and to assess their druggability.^{198,199} FTMap mimics the multiple solvent crystal structures (MSCS) approach, which is a crystallographic fragment screening method. However, FTMap uses a fast Fourier transform (FFT) algorithm for fragment screening. This method is based on the premise that fragment screening identifies hotspots or consensus sites (CSs), which are regions on the protein surface that contribute highly with binding interactions between protein and ligand, by identifying the sites where clusters of different fragments or probes bind.^{198,199} The site with the highest number of probes and clusters is likely considered to be druggable.^{198,199}

The unliganded crystal structure of BPGM (PDB ID 3NFY) was uploaded to the server for analysis. FTMap then docked the entire protein surface with 16 small molecular probes including, ethanol, isopropanol, isobutanol, acetone, acetaldehyde, dimethyl ether, cyclohexane, ethane, acetonitrile, urea, methylamine, phenol, benzaldehyde, benzene, acetamide, and N,N-dimethylformamide, with millions of different poses to identify the most energetically favorable binding pose for each probe. Next, each probe type was clustered into CSs according to their average free energy. The CSs are then ranked on the basis of the number of probe clusters bound, with the highest number of probe clusters predicting a primary hot spot.²⁰⁰ The output result in the form of protein structure with bound probe clusters can be visually inspected using PyMOL (Figure 35A). The result also includes two contact bar graphs, displaying the contact rate of each residue with the probe molecules as a percent of total contacts. The first graph (Figure 35B)

corresponds to the hydrogen-bond interaction and the second graph (Figure **35C**) is for other non-bonded interactions.

The result showed the existence of seven CSs (Figure **35A**). The dimer interface site, denoted as CS0, was predicted to be the top-ranked site with the highest number of bound probes, which equaled to 19 molecular probes. Notably, the binding of at least 16 molecular probes is a requirement for a site to be druggable.²⁰⁰ The second predicted site, denoted as CS1, located at the substrate active site of monomer A was found bound to 13 molecular probes (Figure **35A**). The third and fourth sites, CS2, and CS3 were found bound to 12 molecular probes and are located at a site surrounded by Val59, Trp78, Ser84 Arg141, and Cys145, and at the active site of monomer B, respectively. The remaining sites CS4, CS5, and CS5 have lower number of probe clusters bound to each site, suggesting low druggability (Figure **35A**).²⁰⁰

The first contact graphs showed His65 from both monomers and Tyr92 from monomer A participating in the highest number of hydrogen-bond interactions with the probe molecules (Figure **35B**). The second contact graph demonstrated Trp68 from monomer A, followed by Phe22 from monomer A, and Trp68 from monomer B with the highest percentage of non-bonded contact score with the probe molecules (Figure **35C**). All residues, His65, Tyr92, Trp68, and Phe22, are located at CS0, the dimer interface site, which clearly support the crystallographic studies that indicate the dimer interface site to be a potentially druggable site.

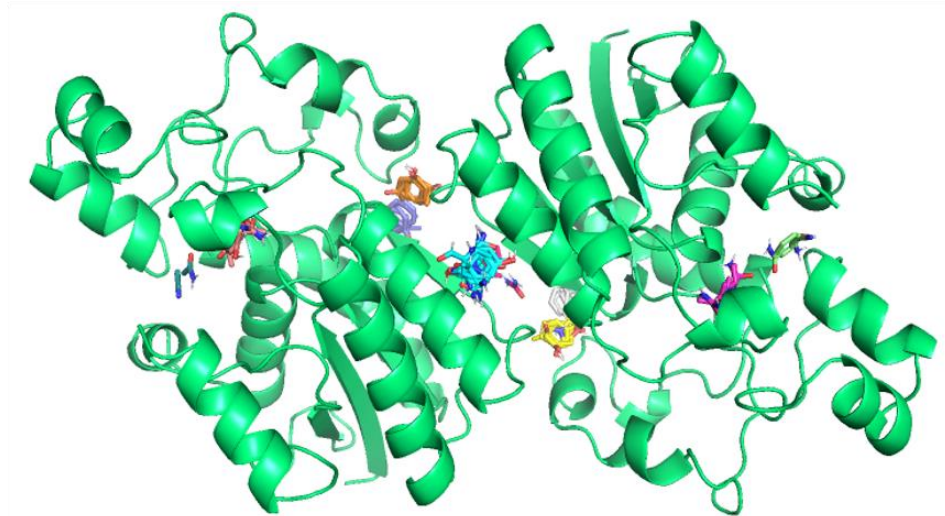
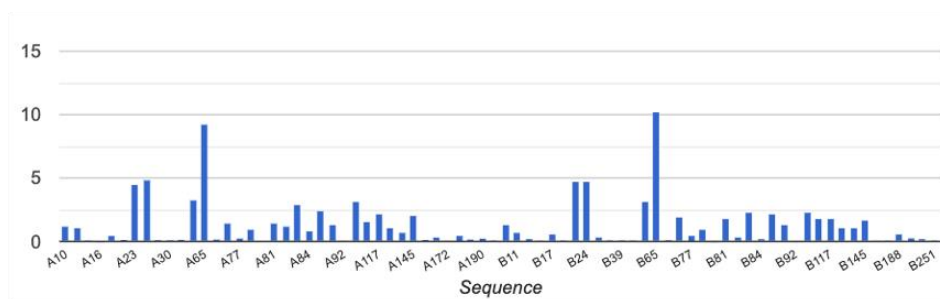
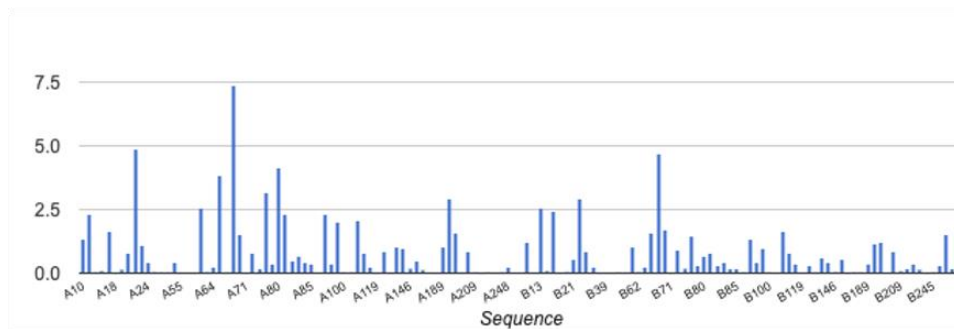
A**B****C**

Figure 35. FTMap output **(A)** Bound probe molecules to consensus sites on unliganded BPGM surface (PDB ID 3NFY); CS0 (cyan, 16 probe clusters), CS1 (magenta, 13), CS2 (yellow,12), CS3 (wheat, 12), CS4 (white, 8), CS5 (purple, 8), and CS6 (orange, 7). **(B)** Contact graph for hydrogen-bond interactions **(C)** Contact graph for nonbonded residue interactions.

4.2. Discussion

4.2.1. Overall structure comparison of the unliganded BPGM, binary BPGM•2-PG complex and ternary BPGM•3-PGA•2-PG complex

The crystal structures of BPGM complexed with the activator 2-PG, as well as complexed with 2-PG and 2,3-BPG have been determined to resolutions of 2.4 and 2.25 Å, respectively. The former structure showed a binary BPGM•2-PG complex, while the latter showed a ternary BPGM•3-PGA•2-PG complex. It became clear that that 2,3-BPG was hydrolyzed to the product 3-PGA during the crystallization of the ternary complex. Both structures were found to be missing the initiating methionine residue. Monomer A of the ternary BPGM•3-PGA•2-PG and binary BPGM•2-PG crystal structures showed resolved residues from Ser2 to Val254, while monomer B only showed resolved residues from Ser2 to Ile241, and Ser2 to Ile245, respectively. The C-terminus residues beyond Gly236 residues were disordered as evidenced by weak electron density, while residues beyond 241 of the ternary BPGM•3-PGA•2-PG and 245 of the binary BPGM•2-PG complexes were completely missing in the electron density.

The active site of monomer B also showed some disorder, especially with the side-chain of Arg100, Arg116, Arg117 located at the mouth of the active cleft. These residues are highly flexible and have been shown to exhibit significant movements, particularly Arg117, during substrate binding.¹⁹⁰ The movement of these residues upon substrate binding along with their interaction with the C-terminal tail residues helps maintain the active site in a catalytically active closed conformation.

It is also noteworthy that the C-terminus is a conserved domain in the homologous phosphoglycerate mutase enzyme 1 (PGAM1) and have been demonstrated to play an important role in the functional activities of the enzymes, including binding of substrates, stabilization of the

phosphorylated enzyme intermediate, and the release of the product by transitioning between open and closed conformations of the active site.^{201,202} The deletion of a minimum of seven residues at the C-terminus portion has been shown to abolish the three catalytic activities of BPGM (synthase, phosphatase, and mutase).¹⁵⁹

The disorder observed at the C-terminus of BPGM is well documented in the literature due to the dynamic nature and high degree of flexibility of this region. When the C-terminus is resolved as observed in monomers A of the ternary BPGM•3-PGA•2-PG complex, and the binary BPGM•2-PG complex, as well as in the previously published structures of BPGM in complex with 2,3-BPG (PDB ID 2H4Z), and BPGM in complex with 3-PGA (PDB ID 2H4X),¹⁶¹ the side-chain of Gln251 is observed to be directed toward the center of the active site pocket making interactions with the bound substrate, as well as with Arg100 and Arg116.¹⁶⁰ These interactions help constrain the flexibility of Arg100 and Arg116 side-chains, and fix the active site into a closed conformation, which is required for catalysis.¹⁶⁰ Expectedly, absence of the above described Gln251-mediated interactions with Arg100 and Arg116 in monomers B of the ternary BPGM•3-PGA•2-PG and binary BPGM•2-PG complex structures, as well as in both monomers of the binary BPGM•citrate complex structure, have led to significant disorder of the C-termini, resulting in open active site conformations in these structures. Also, expectedly, BPGM structures without bound substrate or ligand at the active site, e.g., the unliganded structure of BPGM (PDB ID 3NFY),¹⁹⁰ has C-termini disorder with open active site conformations. Similar observations have been reported for the unphosphorylated/unliganded form of the homologous PGAM1 enzyme as the last 9 residues of the C-terminal tail were found to be missing electron density.¹⁶⁰ These observations showed that the unphosphorylated and/or the unliganded state of the enzyme exhibits more disordered C-terminus residues than the bound or reacting conformation of the enzyme, where the C-terminal

residues are found well defined and covering the active site and maintaining the catalytically active conformation. It is also clear that not all bound ligands at the active site led to resolution of the C-termini or closed active site conformation as observed in monomer B of the ternary BPGM•3-PGA•2-PG complex, monomer B of the binary BPGM•2-PG complex, and both monomers of the binary BPGM•citrate complex.

Quite interestingly, the ternary BPGM•3-PGA•2-PG and the binary BPGM•2-PG complexes revealed a novel binding site for 2-PG at the dimer interface. It thus appears that 2-PG is capable of binding to both the active site and a non-catalytic site at the dimer interface. The bound 2-PG at the dimer interface specifically makes interactions with His65 residues from both monomers and Glu72 from monomer B, that may potentially affect monomer-monomer cooperativity, either by stabilizing or destabilizing the monomer-monomer contact. Interestingly, the existence of an alternative binding site for 2-PG is in agreement with our kinetic analysis of the 2-PG activation mechanism reported in chapter 3. Our results showed that 2-PG exhibits a mixed noncompetitive and competitive mechanism suggesting the binding of 2-PG to the active site as well to an alternative modifier site. The latter appears to be at the dimer interface.

Interestingly, a chloride ion was reported bound at the dimer interface (near the 2-fold axis) of PGAM1 in complex with citrate (PDB ID 1YFK), interacting with Trp68 and Arg83.¹⁹³ Chloride ions have been demonstrated to activate the phosphatase activity of the PGAM1 enzyme as well as BPGM as observed by lowering the apparent K_m of 2,3-BPG.^{154,203} In the PGAM1, chloride has also been shown to be a competitive inhibitor to the activation of 2-PG. Thus, it was postulated that 2-PG and chloride bind to an alternative undetermined site separate from the substrate active site.²⁰³

Binding of 2-PG at the dimer interface appears not to induce any significant conformational changes at the interface region as observed by low RMSD value of ~ 0.4 Å when the dimer interface of the unliganded BPGM structure (PDB ID 3NFY) was superposed with the dimer interface of the ternary BPGM•3-PGA•2-PG complex and binary BPGM•2-PG complex structures. Similarly, the RMSD was ~ 0.3 Å, when the dimer interface of the unliganded BPGM structure was superposed with the BPGM•3-PGA (PDB ID 2H4X) and BPGM•2,3-BPG (PDB ID 2H4Z) complex structures. Note that, unlike 3NFY, 2H4X and 2H4Z, our liganded structures contain bound 2-PG ligand at their dimer interface. It appears that 2-PG binding at the dimer interface causes a long-range effect at the active site of the second monomer. Both active sites in 2H4X and 2H4Z are in the closed conformation, the former with 2,3-BPG bound in both active sites, and the latter with 3-PGA bound in both active sites. Our two structures with a bound ligand at the dimer interface, even though show both active sites occupied by ligands, only monomer A is in the closed conformation, while monomer B is in the open.

Interestingly, in the ternary BPGM•3-PGA•2-PG complex we only observed 3-PGA bound to monomer A active site, with 2-PG bound to monomer B active site. From the foregoing, it appears that the binding at the dimer interface exerts changes in the dynamics of the protein, and the flexibility of the active site residues, both of which can affect the binding affinity of the substrate in the second subunit without significant conformational changes at the dimer interface region. This is the first such crystallographic report of a dimer interface binding.

4.2.2. Active site comparison of the unliganded BPGM and ternary BPGM•3-PGA•2-PG complex

As previously mentioned, 3-PGA binds in the active site of monomer A in the ternary BPGM•3-PGA•2-PG complex structure. Structural water molecules were observed mediating and

strengthening the interactions between the bound 3-PGA and the active site residues Arg10, His11, Glu13, Arg62, Glu89, and His188. These water-mediated interactions are missing in monomer B with the bound 2-PG, in part due to disorder. Similarly, in monomer A of the binary BPGM•2-PG structure, 2-PG was observed to interact with the active site residues through two structural water molecules. While in monomer B, the binding of 2-PG was weak and no structural water molecules were found to facilitate the interactions with the residues at the bottom of the active site. It is clear that the two monomers of the ternary BPGM•3-PGA•2-PG complex and binary BPGM•2-PG complex bind to substrates with different affinities.

Close inspections of the active site of monomer A of the ternary BPGM•3-PGA•2-PG and binary BPGM•2-PG complexes in comparison with the active site of monomer A of the unliganded structure (PDB ID 3NFY) suggested that binding of substrate leads to significant movement of the loop from His11 to Ser24 at the bottom of the active site pocket toward the substrate (Figure **36A** and **B**). In addition, the side-chain of Glu13 of the ternary BPGM•2,3-BPG•2-PG and binary BPGM•2-PG complex showed a significant conformational change upon ligand binding. The side-chain of Glu13 swings outward away from the active site, making contacts with Glu33 and Lys18 at the surface of the protein (Figure **36A** and **B**), in contrast to the unliganded BPGM, where the side-chain of Glu13 is directed toward the active site making several water-mediated interactions with Arg10, His11, Glu89 and Gly189. These conformational changes are important to accommodate the binding of the substrate and to expose the phosphorylation site at the bottom of the active site for catalysis.

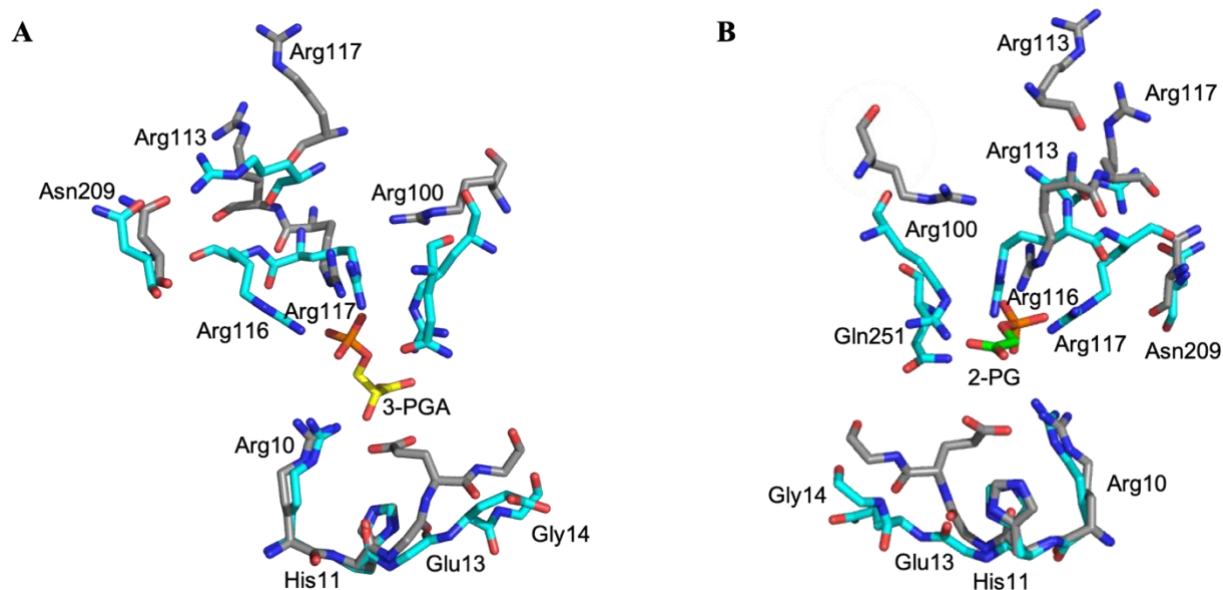


Figure 36. (A) Superposition of the important residues in the active site of monomer A of the ternary BPGM•3-PGA•2-PG complex (cyan) and unliganded BPGM (PDB ID 3NFY; gray) structures. (B) Superposition of the important residues in the active site of monomer A of the binary BPGM•2-PG complex (cyan) and unliganded BPGM (gray) structures.

Another significant difference was observed in the main-chain residues from Arg99 to Thr122 located at the entrance of monomer A active site. These amino acids were observed to move toward the active site placing the side-chains of Arg100, Arg116, and Arg117 into the active site (Figure 36A and B). The conformation of Arg117 is stabilized by hydrogen-bond interactions between the side-chain of Arg117 and Thr211. Moreover, Arg113 showed a large movement to make interactions with Asn209. Also, the C-terminal residues beyond Gly236 stretch forward and close the active pocket, thus maintaining the active site in the catalytically closed conformation.

These interactions were missing in the unliganded structure, making the unliganded structure appear to be in an open catalytically inactive conformation.

Structural comparison of the active site of monomer B of the ternary BPGM•2,3-BPG•2-PG or binary BPGM•2-PG complexes with the unliganded structure (PDB ID 3NFY) showed conformational changes of the residues at the bottom of the active site from His11 to Ser24 in a similar fashion as described for monomer A in which the side-chain of Glu13 has significant movement, exposing the phosphorylation site at the bottom of the active for catalysis (Figure **37A** and **B**). However, unlike monomer A, but similar to the unliganded structure, the residues at the entrance of the active site, Arg100, Arg116, and Arg117, were highly disordered making it difficult to determine their side-chain direction and interactions. Furthermore, the hydrogen-bond interaction between the Arg113 with Asn209 observed in monomer A of the ternary BPGM•3-PGA•2-PG and binary BPGM•2-PG complex structures was absent in monomer B. In addition, the C-terminus residues beyond Ile-240 in monomer B of the ternary BPGM•2,3-BPG•2-PG and beyond Ile-245 in the binary BPGM•2-PG were missing. It should be noted that the C-terminus of the unliganded structure was resolved up to Asp250. The observed significant disorder of the residues at the entrance of the active site and at the C-terminus made the active site of monomer B appear to be in an open conformation resembling the catalytically inactive open active site of the unliganded structure. The open active site conformation of monomer B therefore reflects weak binding of 2-PG to monomer B active site in contrast to the high affinity binding of 2-PG to the active site of monomer A.

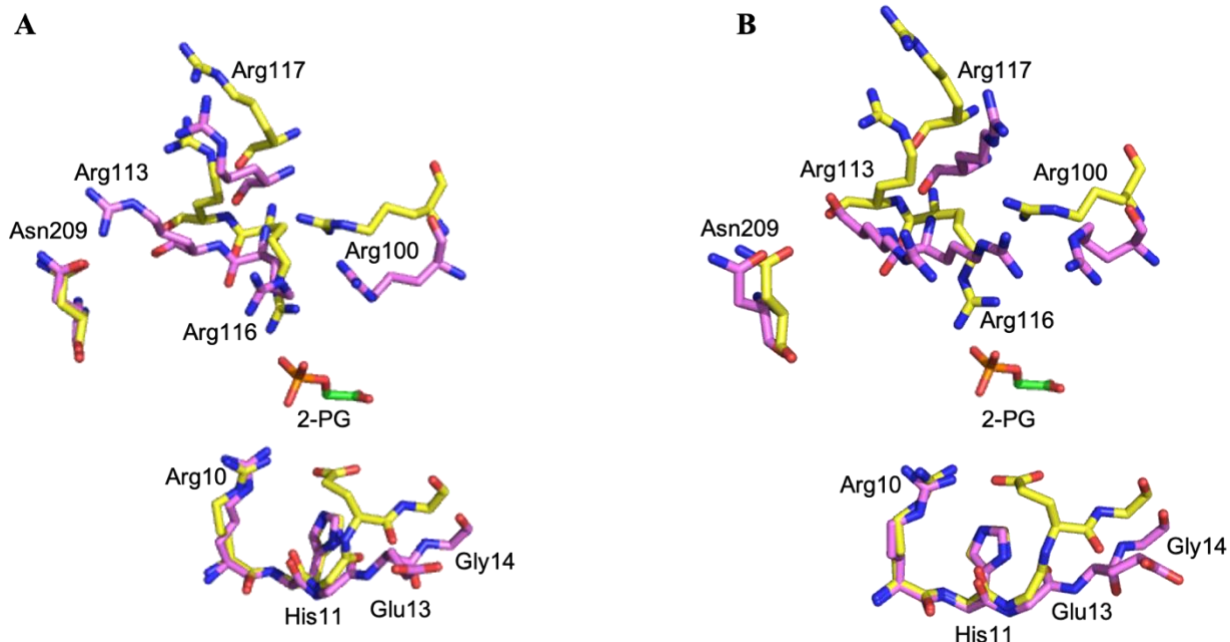


Figure 37. (A) Superposition of the important residues in the active site in monomer B of the ternary BPGM•3-PGA•2-PG complex (violet) and unliganded BPGM (PDB ID 3NFY; yellow). (B) Superposition of the important residues in the active site in monomer B of the binary BPGM•2-PG complex (violet) with the unliganded BPGM structure (yellow).

In summary, the inequivalence in the conformational behavior of the active sites of both monomers suggests the existence of sequential interaction or allostery across the BPGM subunits that is likely induced by the binding of 2-PG at the dimer interface, thereby affecting the binding affinity of a substrate at the second subunit active site. Therefore, we propose that binding of a ligand at the dimer interface will affect the utilization of 3-PGA or 2,3-BPG as a substrate and induce negative cooperativity in which it lowers the binding affinity of the ligand in the active site of the second monomer, making only one site catalytically reactive.

4.2.3. Citrate complex with BPGM

Interestingly, co-crystallization of citrate with BPGM only resulted in citrate binding to monomer A as active site and not that of monomer B. Nonetheless, like the ternary BPGM•2-PGA•2-PG and binary BPGM•2-PG complexes, the binary BPGM•citrate also showed bound citrate at the dimer interface. In this structure, monomer A showed well defined Arg100 and Arg116 density at the entrance of the active site, while the side-chain of Arg117 showed disorder (similar to the unliganded BPGM active site), making monomer A active site appears to be in a partially closed conformation (Figure 38). The active site of monomer B of the binary BPGM•citrate, however, demonstrated significant disorder with Arg100, Arg116 and Arg117 having no electron density. Furthermore, the binary BPGM•citrate complex showed disorder in both monomers, lacking electron density beyond Gly236.

From the forgoing, it appears that the binding affinity of citrate to the active site is weaker than 3-PGA or 2-PG as reflected in the partially closed structure at monomer A, and apparent is missing any bound molecule at monomer B. The binary BPGM•citrate structure with one ligand bound per dimer best fits an extreme form of negative cooperativity named “half of sites reactivity” kinetic model, in which the binding of the ligand to the dimer interface inhibits the binding of the ligand in the active site of the second monomer.²⁰⁴ We assume that the strength of the negative cooperativity depends on the structure and the strength of the interactions of the ligand at the dimer interface. Since the citrate is larger than the 2-PG structure and exhibits more interactions at the dimer interface, the negative cooperativity was observed to be more significant.

In conclusion, it seems that the best working hypothesis at the moment is that binding of ligand at the dimer interface induces a negative cooperativity behavior, decreasing the affinity or

completely inhibiting the binding of ligand at the active site of the second monomer. This is the first such report that displays such an allostereism in BPGM.

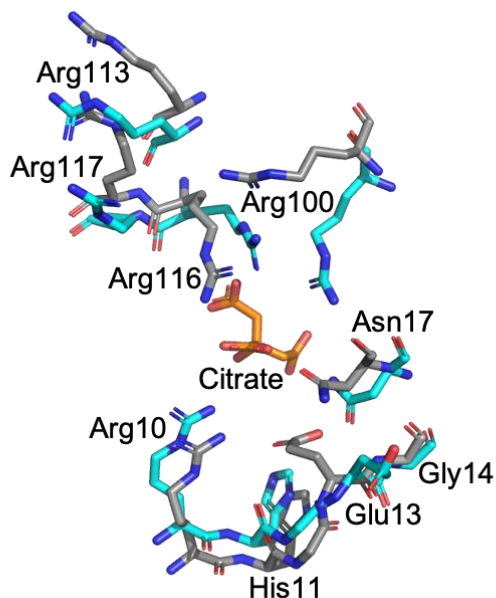


Figure 38. Superposition of the important residues in the active site in monomer B of the binary BPGM•citrate complex (cyan) and the unliganded structure of BPGM (PDB ID 3NFY; gray).

4.2.4. Computational solvent mapping of BPGM using FTMap

The identification of non-catalytic or allosteric binding site at the dimer interface encouraged us to search for other potential allosteric sites on BPGM surface and evaluate the target druggability. Therefore, we carried out computational solvent mapping analysis of the BPGM surface using the FTMap server as described above (4.1.2). Therefore, we will be screening the site against virtual drugs library to find potential allosteric modulators to be used for SCD therapeutics, as described in chapter 5.

CHAPTER 5

5. SPECIFIC AIM 3: Identify BPGM synthase inhibitors and/or phosphatase activators that can be used as leads for SCD drug discovery

Targeting the BPGM enzyme by inhibiting the synthase and/or activating the phosphatase activity to reduce 2,3-Bisphosphoglycerate (2,3-BPG) levels in sickle RBC is an interesting therapeutic approach for sickle cell disease (SCD). Up to date, no drug screening study is reported in the literature to identify small molecules against BPGM for therapeutic purposes. One of the objectives of this chapter is to identify novel lead BPGM modulators that can be developed further in the future as drug candidates for the treatment of SCD. To reach our objective, we have utilized different *in-silico* techniques to search for BPGM modulators against the active site and the non-catalytic binding site at the dimer interface of the protein. The resulted active site hits were obtained and tested for their effect on BPGM phosphatase and synthase activities.

5.1. Specific Aim 3A: Identification of BPGM modulators against the active site

5.1.1. Pharmacophore- based virtual screening and molecular docking

In this study, an *in silico* method that involves a combination of a ligand-based virtual screening and a structure-based molecular docking was implemented to identify putative BPGM modulators targeting the active site. The ligand-based virtual screening exercise is based on the generation of a three-dimensional (3D) pharmacophore model from a reference ligand. The pharmacophore model empirically defines the molecular features of the reference ligand that are critical for its interaction with the enzyme active site. This model was used as a template to search

for compounds that match the selected pharmacophoric features in the virtual chemical database.^{205–207}

X-ray crystal structure of BPGM in complex with 3-PGA was retrieved from the protein data bank (PDB ID 2H4X) and 3D pharmacophore queries were generated from the interaction of 3-PGA with BPGM at the active site using the UNITY database searching program in the molecular modeling software (SYBYL-X 2.0, Tripos Inc.).²⁰⁵ Figure **39** represents the constructed 3D pharmacophore queries from 3-PGA, which include: (1) a negative center placed at the position of the phosphoryl group of 3-PGA, (2) an acceptor atom at the position of the carboxylate group of 3-PGA, and (3) a donor atom at the hydroxyl group of 3-PGA. The negative center searches for a negatively-charged group from the database, such as a carboxylate, sulfate, or phosphate. The acceptor and donor atoms denote sites for an atom that can act as a hydrogen-bond acceptor and hydrogen-bond donor, respectively. A receptor site constraint within 5 Å of the ligand was applied. Consequently, the pharmacophore model was screened using a flexible directed tweak algorithm via a 3D flexible database search (UNITY, Tripos Inc.)²⁰⁵ against diverse set of ligands retrieved from the Molport virtual chemical library, (www.molport.com), which is a public access database that contains over 7 million commercially available compounds, to identify positive hits that match the requirements of the queries.

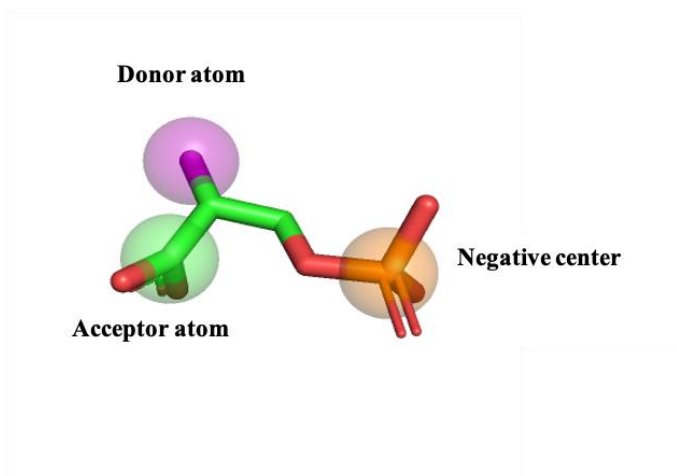


Figure 39. The 3D queries on 3-phosphoglycerate.

The initial UNITY search resulted in 25,000 hits, and the results were viewed using the hitlist manager in SYBYL-X 2.0 software. The hit lists were filtered down to 12,000 by removing duplicates, and linear chain compounds. Also, the hit lists were filtered down by applying the Lipinski's 'Rule of Five' to remove compounds that are unlikely to be good drug candidates. The Lipinski's 'Rule of Five' suggested that five keys physiochemical parameters must exist in drugs to make them orally bioavailable, which include compounds with molecular weight of less than 500 Dalton; the lipophilicity of the compounds as represented by (clogP) have to be less than five; compounds have to contain less than five hydrogen-bond donating groups, and less than 10 hydrogen-bond accepting group.²⁰⁸ All parameters were applied except for the molecular weight, where a 350 Dalton cutoff was used instead. Next, the virtual screening hits, i.e., molecules that met the pharmacophore queries requirements were selected and docked against the BPGM active site using the GOLD 5.4. docking program. Gold is an automated ligand docking software that employs a genetic optimization algorithm to predict different binding poses and conformations of the ligand with the target protein.^{209,210} The program assigns scores of the different binding poses by using a built-in fitness function, which is a metric for measuring the binding of ligand to protein,

and ranks the ligands based on the binding score. The higher the scoring value, the better the docking result. The scoring function used in this exercise was the ChemPLP score, which is the default scoring function in GOLD that takes into account the contribution of hydrogen-bonds, van der Waals, and repulsive interactions between the protein target and heavy atoms of the ligand. Following, the top-ranking list that has the compounds with the highest function score were sorted based on their ligand efficiency (LE) score. The LE was used as an extra metric to estimate the efficiency of the ligand by measuring the average binding affinity per an atom of a ligand to the active site of the target protein. It is mathematically calculated by dividing the free energy of a ligand (ΔG) by the number of non-hydrogen heavy atoms (HA) in the molecule.^{211,212}

$$LE = \Delta G / [\text{number of HA}]$$

Among the top 10 compounds selected, 6 compounds were purchased for experimental activity assay. The chemical structures of the top scoring compounds are shown in Figure 40.

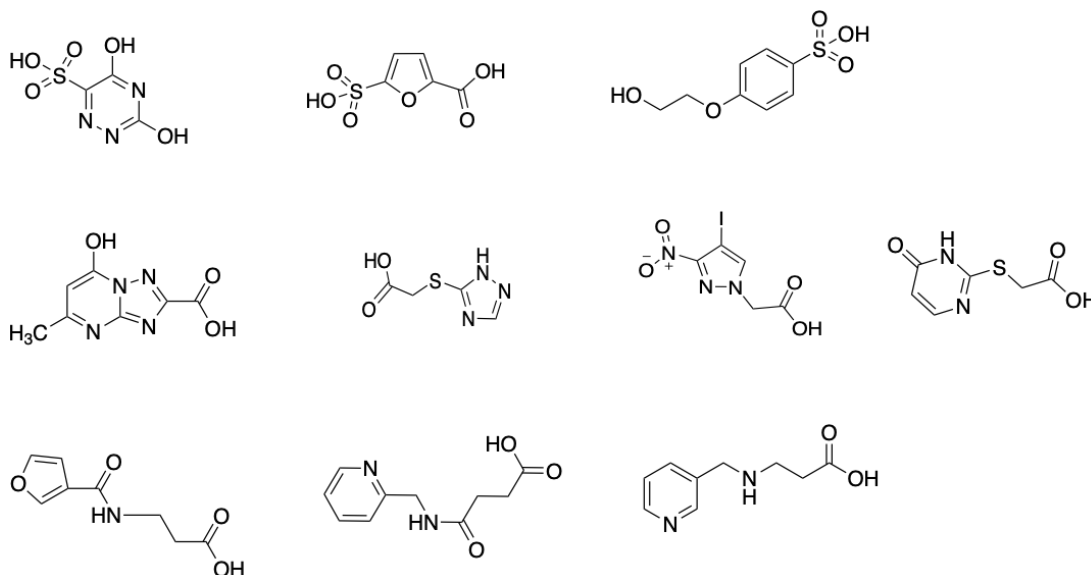


Figure 40. Top hits identified from the virtual screening for the active site.

5.1.2. Machine-learning based virtual screening by *Atomwise*

Atomwise is a pharmaceutical company that uses an AtomNet™ technology for rational drug design.²¹³ AtomNet technology is a convolutional deep learning neural network employed to conduct a machine learning-based virtual screening exercise to find potential lead compounds from a vast database of chemical compounds against any biological target.²¹³ Dr. Safo's research group was granted the opportunity to screen the BPGM target using their artificial intelligence virtual screen as a part of their AIMS program. The AIMS screening yielded 72 small molecules for experimental testing.

5.1.3. PGM1-004A

PGM1-004A (Figure 41), is an anthraquinone derivative compound found by Hitosugi group in an effort to identify anticancer therapies targeting the Warburg effect (aerobic glycolysis), a known cancer hallmark, through inhibiting the phosphoglycerate mutase 1 (PGAM1) activity.²¹⁴ PGAM1 is a glycolytic enzyme that catalyzes the reversible isomerization of 3-PGA into 2-phosphoglycerate (2-PGA) with an intermediate product formation of 2,3-BPG. PGAM1 shares 50% sequence identity and conserved residues at the active site with BPGM.¹⁵⁷ Also, both enzymes catalyze the same three catalytic reactions; the synthase, phosphatase, and mutase activities; but with different rates. PGM1-004A inhibits PGAM1 enzyme with an IC₅₀ of 13 μM.²¹⁴ We hypothesize that the binding of PGM1-004A to BPGM will result in pharmacological inhibition similar to the one obtained from their effect on PGAM1. Therefore, PGM1-004A was purchased from (MedChemExpress LLC) to evaluate its activity against BPGM.

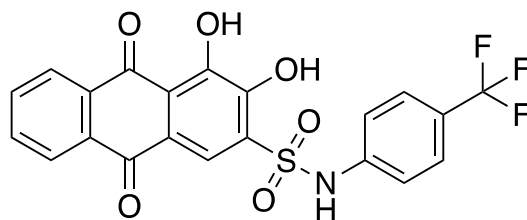


Figure 41. Chemical structure of PGMI-004A.

5.2. Specific Aim 3B: Identification of BPGM allosteric modulators

5.2.1. Molecular docking against BPGM dimer interface

As reported in chapter 4, the X-ray crystallographic studies of BPGM in complex with 2-PG and citrate revealed a novel binding site at the dimer interface. Furthermore, based on the FTMap analysis, the dimer interface was predicted to be a druggable target. On this basis, a molecular docking experiment was carried out by our collaborator, Dr. Abdelsattar Omar, from King Abdulaziz University in Saudi Arabia to identify potential allosteric modifiers targeting the dimer interface. Therefore, a library of approved drugs was docked against the dimer interface site using our determined crystal structure of BPGM in complex with 2-PG. The molecular docking study was performed using the Glide docking software 12.3 (Schrödinger, New York, NY).^{215,216} The docking calculation was performed with Glide in the default standard-precision (SP) mode, using GlideScore for ligand ranking. The top 10 hits (Figure 42) were selected for further analysis using molecular dynamic simulation.

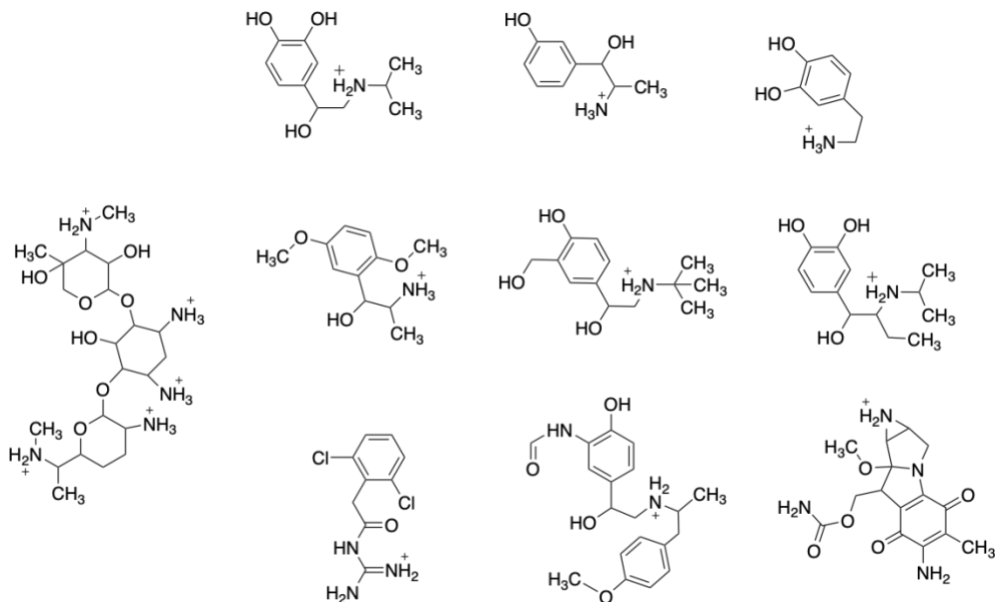


Figure 42. Top hits identified from the molecular docking for the allosteric site.

5.2.2. Molecular dynamic simulation of the top scoring docked compounds with BPGM

The binding of the top scored compounds from the molecular docking exercise were further validated using Desmond Molecular dynamic simulation (Schrödinger, New York, NY)²¹⁷ to confirm their binding stability with BPGM. This work was also done by Dr. Abdelsattar Omar from King Abdulaziz University in Saudi Arabia.

The results of the top-ranking compounds, Methyldopa, Baclofen, Carbamazepine, Mesalazine, Memantine, and Hydrochlorothiazide from the molecular dynamic simulation (Figure 43) showed that the protein-ligand root-mean-squared deviation (RMSD) of each compound is stable throughout the trajectory (50 ns). The results obtained from the simulation suggest the ability of each compound to form a stable complex at the dimer interface site.

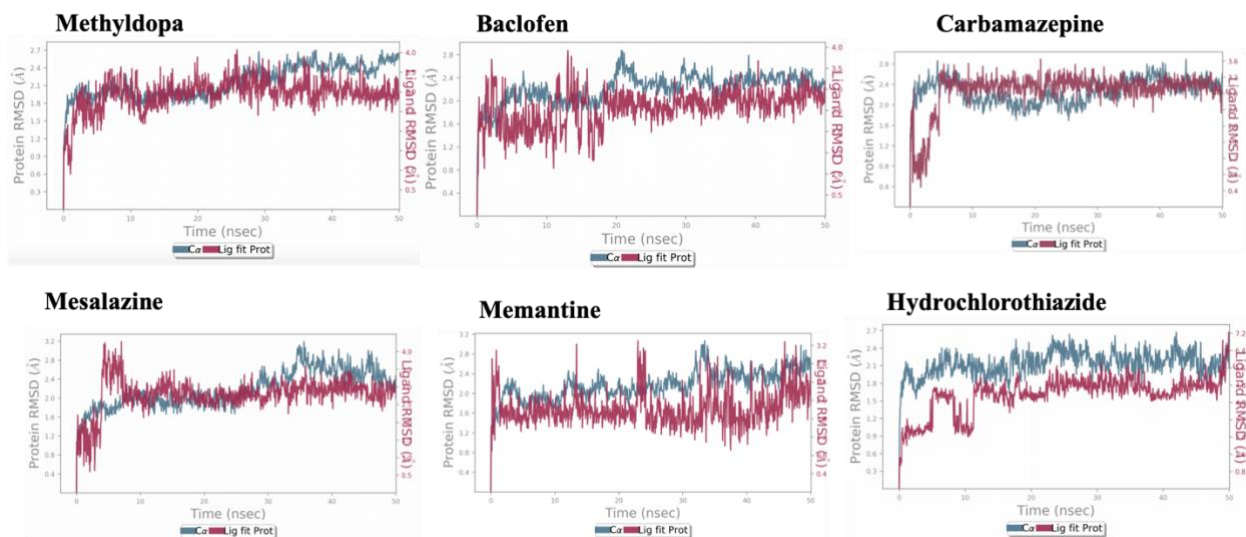


Figure 43. Protein-ligand RMSD graphs for the top-ranking compounds from the molecular dynamic simulation.

5.3. Specific Aim 3C: Examination of the modulators effect of BPGM phosphatase and synthase activities

The compounds obtained from the *in-house* virtual screening and molecular docking exercise, *Atomwise's* molecular screening, and PGMI-004A were tested for their *in vitro* effect on BPGM phosphatase and synthase activities. The compounds were first screened for their effect on the phosphatase activity using the malachite green assay, which is a colorimetric assay for measuring P_i liberated from 2,3-BPG hydrolysis reaction. The cutoff level selected for the screening assay was 50% modulation of the phosphatase activity. The compounds showing $\pm 50\%$ phosphatase inhibition and/or activation were selected for dose-response analysis. Also, selected compounds were tested further for their effect on BPGM phosphatase activity using the

PGK•GAPDH•BPGM phosphatase coupled assay, and for their effect on BPGM synthase activity using GAPDH.BPGM synthase coupled synthase assay.

5.3.1. Compound screening using malachite green assay

A total of 78 compounds, including 6 compounds from the *in-house* virtual screening and molecular docking exercise, and 72 compounds from *Atomwise*'s screening were screened initially for their effect on BPGM phosphatase activity using the malachite green phosphate assay kit (Sigma Aldrich, MAK307-1KT). Malachite green assay is a colorimetric assay used to measure P_i released during 2,3-BPG hydrolysis reaction. The liberated P_i in the reaction mixture form a complex with molybdate in the malachite green reagent turning the color of the reaction mixture to green that is detectable at A_{620} nm using BMG LABTECH CLARIOstar® Plus microplate reader. The assay was carried out with a final assay volume of 100 μ L in a clear flat-bottom 96-well plate. First, a final concentration of 100 μ M compounds in 1% dimethyl sulfoxide (DMSO) (v/v) was added to the empty wells. Then, 100 μ M 2,3-BPG ($\sim K_m$ of 2,3-BPG) in buffer containing 20 mM Tris-HCl and 100 mM NaCl (pH 7.5) was added to each well. The reaction was initiated by the addition of 5 μ M BPGM and allowed to react for 50 min at 37°C. A control (i.e., DMSO), a positive control using 2-phosphoglycolate (2-PG) as an activator and 3-PGA as an inhibitor were included in each experiment. Next, an aliquot from the reaction mixture was diluted 8 times with the assay buffer. The reaction was stopped by the addition of the malachite green dye. Following, the mixture was incubated at room temperature for 30 min for color development, and the absorbance was measured at A_{620} nm. The concentrations of P_i were determined with a P_i standard curve, and the effect of the compounds on the initial velocity of the phosphatase reaction was measured as μ mole of P_i /min. During the study, we observed that a number of the compounds

showed poor solubility and aggregation in the assay mixture. Therefore, the malachite green dye was supplemented with 0.01% Triton X-100 to reduce the aggregation. In addition, the malachite green dye was observed to slowly form precipitations over the 30 min incubation time, which we resolved by diluting the reaction mixture with the buffer before the addition of the reagent for detection.

None of the compounds (Compounds 1, 2, 3, 4, 5, 6) obtained from the *in-house* virtual screening and molecular docking exercise showed any effect on the phosphatase activity (Figure 44). The compounds obtained from *Atomwise's* molecular screen demonstrated modulation of the BPGM phosphatase activity, including activation or inhibition (Figure 45-48). The results showed that compounds B11, E7, F2, and F12 exhibited more than 50% activation, while compounds A10, B6, C7, C8, and D2 showed more than 50% inhibition. Therefore, these compounds were picked for validation using dose-response analysis. Unfortunately, none of the compounds showed dose dependent modulation of the BPGM phosphatase activity. The precipitation of the malachite green dye due to over saturation or the precipitation of the protein in the acidic assay condition may explain the likely false positive hits and/or the inability to observe dose-response effect. The malachite green assay needs to be further optimized to get accurate screening results.

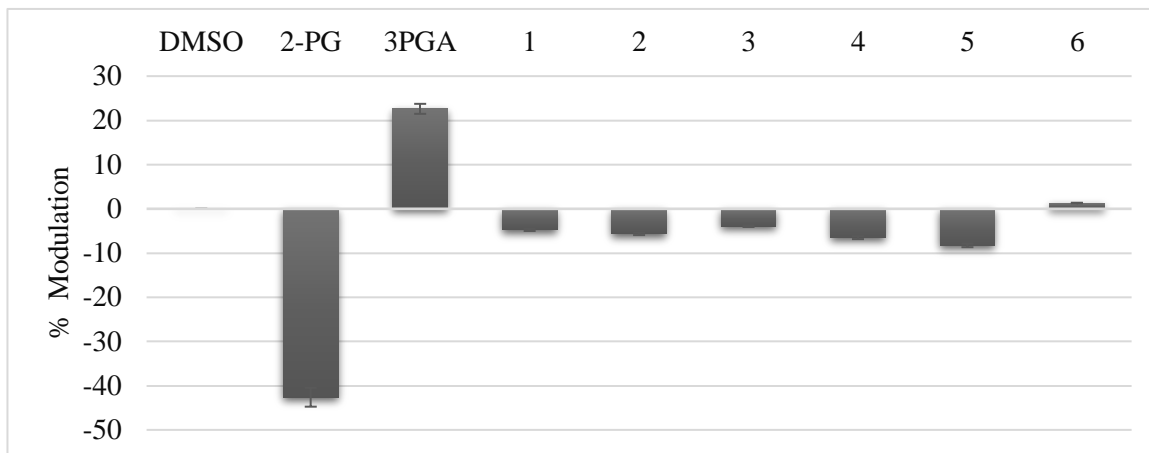


Figure 44. The effect of compounds 1-6, 2-PG, and 3-PGA on BPGM phosphatase activity using malachite green assay.

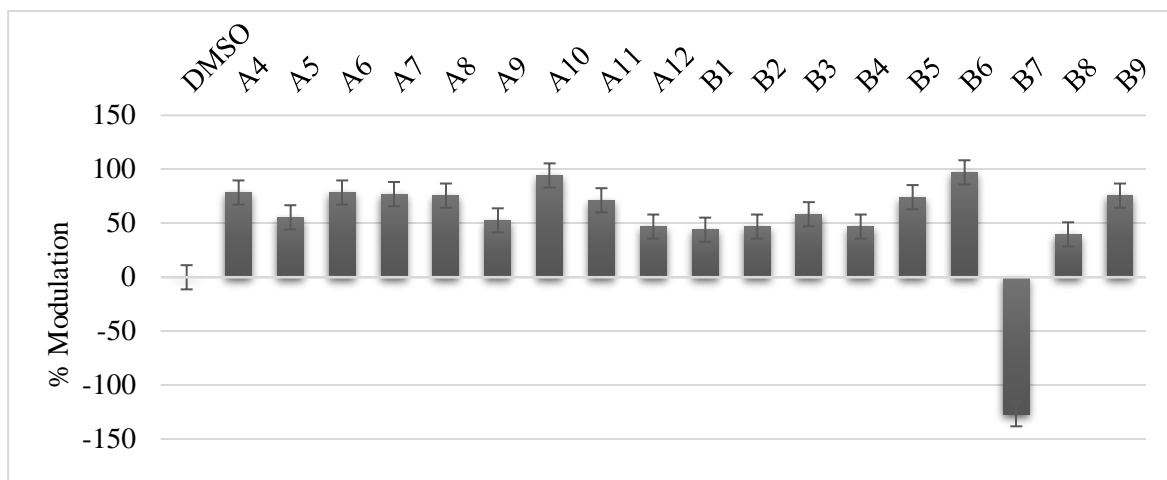


Figure 45. The effect of compounds A4-B9 on BPGM phosphatase activity using malachite green assay.

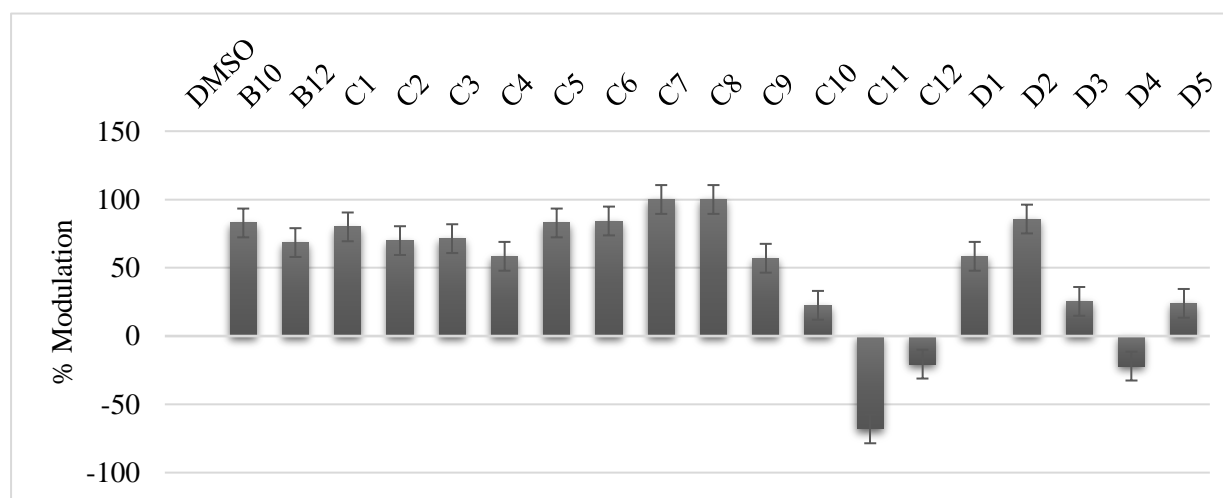


Figure 46. The effect of compounds B10-D5 on BPGM phosphatase activity using malachite green assay.

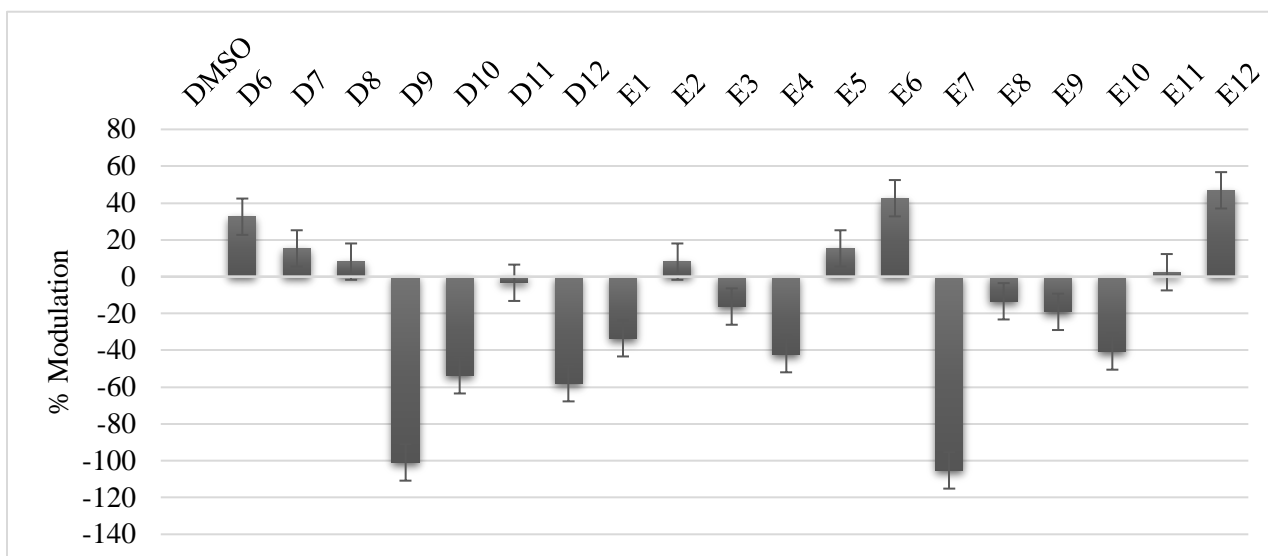


Figure 47. The effect of compounds D6-E12 on BPGM phosphatase activity using malachite green assay.

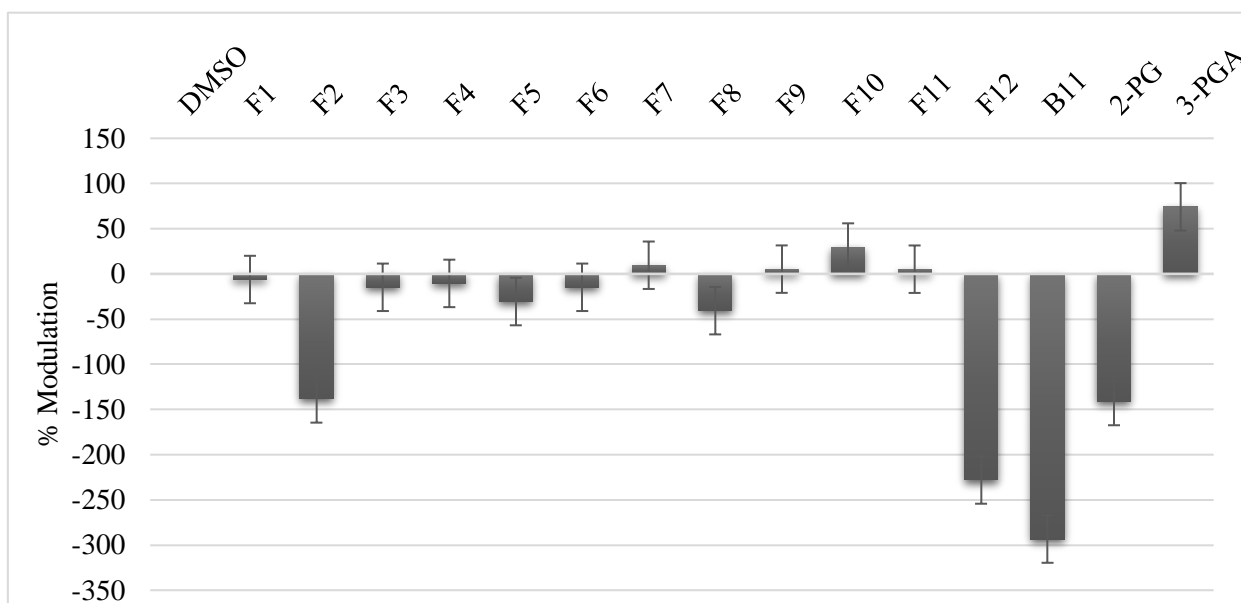


Figure 48. The effect of compounds F1-B11, 2-PG, and 3-PGA on BPGM phosphatase activity using malachite green assay.

5.3.2. Compound screening using PGK•GAPDH•BPGM phosphatase coupled assay

Above, even though we observed significant modulation of BPGM with several compounds from *Atomwise*, none of them showed dose-response effect using the malachite assay. We decided to use an alternate BPGM phosphatase assay, the PGK•GAPDH•BPGM coupled phosphatase assay, to study the dose-response effect of selected *Atomwise*'s compounds, including A5, A10, B6, C7, C8, E7 and F2. The PGK•GAPDH•BPGM phosphatase coupled assay indirectly measures the effect of the compounds on BPGM phosphatase activity by coupling BPGM phosphatase activity with the activity of Phosphoglycerate kinase (PGK) and Glyceraldehyde-3-phosphate dehydrogenase (GAPDH) enzymes. In this assay, BPGM hydrolyzes 2,3-BPG to 3-PGA and Pi. PGK converts 3-PGA to 1,3-BPG, which is a substrate for GAPDH. In the presence of NADH, GAPDH converts 1,3-BPG and NADH to glyceraldehyde-3-phosphate (GAP) and NAD, respectively. The oxidation of NADH to NAD, which correlates with 2,3-BPG hydrolysis activity, is detected spectrophotometrically at A₃₄₀ nm.

The assay was carried out with a final volume of 200 μ L in a clear flat-bottom 96-well plate. The assay reaction contained a final concentration of 100 μ M compound in 1% DMSO (v/v), 50 mM Tris-HCl buffer at (pH 7.5), 10 mM MgCl₂, 0.2 mM NADH, 3 mM ATP, 3.3 U/ml GAPDH, 2.3 U/mL PGK, and 5 μ M BPGM. The reaction was initiated by the addition of 400 μ M 2,3-BPG, and monitored for 20 min at A₃₄₀ nm using a BMG LABTECH CLARIOstar® Plus microplate reader. A DMSO control, a positive control with 2-PG as an activator, and a negative control (lacking 2,3-BPG) were included in each experiment. The compounds showed no effect on the phosphatase activity (Figure 49). The PGMI-004A compound was also tested with the PGK•GAPDH•BPGM phosphatase coupled assay, and the results did not show any significant

modulation of the phosphatase activity. It is clear that the results from the coupled assay are not consistent with the malachite green assay. The inconsistent results are related to the limitations in both assays. The malachite green assay needs to be optimized further to reduce the precipitation that affects the reading output. The PGK•GAPDH•BPGM coupled assay exhibits low sensitivity, requiring high substrate concentration for the activity to be detected.

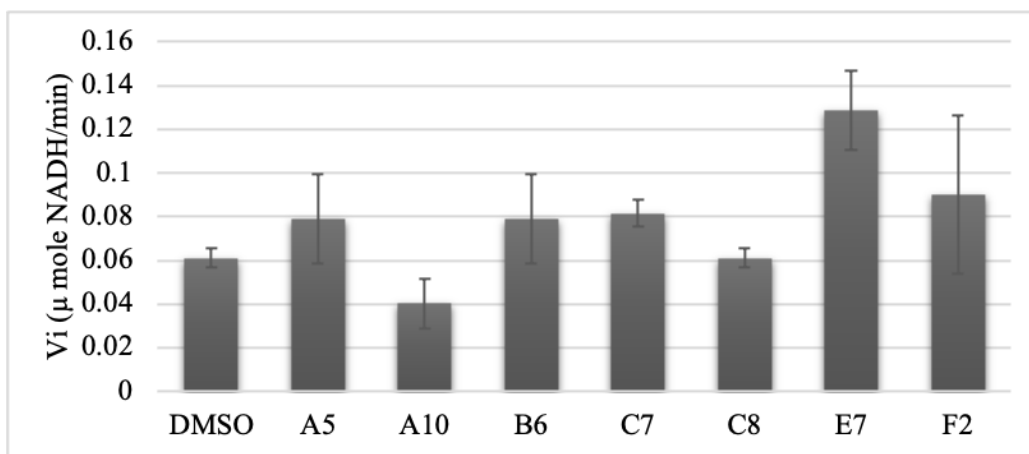


Figure 49. The effect of compounds A5, A10, B6, C7, C8, E7, and F2 on BPGM phosphatase activity using PGK•GAPDH•BPGM phosphatase coupled assay.

5.3.3. Compound screening with GAPDH.BPGM coupled Synthase Assay

The compounds were also tested for their effect on BPGM synthase activity using the GAPDH•BPGM synthase coupled assay, which is a spectrophotometric assay that indirectly measures 2,3-BPG synthesis by coupling BPGM synthase with GAPDH activity. GAPDH is used to convert GAP and NAD into 1,3-BPG and NADH, respectively. The reduction of NAD to NADH, which correlates with 2,3-BPG formation, was monitored at A₃₄₀ nm using BMG LABTECH CLARIOstar® Plus microplate reader.

The compounds obtained from the *in-house* virtual screening and the molecular docking exercise (Compounds 1-6) were tested for their effect on the BPGM synthase activity, and the results did not show any significant effect. In addition, selected *Atomwise* compounds (A5, A10, B6, C7, and C8) were analyzed and the results also showed no effect on the synthase activity (Figure 50). Interestingly, PGM1-004A, the known inhibitor of PGAM1, showed a significant inhibitory effect on the synthase activity in a dose-dependent manner. A dose response experiment using 2-fold serial dilutions of the PGMI-004A (1.5 to 200 μM) showed that PGM1-004A inhibits BPGM synthase activity with an IC₅₀ value (50% inhibitory concentration) of 50±11 μM. This compares with IC₅₀ of 13.1 μM with PGMI-004A inhibition of PGAM1. The data was plotted using nonlinear regression to fit the % inhibition vs. log μM compound concentration (Graphpad Prism software) (Figure 51). The fact that PGMI-004A showed a clear inhibitory data with the synthase activity suggest that the assay works and the other compounds likely do not affect the synthase activity.

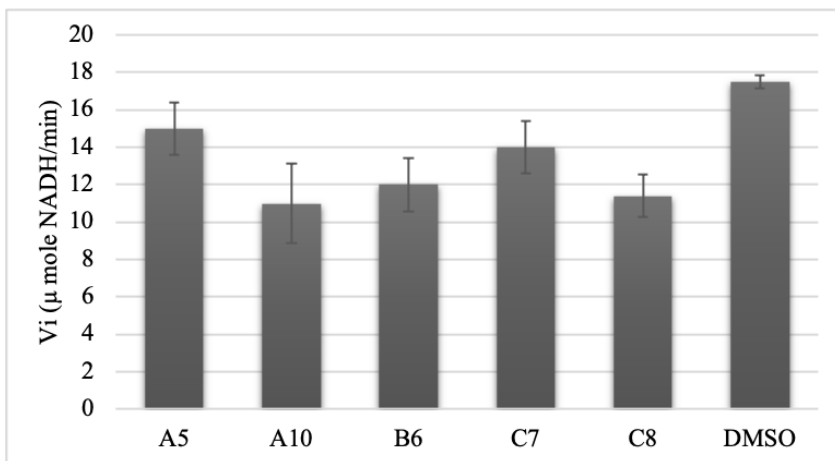


Figure 50. The effect of compounds A5, A10, B6, C7, and C8 on BPGM synthase activity using GAPDH•BPGM synthase coupled assay.

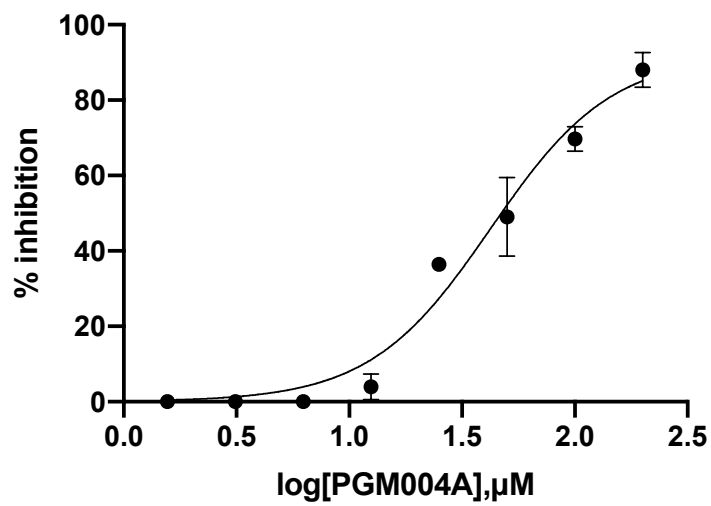


Figure 51. Dose-response curve of PGMI-004A on BPGM synthase activity .

5.4. Specific Aim 3D: Elucidate the X-ray crystallographic binding between BPGM and PGMI-004A.

PGMI-004A was the only compound that appeared to inhibit BPGM synthase activity. Therefore, several attempts were made to co-crystallize PGMI-004A with BPGM to elucidate its atomic interaction with the enzyme. We believe that the binding interactions of PGMI-004A with BPGM would provide useful insight into the design of selective BPGM synthase inhibitors.

Several attempts of co-crystallizing PGMI-004A with BPGM resulted in crystals that either did not diffract or were low-resolution. However, in a last attempt, a cubic crystal form was obtained, and diffraction data collected to 2.3 Å. The structure was determined by Phaser-MR (simple interface) molecular replacement with the Phenix software package¹⁹⁵ using the monomeric unliganded structure of BPGM (PDB ID 3NFY) as a search model. The dimeric structure underwent iterative cycles of refinement with Phenix along with manual refinement and model building using COOT.^{195–197} Crystallographic and refinement parameters are summarized in (Table 8).

The co-crystallized structure of BPGM with PGMI-004A showed no apparent bound ligand in the active site of both monomers nor anywhere in the structure (Figure 52). Both monomers were modelled into density from Ser2 to Leu235. The last 21 residues in the C-terminus were disordered and therefore could not be modelled. The significant disorder in the C-terminus along with the disordered side-chain of Arg117 resulted in both active sites being in open conformation,

similar to the open conformation of the previously reported unliganded BPGM structure (PDB ID 3NFY)

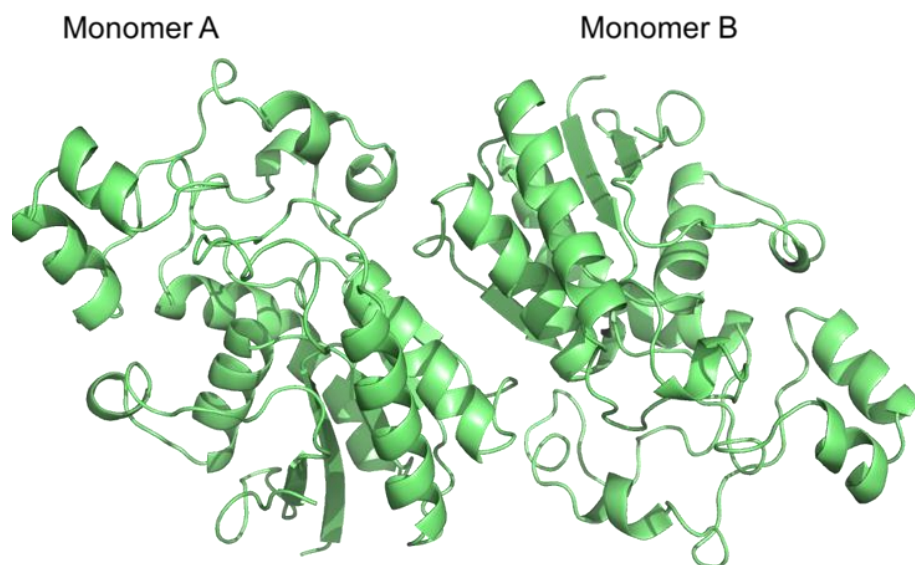


Figure 52. Overall structure of BPGM in complex with PGMI-004.

Table 8. Crystallization and refinement parameters of BPGM•PGMI-004A complex.

Data set	BPGM•PGMI-004A		
Data collection			
Resolution (Å)	2.3 Å		
Space group	P2 ₁ 2 ₁ 2 ₁		
Unit cell dimensions [<i>a</i> , <i>b</i> , <i>c</i> (Å)]	52.13	78.8	120.87
Total no. of reflections	22661		
Completeness	99.32		
Refinement			
R _{work}	0.30		
R _{free} ^{3a}	0.38		
Molprobrity statistics			
All atom clash score	11.63		
Ramachandran plot (%)			
Favored	93.75		
Allowed	5.17		
Outliers	1.08		
Rotamer outlier	0.95		
Wilson B factor	25.97		

^a R_{free} was calculated from 5% randomly selected reflection for cross-validation. All other measured reflections were used during refinement

5.5. Discussion

Targeting the central enzyme of the Rapoport Leubering pathway, BPGM, is suggested as a potential therapeutic opportunity for SCD drug discovery. The fact that BPGM is exclusively expressed in erythrocyte, and is the only enzyme responsible for the synthesis and hydrolysis of 2,3-BPG makes it an attractive target to explore.

We have utilized different techniques to search for BPGM modulators. First, an *in-house* pharmacophore-based virtual screening and molecular docking against BPGM active site were performed, which yielded 6 virtual hits that were purchased for experimental testing. Also, a computational machine learning-based virtual screening against BPGM active site has been performed by the pharmaceutical company, *Atomwise*, as part of their artificial intelligence molecular screen (AIMS) program and resulted in 72 compounds. Lastly, a well validated inhibitor of PGAM1, named PGM1-004A, were purchased for experimental testing.

In addition to targeting BPGM active site, molecular docking was performed against the new non catalytic/allosteric sites at the dimer interface to identify potential allosteric modulators of BPGM activity. This novel binding site was identified during the conduct of this project. Following, the binding of the top scoring docked compounds was confirmed by analyzing their binding stability with BPGM using molecular dynamic simulation. The top 6 compounds from the molecular dynamic simulation, Methyldopa, Baclofen, Carbamazepine, Mesalazine, Hydrochlorothiazide, and Memantine, have been purchased for experimental testing.

Thus, a total of 79 compounds targeting the active site of BPGM were tested for their effect on BPGM phosphatase and synthase activities. Initially, the compounds were screened using the colorimetric malachite green assay. This assay was utilized as direct, robust and alternative assay

to the existing hazardous radioactive assay or the BPGM continuous coupled assay.^{152,154,166,167,170,179}

Screening with the malachite green assay, however, exhibited several challenges as the hits could not be validated with dose-response analysis. The false positive is likely due to malachite green dye precipitation or protein/compounds aggregation at the acidic assay condition during the incubation period (30 min), affecting the stability of the end-point signal.

The compounds were also tested for their effect on the phosphatase activity using the PGK•GAPDH•BPGM phosphatase coupled assay. Likewise, none of the compounds showed any modulation in the phosphatase activity. The PGK•GAPDH•BPGM coupled assay also has several limitations, including less sensitivity when compared to the malachite green assay. For the BPGM phosphatase activity to be detected with this assay, the substrate and the enzyme need to be in high concentration. The substrate (2,3-BPG) concentration is 400 μM , which is four times the K_m value of 2,3-BPG ($\sim 100 \mu\text{M}$), significantly higher than the substrate used in the malachite green assay (100 μM , similar to 2,3-BPG K_m). The high substrate concentration could result in overcoming the modulation exerted by any potential inhibitors and/or activators. It is worth mentioning that this assay has always been used with the activator, 2-PG.

The compounds were also tested for their effect on the BPGM synthase activity using the GAPDH•BPGM synthase coupled assay. Similarly, none of the compounds showed any effect on the synthase activity with the exception of PGMI-004A. PGMI-004A showed inhibition in a dose-dependent manner, with an IC_{50} of $50 \pm 11 \mu\text{M}$. The inability of PGMI-004A compound to show any modulation of the phosphatase activity confirms either the low sensitivity of PGK•GAPDH•BPGM phosphatase coupled assay or that PGMI-004A preferentially modulates the synthase activity. The dissociation equilibrium constant of the enzyme-inhibitor complex (K_i)

could not be obtained due to the inability to vary the 1,3-BPG concentration in the coupled synthase assay as 1,3-BPG is commercially unavailable and has to be enzymatically synthesized in situ during the assay.

The co-crystallization of BPGM with PGMI-004A resulted in a structure with a resolution of 2.3 Å. However, the co-crystal structure did not show bound PGMI-004A at the active site or any other sites. Also, a significant disorder was observed at the C-terminus. Due to the unliganded active site, both active sites expectedly are in open conformations (Figure **53**). The crystallization condition needs to be optimized to obtain BPGM•PGMI-004A complex structure.

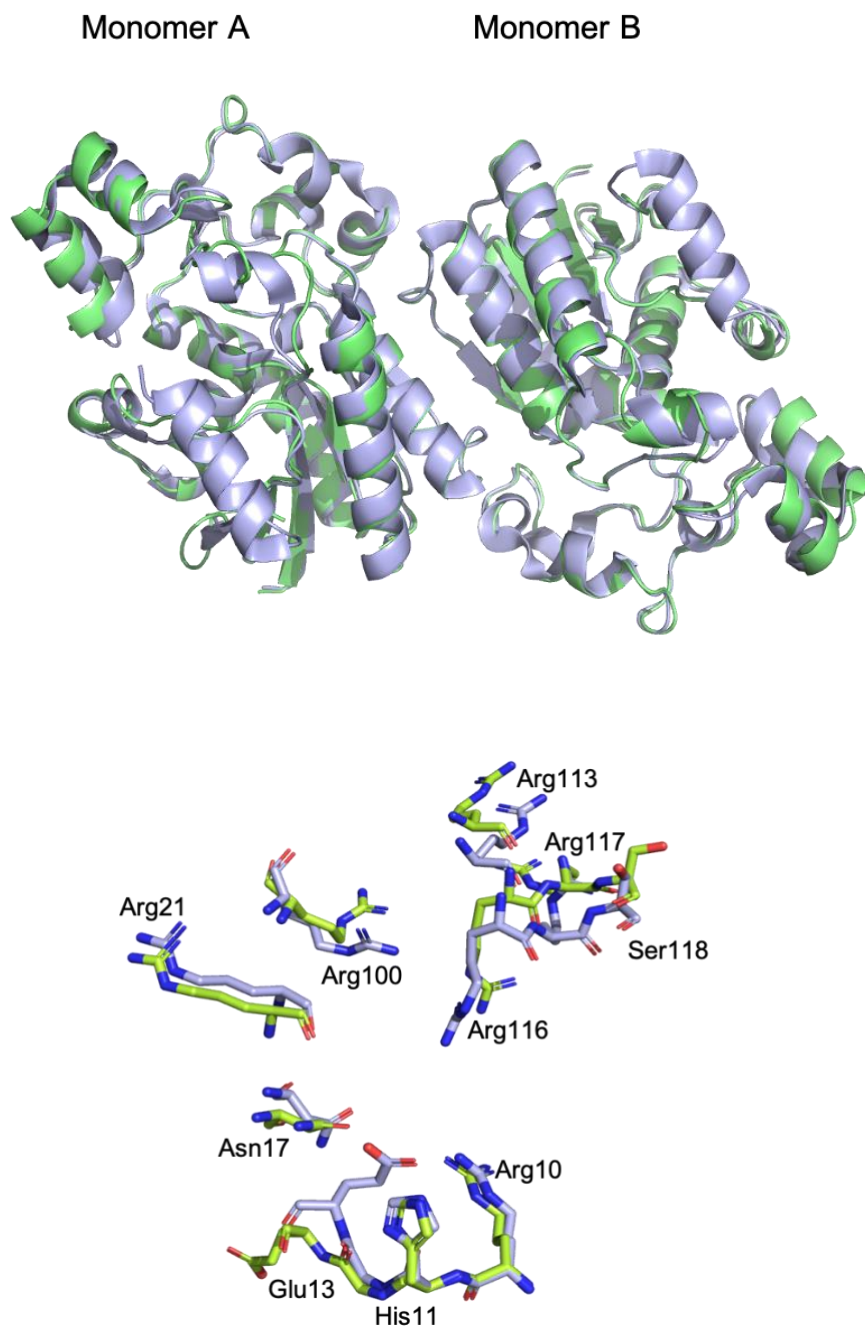


Figure 53. (A) Superposition of the BPGM•PGMI-004A dimer (lime green) with the unliganded BPGM dimer (PDB ID 3NFY, light purple). (B) Superposition of the active site residues of monomer A of BPGM•PGMI-004A and the unliganded BPGM structures.

CHAPTER 6

6. SUMMARY AND CONCLUSION

Bisphosphoglycerate mutase (BPGM) is a multifunctional enzyme in the Rapoport-Luebering pathway, a glycolytic bypass predominantly presents in red blood cells (RBCs), responsible for the synthesis and hydrolysis of 2,3-Bisphosphoglycerate (2,3-BPG).^{5,7-9} The synthesis of 2,3-BPG is the main activity of the enzyme (synthase activity), while the hydrolysis of 2,3-BPG (phosphatase activity) is physiologically low but can be potently activated by 2-phosphoglycolate (2-PG) through a poorly understood mechanism.⁷⁻⁹ 2,3-BPG is crucial for RBCs oxygen delivery by binding directly to hemoglobin (Hb); stabilizing the deoxygenated Hb conformation, and facilitating the release of oxygen to tissues.¹²⁻¹⁴ The level of 2,3-BPG increases as an adaptation mechanism in clinical conditions where the oxygen transport is compromised. In sickle cell disease (SCD), 2,3-BPG level is abnormally elevated due to glycolytic activation in response to hypoxia, which significantly contributes to the disease pathophysiology. The elevated 2,3-BPG directly promotes hypoxia-induced sickle Hb (HbS) polymerization and subsequent RBCs sickling.^{22,150,17}

Modulating BPGM activity through inhibiting the synthase activity or activating the phosphatase activity to reduce 2,3-BPG levels is considered an attractive approach to target HbS polymerization and RBC sickling. The activation of the phosphatase activity by 2-PG has been shown to reduce 2,3-BPG level and consequently reduce HbS polymerization and RBCs sickling.¹⁵⁰

Therefore, the specific aims of this project were to: (1) Elucidate the steady state kinetics of BPGM synthase and phosphatase activities and optimize the activity assays to be used for compounds screening, (2) Elucidate the atomic interactions of BPGM phosphatase with its effectors, and identify allosteric binding site(s) of BPGM, (3) Identify BPGM synthase inhibitor and/or phosphatase activators that can be used as leads for SCD drug discovery.

In this dissertation, we have in chapter 3 studied the steady-state kinetics of BPGM synthase and phosphatase activities in order to optimize and validate appropriate enzymatic assays for compound screening. BPGM synthase activity was studied using GAPDH•BPGM synthase coupled assay. Due to the complexity and the limitations of this assay, it was not possible to obtain detailed steady-state kinetic parameters of BPGM synthase activity. However, the assay was used for compound screening in a low-throughput setting. BPGM phosphatase activity, on the other hand, was studied using the colorimetric malachite green assay, and PGK•GAPDH•BPGM phosphatase coupled assay. The steady-state kinetic parameters of the phosphatase activity were characterized with both assays and the conditions of the assays were optimized for the compounds screening experiments. The malachite green assay was utilized as a robust assay that can be easily adapted to high-throughput setting.

Next, we shed the light on 2-PG activation mechanism of BPGM phosphatase activity by studying the kinetic of 2-PG activation using PGK•GAPDH•BPGM phosphatase coupled assay, and structurally elucidated the binding mode of BPGM with 2-PG using X-ray crystallography in chapter 4. The kinetic analysis showed 2-PG activation mechanism to be mixed of noncompetitive and competitive mechanism suggesting the binding of 2-PG to the active site as well as a non-catalytic or allosteric site. The structural analysis of BPGM in complex with 2-PG, in presence and

absence of 2,3-BPG, confirmed the kinetic finding as it revealed for the first time a novel non-catalytic or allosteric binding site for 2-PG at the dimer interface in addition to its predicted or known active site binding. Moreover, we have elucidated the binding mode of citrate, a known BPGM phosphatase inhibitor, to gain further understanding of the phosphatase molecular mechanism. The co-crystal structure of BPGM in complex with citrate showed citrate bound to one active site per dimer as well as at the dimer interface. On this basis, we proposed the existence of negative cooperativity induced by 2-PG or citrate binding at the dimer interface.

Furthermore, in chapter 4, we have also carried out a computational solvent mapping technique using FTMap online server in an attempt to identify additional BPGM binding sites, including allosteric site, and predict their druggability. The results demonstrated the dimer interface site as the most important and likely druggable site of BPGM, supporting our crystallographic findings of the dimer interface as a potential druggable target.

In chapter 5, multiple *in-silico* approaches aimed to identify BPGM modulators against the active site were conducted to find potential modulators for BPGM activity. The results from the compounds screening did not show any potential BPGM modulatory effect except for PGMI-004A that inhibited BPGM synthase activity (IC_{50} of $50 \pm 11 \mu M$). PGMI-004A is an already well validated inhibitor for the homologous enzyme PGAM1.²¹⁴ Based on the inhibitory effect of PGMI-004A, the anthraquinone chemical scaffold can be used to develop specific inhibitors for BPGM synthase activity. The crystal structure of BPGM in complex with PGMI-004A did not show any ligand bound to BPGM, and further optimization of the crystallization condition is required to obtain the bound BPGM•PGMI-004A complex.

Apart from targeting the active site of BPGM, the novel dimer interface was also docked against a library of approved drugs, and the top scoring compounds were analyzed for their binding stability with BPGM. Six of the top ranked compounds were obtained for experimental testing.

The identification of the allosteric site at the dimer interface opens new promising avenue in the development of allosteric modulators for BPGM given the challenges in targeting BPGM active site, owing to its highly charged environment. In addition, the saturation of the intracellular substrate may overcome the effects of any potential competitive modulators.

In conclusion, this dissertation provides novel insights into the mechanism of 2-PG activation and citrate inhibition of BPGM phosphatase activity. In addition, it explored a novel therapeutic approach to SCD by targeting the reduction of 2,3-BPG concentration that can mitigate hypoxia-induced HbS polymerization and RBC sickling.

The limitation of this project is the challenges experienced with the available BPGM activity biochemical assays that limited their use for high-throughput screening. Therefore, developing direct and sensitive assays is needed to allow for discovery of potential BPGM modulators.

Future research should also consider experimental and computational efforts to expand our understanding of BPGM as a molecular target and its catalytic mechanisms. For instance, understanding the role of the C-terminus in the transition of active to inactive conformation and the relationship between the binding at the dimer interface and BPGM dimerization by using molecular dynamic simulation techniques or site directed mutagenesis at the dimer interface site.

CHAPTER 7

7. EXPERIMENTAL SECTION

General information: Unless stated otherwise, all reagents used in the biochemical assays were purchased from Sigma-Aldrich (St. Louis, MO) and Thermo Fisher Scientific (Waltham, MA).

7.1. BPGM expression and purification:

Human BPGM clone in pET-30b (+) vector was purchased from (GenScript USA Inc.) and transformed into *E.coli* BL21-CodonPlus (DE3)-RIPL cells for expression. The transformed cells were streaked in a kanamycin plate and incubated overnight at 37° C. A single colony was picked from the kanamycin plate and grown overnight with shaking at 37° C in Luria-Bertani (LB) broth containing 100 µg/mL kanamycin. The culture was then inoculated (1:20) into 6 L of LB media and grown at 37° C under aerobic conditions until the optical density at 600 nm (OD600) reached 0.6. Next, the cell culture was induced with 0.2 mM isopropyl-thio-β-D-galactosidase (IPTG) and further incubated at lower temperature of 30° C for 8 h. Cells were harvested by centrifugation and cell pellets were resuspended in a buffer containing 50 mM Tris-HCl, 10 mM imidazole and 300 mM NaCl at pH 8 (Buffer A). The resuspended cells were lysed using Avestin Emulsiflex (Emulsiflex C-3, operating at > 20,000 PSI), followed by high-speed centrifugation at 12,000 rpm for 20 min. The supernatant was filtered and loaded onto a 5-ml HisTrap HP column (GE Healthcare Bio-Sciences) pre-equilibrated with buffer A. The purification process was carried out using ÄKTA fast protein liquid chromatography (FPLC).

First, the column was washed with buffer A that contain low concentration of imidazole (10 mM) to reduce the non-specific binding proteins. Then, the imidazole gradient was gradually increased using a buffer containing 50 mM Tris-HCl, 250 mM imidazole and 300 mM NaCl at pH 8 (buffer B) to remove the non-specific binding proteins until the protein was eluted with 75 mM imidazole concentration. Protein fractions were collected and the purity was assessed by single band on sodium dodecyl sulfate polyacrylamide gel electrophoresis (SDS-PAGE) (Figure 54). The pure fractions were then pooled and dialyzed overnight at 4 °C using buffer containing 20 mM Tris-HCl and 150 mM NaCl at pH 7.5. The dialysis buffer was then exchanged to a second dialysis buffer containing lower salt concentration of 20 mM Tris HCL and 100 mM NaCl (pH 7.5) for 4 h. The protein concentration was determined spectrophotometrically using BPGM extinction coefficient $A_{280} \text{ 1.63 AU} = 1 \text{ mg/mL}$.

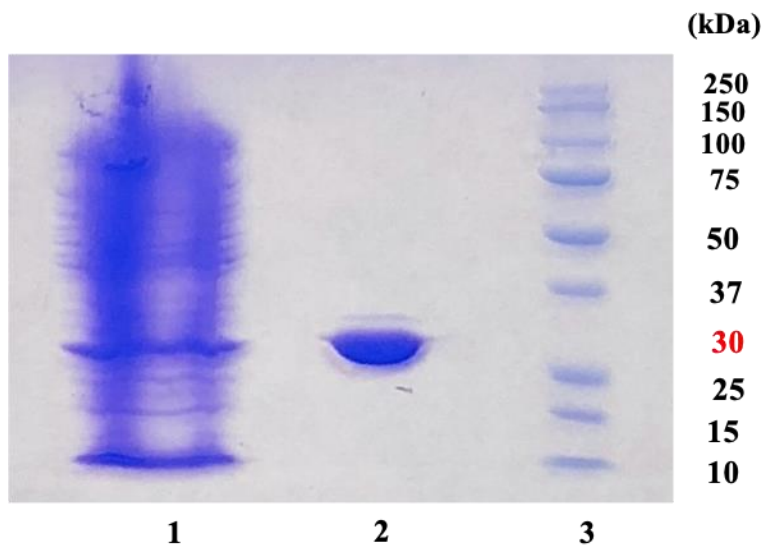


Figure 54. SDS-PAGE analysis of BPGM expressed in E.coli **(1)** E.coli crude extract **(2)** Purified BPGM fractions **(3)** Molecular weight standards.

7.2. BPGM synthase activity:

BPGM synthase activity was measured using a continuous spectrophotometric coupled enzymatic assay developed by Garel et al.¹⁷⁹ with some modifications, using an Agilent 8453 UV-VIS spectrophotometer. The assay was performed in a total volume of 1 mL mixture containing 50 mM Tris HCl, 7 mM monobasic potassium phosphate (KH₂PO₄) at pH 8, 2U/mL Glyceraldehyde-3-phosphate dehydrogenase (GAPDH), 1 mM Nicotine diamine dinucleotide (NAD), 2.9 mM Glyceraldehyde-3-phosphate (GAP), and 40 μM 3-phosphoglycerate (3-PGA) in the presence and absence of 1mM 2-phosphoglycolate (2-PG). The reaction was initiated by the addition of various concentrations of BPGM (0.1-2.5 μM), and monitored by the increase in A₃₄₀ nm that corresponds to the reduction of NAD for 10 min. The activity was obtained by calculating the initial velocity (ΔA_{340} nm/min) from the slope of the tangent line in the reaction progress curve. Then, the absorbance was converted into μmole of NADH/min using the millimolar extinction coefficient of NADH ($\epsilon = 6.2/\text{mM}\cdot\text{cm}$). The activity curve of the initial velocity (μmole of NADH/min) vs. BPGM concentration (μM) was plotted using Microsoft Excel.

For the compound screening experiment, the assay volume was scaled down to 200 μL and the assay carried out using BMG LABTECH CLARIOstar[®] Plus microplate reader. In a 96-well clear flat-bottomed plate, a final compound concentration of 100 μM dissolved in 1% DMSO (v/v) was incubated with the reaction mixture containing 50 mM Tris-HCl, 7 mM KH₂PO₄ at pH 8, 2 U/mL GAPDH, 1 mM NAD, 3 mM GAP, and 40 μM 3-PGA. The reaction was initiated by the addition of 0.2 μM BPGM and monitored for 10 min. A control (with DMSO) and a positive control (with 1 mM 2-PG) were tested in each experiment. The initial velocity was calculated as a μmole of NADH/min using the millimolar extinction coefficient for NADH of 6.22. The effect of

the compounds on the initial velocity of BPGM synthase was plotted as a bar graph of μmole of NADH/min vs. compound name using Microsoft Excel.

For PGMI-004A dose-response assay, two-fold serial dilutions of PGMI-004A dissolved in 1% DMSO (v/v) (1.5 to 200 μM) were tested in the assay mixture containing 50 mM Tris-HCl, 7 mM KH_2PO_4 at pH 8, 2 U/mL GAPDH, 1 mM NAD, 2.9 mM GAP, and 40 μM 3-PGA. The reaction was initiated by the addition of 0.2 μM BPGM. The initial velocity was calculated from each concentration and the data was converted to % inhibition compared to control (with DMSO). The dose response curve of % inhibition vs. PGMI-004A $\log[\mu\text{M}]$ was generated using variable slope (four parameters) log (inhibitor) vs. response function in Prism GraphPad software.

7.3. BPGM phosphatase activity:

7.3.1. Malachite green assay

The assay was carried out with the commercially available malachite green assay kit (Sigma Aldrich; MAK307), which measures the liberated inorganic phosphate (P_i) from 2,3-BPG hydrolysis at absorbance of $A_{620\text{ nm}}$ using BMG LABTECH CLARIOstar[®] Plus microplate reader.

For time-dependent experiment, the assay was conducted in 96-well clear flat-bottomed plate with a total volume of 100 μl . The standard assay condition contains 100 μM 2,3-BPG in a buffer composed of 20 mM Tris-HCl and 100 mM NaCl at pH 7.5 in the absence and presence of 5 μM 2-PG. The reaction was initiated by the addition of 5 μM BPGM. Aliquot of 10 μL of the reaction mixture was withdrawn every 10 min and diluted with 70 μL assay buffer. Then, the reaction mixture was stopped by the addition of 20 μL malachite green dye. The mixture was left

at room temperature for 30 min for color development. Next, the released P_i was measured at A_{620} nm and P_i concentration was determined using P_i standard curve. The data from each time point were measured as $\mu\text{mole of } P_i/\text{min}$ and plotted against time in min using Microsoft Excel.

For the un-stimulated and 2-PG stimulated phosphatase activity experiments, the standard assay condition contains various concentrations of BPGM (0.3-10 μM) in a buffer composed of 20 mM Tris-HCl and 100 mM NaCl at pH 7.5 in the absence and presence of 5 μM 2-PG. The reaction was initiated by addition of 100 μM 2,3-BPG, followed by incubation at 37°C for 50 min for the non-stimulated reaction and 20 min for the 2-PG stimulated phosphatase reaction. Next, an aliquot of 10 μL of the reaction mixture was diluted with 70 μL assay buffer and the reaction were then stopped by the addition of 20 μL malachite green reagent. The mixture was left at room temperature for 30 min for color development. Next, the activity of the enzyme was measured as $\mu\text{mole of } P_i/\text{min}$ and the data was plotted as $\mu\text{mole of } P_i/\text{min}$ vs. BPGM concentration (μM) using Microsoft Excel.

For steady-state kinetic characterization, the assay mixture contains various concentrations of 2,3-BPG (3-500 μM) in a buffer composed of 20 mM Tris-HCl and 100 mM NaCl at pH 7.5 in the absence and presence of 5 μM 2-PG. The reaction was started by the addition of 5 μM BPGM to the unstimulated reaction mixture and 2 μM BPGM to the 2-PG stimulated reaction mixture. Data from each substrate concentration was fitted to Michaelis–Menten nonlinear regression model using GraphPad Prism 8 software to obtain K_m , V_{max} and k_{cat} values.

For compound screening assay, a final concentration of 100 μM compounds dissolved in 1% DMSO (v/v) were added to the empty wells in clear flat-bottomed 96 well-plates. Next, assay mixture containing 20 mM Tris-HCl, 100 mM NaCl at pH 7.5, and 100 μM 2,3-BPG was added

to each well. Next, the reaction was initiated by the addition of 2 μM BPGM to each well. The mixture was incubated for 50 min, and 10 μL aliquot was withdrawn and diluted 8 times with the assay buffer. Following, the reaction was stopped by the addition of 20 μL malachite green dye (with 0.01% Triton X-100) to reduce compounds and/or protein aggregation. A control (with DMSO), positive control with the activator, 2-PG, and the inhibitor, 3-PGA, were included in each experiment. The effect of the compounds on BPGM phosphatase activity was represented in bar graph as initial velocity ($\mu\text{mole of P}_i/\text{min}$) vs. compound name using Microsoft Excel.

7.3.2. PGK. GAPDH.BPGM coupled phosphatase assay

The assay was performed using the method described by Calvin *et al.*¹⁷⁰ The reaction was carried out in a final volume of 200 μL in clear flat-bottomed 96 well-plates using BMG LABTECH CLARIOstar[®] Plus microplate reader.

For the phosphatase activity experiment, the standard assay mixture included 50 mM Tris-HCl buffer at pH 7.5, 10 mM MgCl_2 , 0.2 mM NADH, 3 mM ATP, 3.3 U/mL GAPDH, 2.3 U/mL PGK, and various concentrations of BPGM (1-10 μM) in the presence and absence of 10 μM 2-PG. The reaction was initiated by the addition of 0.8 mM 2,3-BPG and was monitored for 20 min by observing the decrease in $A_{340\text{ nm}}$ that correlate to the oxidation of NADH. The initial velocity ($\Delta A_{340\text{ nm}}/\text{min}$) was calculated from the slope of tangent line in the reaction progress curve. The absorbance was then converted into $\mu\text{mole of NADH}/\text{min}$ using the millimolar extinction coefficient for NADH of 6.22. The activity curve was obtained by plotting the initial velocity ($\mu\text{mole of NADH}/\text{min}$) vs. BPGM concentration (μM) using Microsoft Excel.

For steady state kinetic experiment, the standard assay mixture included 50 mM Tris-HCl buffer at pH 7.5, 10 mM MgCl_2 , 0.2 mM NADH, 3 mM ATP, 3.3 U/mL GAPDH, 2.3 U/mL PGK,

and various concentrations of 2,3-BPG (8-1000 μM) in final volume of 200 μL . The reaction was started by the addition of 5 μM BPGM in the non-stimulated reaction or addition of 2 μM BPGM in the presence of 10 μM 2-PG. Data from each substrate concentration was fitted to Michaelis–Menten nonlinear regression model using GraphPad Prism 8 software to obtain K_m , V_{\max} and k_{cat} values.

For studying the activation mechanism of 2-PG, the standard assay mixture included 50 mM Tris-HCl buffer at pH 7.5, 10 mM MgCl_2 , 0.2 mM NADH, 3 mM ATP, 3.3 U/mL GAPDH, 2.3 U/mL PGK, various concentrations of 2,3-BPG (3-2000 μM), and 5 different fixed 2-PG concentrations (10, 50, 250, 500, and 1000 μM). The reaction was initiated by the addition of 2 μM BPGM and monitored for 20 min. The initial velocity at each 2,3-BPG concentration in fixed 2-PG concentration was plotted against 2,3-BPG concentration using the Michaelis-Menten nonlinear regression model using the GraphPad Prism 8 software. The reciprocal of the activity at each 2,3-BPG in fixed 2-PG concentration and the reciprocal of 2,3-BPG concentration was plotted to generate the Lineweaver-Burk using Microsoft Excel to obtain K_m , V_{\max} and k_{cat} values.

For compound screening, a final concentration of 100 μM compounds dissolved in 1% DMSO (v/v) were incubated with the reaction mixture containing 50 mM Tris-HCl buffer at pH 7.5, 10 mM MgCl_2 , 0.2 mM NADH, 3 mM ATP, 3.3 U/mL GAPDH, 2.3 U/mL PGK, and 5 μM BPGM. The reaction was started by the addition of 400 μM 2,3-BPG to each well. The reaction was monitored for 20 min and the activity was calculated as μmole of NADH/min. The effect of the compound on BPGM phosphatase activity was represented in a bar graph as initial velocity (μmole of NADH/min) vs. compound name using Microsoft Excel.

7.4. X-ray crystallographic studies

7.4.1. Crystallization of the ternary BPGM•3-PGA•2-PG complex structure

Purified BPGM (30 mg/mL) in 20 mM Tris-HCl and 100 mM NaCl at pH 7.5 was incubated with 3.8 mM 2,3-BPG and 7.6 mM 2-PG at room temperature for 1 h to form a complex prior to crystallization experiment. Crystallization was carried out with a hanging drop vapor diffusion method accomplished using the Art Robbins Instruments (ARI) Crystal Gryphon Robot. The complex mixture was screened against PEGRx HT crystallization screen (Hampton Research) that contained different precipitants. Single crystal suitable for X-ray analysis was obtained with 10% v/v Polyethylene glycol 200, 0.1 M BIS TRIS propane at pH 9, and 18% Polyethylene glycol 8000. The crystal was mounted and flash-frozen in liquid nitrogen before data collection. The crystallization condition required no cryoprotectant. The X-ray diffraction data was collected at 100 K using Rigaku MicroMax-007HF X-ray Generator and Eiger R 4 M Detector. The data set was processed with CrysAllysPro 40.64.42a (Rigaku OD, Yarnton, Oxfordshire, England, 2015) and the CCP4 suite of programs.¹⁹⁴ The crystal structure was determined with Phaser-MR (simple interface) molecular replacement with the Phenix software package¹⁹⁵ using the monomeric structure of BPGM complexed with 2,3-BPG (PDB ID 2H4Z) as a search model. The solved structure was refined with the Phenix software along with model building using the COOT graphic program.^{195–197}

7.4.2. Crystallization of the binary BPGM•2-PG complex structure

Purified BPGM (30 mg/mL) in 20 mM Tris-HCl and 100 mM NaCl at pH 7.5 was incubated with 8.3 mM 2-PG. The mixture was crystallized with a hanging drop diffusion method accomplished manually using the same crystallization condition as described above: 10% v/v Polyethylene glycol 200, 0.1 M BIS TRIS propane at pH 9, and 18% polyethylene glycol 8000

(Hampton research). The crystallization condition required no cryoprotectant. The X-ray diffraction data was collected at 100 K using a Rigaku MicroMax-007HF X-ray Generator and Eiger R 4 M Detector. The data set was processed with the CrysAlysPro 40.64.42a (Rigaku OD, Yarnton, Oxfordshire, England, 2015) and the CCP4 suite of programs.¹⁹⁴ The refined ternary BPGM•3-PGA•2-PG complex without bound ligands and water molecules was used as the starting model to refine against the binary BPGM•2-PG complex diffraction data. The solved structure was refined with the Phenix software along with model building using the COOT graphic program.^{195–}

197

7.4.3. Crystallization of binary BPGM•Citrate complex structure

Purified BPGM (30 mg/mL) in 20 mM Tris-HCl and 100 mM NaCl at pH 7.5 was crystallized with a hanging drop vapor diffusion method using the Art Robbins Instruments (ARI) Crystal Gryphon Robot. A single crystal was obtained using the Wizard Classic 1 crystal screen containing 1000 mM Sodium citrate tribasic, 100 mM Sodium cacodylate/hydrochloric acid at pH 6.5 (Rigaku). The crystal was first cryo-protected by soaking into cryo-solution containing mother liquor and 20% glycerol. The crystal flash-frozen in liquid nitrogen before data collection. The X-ray diffraction data was collected at 100 K using a Rigaku MicroMax-007HF X-ray Generator and Eiger R 4 M Detector. The data set was processed with CrysAlysPro 40.64.42a (Rigaku OD, Yarnton, Oxfordshire, England, 2015) and the CCP4 suite of programs.¹⁹⁹ The structure was determined using the Phaser-MR (simple interface) molecular replacement with the Phenix software package¹⁹⁵ using the monomeric structure of BPGM in complex with 2,3-BPG (PDB ID 2H4Z) as a search model. The solved structure was refined with the Phenix software along with model building using the COOT graphic program.^{195–197}

7.4.4. Crystallization of BPGM in complex with PGMI-004A

BPGM sample (30 mg/mL) in 20 mM Tris-HCl and 100 mM NaCl at pH 7.5 was incubated with PGMI-004A in 1:5 molar ratio with a total volume of 580 μ L. The BPGM-PGMI-004A complex mixture was incubated overnight at 4 °C to ensure complete binding. Next, the complex mixture was concentrated with Amicon ultra centrifugal filter to 80 μ L with a final concentration of 22 mg/mL. Crystallization was performed with a hanging drop vapor diffusion method accomplished using the Art Robbins Instruments (ARI) Crystal Gryphon Robot, and the mixture was screened against Wizard Classic 2 crystal screen (Rigaku). A single crystal suitable for X-ray analysis was obtained with the crystallization condition of 10% (w/v) PEG 3K, 200 mM MgCl₂, and 100 mM sodium cacodylate/HCl at pH 6.5. The co-crystal was cryo-protected with a solution containing the mother liquor and 20% glycerol, and then quickly flash frozen with liquid nitrogen before data collection. The X-ray diffraction data were collected at 100 K using a Rigaku MicroMax-007HF X-ray Generator and Eiger R 4 M Detector. The data set was processed with CrysAlisPro 40.64.42a (Rigaku OD, Yarnton, Oxfordshire, England, 2015) and the CCP4 suite of programs.¹⁹⁴ The structure was determined using the Phaser-MR (simple interface) molecular replacement with the Phenix software package¹⁹⁵ using the monomeric structure of the unliganded BPGM (PDB ID 3NFY) as a search model. The solved structure was refined with the Phenix software along with model building using the COOT graphic program.^{195–197}

7.5. FTMap server

The unliganded BPGM crystal structure (PDB ID 3NFY) was uploaded into FTMap online server (<http://ftmap.bu.edu>).^{198,199} FTMap scans the surface of the protein for identification of allosteric binding sites using a fast Fourier transform (FTT) algorithm. The output from the FTMAP server is a PDB file containing the analyzed protein structure with clusters of small molecular probes forming the consensus sites (CSs) that can be visualized using the graphic program PyMOL.

7.6. Molecular modeling

7.6.1. Pharmacophore based virtual screening

The 3D pharmacophore generation was carried out using the SYBYL-X software package (Tripos Inc., St. Louis, MO, USA).²⁰⁵ The crystal structure of BPGM in complex with 3-PGA (PDBID 2H4X) was retrieved from the protein data bank (<https://www.rcsb.org/>). The target file was prepared by adding hydrogen atoms and energy minimized using the Tripos force field function in SYBYL-X. Also, Gasteiger-Hückel charges were assigned, and a gradient of 0.005 kcal/mol was set with maximum iterations of 100,000. All other parameters were kept as default.

Key molecular interactions of 3-PGA at the active site were identified and used to build the UNITY queries. In addition, a volume constraint that takes into account the size of the binding site was applied. Next, the generated 3D pharmacophore queries were screened against the retrieved Molport database using 3D flexible database search by UNITY.

7.6.2. GOLD docking

The crystal structure of BPGM in complex with 3-PGA (PDBID 2H4X) was prepared by adding hydrogen, deleting water and extracting the ligand. Then, the hits were docked into the defined active site of BPGM using the automatic docking program GOLD. The default ChemPLP scoring function was assigned. During the docking run, the docking speed was set to slow which equate to 100,000 operations, and the run was specified for 100 solutions of each ligand using default parameters.

7.6.3. Glide docking

The binary BPGM•2-PG complex crystal structure was selected for docking a library of approved drugs against the dimer interface site. The docking study was performed using Glide program Maestro 12.3 (Schrödinger, LLC).^{215,216} First, the ligands were optimized using ligand Preparation function implemented in Maestro. Then, the target protein was prepared using the protein preparation wizard in Maestro. The water molecules were removed, the hydrogen atoms were added, and the binding pocket was identified by placing a grid box around 2-PG binding site at the dimer interface. The molecular docking calculations were performed using the Glide standard precision function.

7.6.4. Molecular dynamic simulation

The molecular dynamic (MD) simulations were performed using Desmond simulation (Schrödinger, LLC).²¹⁷ All systems were set up using “System Builder” in Maestro. The Isothermal-Isobaric (NPT) ensemble with the temperature 300 K and a pressure 1 bar was applied in all simulation runs. The simulation duration was 50 ns. To analyze the MD simulation data, the Simulation Interaction Diagram tool implemented in Maestro was used to obtain Protein-Ligand RMSD

REFERENCES

- (1) Grace, R. F.; Glader, B. Red Blood Cell Enzyme Disorders. *Pediatr. Clin. North Am.* **2018**, *65* (3), 579–595.
- (2) Van Wijk, R.; Van Solinge, W. W. The Energy-Less Red Blood Cell Is Lost: Erythrocyte Enzyme Abnormalities. *Blood* **2005**, *106* (13), 4034–4042.
- (3) Huisjes, R.; Bogdanova, A.; van Solinge, W. W.; Schiffelers, R. M.; Kaestner, L.; van Wijk, R. Squeezing for Life - Properties of Red Blood Cell Deformability. *Frontiers in Physiology*. Frontiers Media S.A. June 1, 2018, p 656.
- (4) Engelking, L. R. Carbohydrate Metabolism in Erythrocytes. In *Textbook of Veterinary Physiological Chemistry*; Elsevier, 2015; pp 190–194.
- (5) Rapoport, S.; Luebering, J. Glycerate-2,3-Diphosphatase. *J. Biochem.* **1951**, *189* (2), 683–694.
- (6) Rapoport, S.; Luebering, J. The Formation of 2,3-Diphosphoglycerate in Rabbit Erythrocyte: The Existence of a Diphosphoglycerate Mutase. *J. Biol. Chem.* **1950**, *183*, 507–516.
- (7) Rose, Z. B.; Whalex, R. G. The Phosphorylation of Diphosphoglycerate Mutase*. *J. Biol. Chem.* **1973**, *248* (5), 1513–1519.
- (8) Rose, Z. B.; Dube, S. Rates of Phosphorylation and Dephosphorylation of Phosphoglycerate Mutase and Bisphosphoglycerate Synthase. *J. Biol. Chem.* **1976**, *251* (26), 4817–4822.
- (9) Ikura, K.; Sasaki, R.; Narita, H.; Sucimoto, E.; Chiba, H. Multifunctional Enzyme, Bisphosphoglyceromutase/ 2,3-Bisphosphoglycerate Phosphatase/Phosphoglyceromutase, from Human Erythrocytes Evidence for a Common Active Site. *Eur. J. Biochem* **1976**, *66* (3), 515–522.

- (10) Isidor Greenwald. A New Type of Phosphoric Acid Compound Isolated from Blood, with Some Remarks on the Effect of Substitution on the Rotation of I-Glyceric Acid. *J. Biol. Chem.* **1925**, 63 (2), 339–349.
- (11) Sutherland, E. W.; Posternak, T. Z.; Cori, C. F. The Mechanism of Action of Phosphoglucomutase and Phosphoglyceric Acid Mutase. *J. Biol. Chem.* **1949**, 179 (1), 501.
- (12) Benesch, R. E. R.; Benesch, R. E. R. The Mechanism of Interaction of Red Cell Organic Phosphates with Hemoglobin. *Adv. Protein Chem.* **1974**, 28 (C), 211–237.
- (13) Benesch, R.; Benesch, R. E. The Effect of Organic Phosphates From the Human Erythrocyte on the Allosteric Properties of Hemoglobin. *Biochem. Biophys. Res. Commun.* **1967**, 26 (2), 162–167.
- (14) Chanutin, A.; Curnish, R. R. Effect of Organic and Inorganic Phosphates on the Oxygen Equilibrium of Human Erythrocytes. *Arch. Biochem. Biophys.* **1967**, 121 (1), 96–102.
- (15) Oski, F. A.; Gottlieb, A. J.; Miller, W. W.; Delivoria-Papadopoulos, M. The Effects of Deoxygenation of Adult and Fetal Hemoglobin on the Synthesis of Red Cell 2,3-Diphosphoglycerate and Its in Vivo Consequences. *J. Clin. Invest.* **1970**, 49 (2), 400–407.
- (16) Ahmed, M. H.; Ghatge, M. S.; Safo, M. K. Hemoglobin: Structure, Function and Allostery. In *Subcellular Biochemistry*; Springer, 2020; Vol. 94, pp 345–382.
- (17) Safo, M. K.; Ahmed, M. H.; Ghatge, M. S.; Boyiri, T. Hemoglobin-Ligand Binding: Understanding Hb Function and Allostery on Atomic Level. *Biochimica et Biophysica Acta - Proteins and Proteomics*. Elsevier June 1, 2011, pp 797–809.
- (18) Benesch, R.; Benesch, R. E. Intracellular Organic Phosphates as Regulators of Oxygen Release by Haemoglobin. *Nature* **1969**, 221 (5181), 618–622.
- (19) Bunn, H. F.; Jandl, J. H. Control of Hemoglobin Function within the Red Cell. *N. Engl. J.*

- Med.* **1970**, 282 (25), 1414–1421.
- (20) Bunn, H. F. Evolution of Mammalian Hemoglobin Function . *Blood* **1981**, 58 (2), 189–197.
- (21) Safo, M. K.; Kato, G. J. Therapeutic Strategies to Alter the Oxygen Affinity of Sickle Hemoglobin. *Hematol. Oncol. Clin. North Am.* **2014**, 28 (2), 217–231.
- (22) Poillon, W. N.; Kim, B. C.; Welty, E. V; Walder, J. A. The Effect of 2,3-Diphosphoglycerate on the Solubility of Deoxyhemoglobin S. *Arch. Biochem. Biophys.* **1986**, 249 (2), 301–305.
- (23) Sun, K.; D'alessandro, A.; Ahmed, M. H.; Zhang, Y.; Song, A.; Ko, T.-P.; Nemkov, T.; Reisz, J. A.; Wu, H.; Adebisi, M.; et al. Structural and Functional Insight of Sphingosine 1-Phosphate-Mediated Pathogenic Metabolic Reprogramming in Sickle Cell Disease. *Sci. Rep.* **2017**, 7 (15281).
- (24) Sun, K.; Zhang, Y.; D'Alessandro, A.; Nemkov, T.; Song, A.; Wu, H.; Liu, H.; Adebisi, M.; Huang, A.; Wen, Y. E.; et al. Sphingosine-1-Phosphate Promotes Erythrocyte Glycolysis and Oxygen Release for Adaptation to High-Altitude Hypoxia. *Nat. Commun.* **2016**, 7 (12086).
- (25) Adebisi, M. G.; Manalo, J. M.; Xia, Y. Metabolomic and Molecular Insights into Sickle Cell Disease and Innovative Therapies. *Blood Advances*. American Society of Hematology April 23, 2019, pp 1347–1355.
- (26) Bunn, H. F. Pathogenesis and Treatment of Sickle Cell Disease. *N. Engl. J. Med.* **1997**, 337 (11), 762–769.
- (27) Steinberg, M. H. Sickle Cell Anemia, the First Molecular Disease: Overview of Molecular Etiology, Pathophysiology, and Therapeutic Approaches. **2008**, 8, 1295–1324.
- (28) Harrington, D. J.; Adachi, K.; Royer, W. E. The High Resolution Crystal Structure of

- Deoxyhemoglobin S. *J. Mol. Biol.* **1997**, 272 (3), 398–407.
- (29) Ghatge, M. S.; Ahmed, M. H.; Omar, A. S. M.; Pagare, P. P.; Rosef, S.; Kellogg, G. E.; Abdulmalik, O.; Safo, M. K. Crystal Structure of Carbonmonoxy Sickle Hemoglobin in R-State Conformation. *J. Struct. Biol.* **2016**, 194 (3), 446–450.
- (30) Bunn, H. F.; Forget, B. G. *Hemoglobin: Molecular, Genetic and Clinical Aspects*; W.B. Saunders Company, Philadelphia, 1986.
- (31) Eaton, W. A.; Hofrichter, J. Sickle Cell Hemoglobin Polymerization. *Adv. Protein Chem.* **1990**, 40, 63–279.
- (32) Edelstein, S. J. Molecular Topology in Crystals and Fibers of Hemoglobin S. *J. Mol. Biol.* **1981**, 150 (4), 557–575.
- (33) Cretegnny, I.; Edelstein, S. J. Double Strand Packing in Hemoglobin S Fibers. *J. Mol. Biol.* **1993**, 230 (3), 733–738.
- (34) Nagel, R. L.; Johnson, J.; Bookchin, R. M.; Garel, M. C.; Rosa, J.; Schiliro, G.; Wajcman, H.; Labie, D.; Moo-Penn, W.; Castro, O. β -Chain Contact Sites in the Haemoglobin S Polymer. *Nature* **1980**, 283 (5750), 832–834.
- (35) Benesch, R. E.; Kwong, S.; Benesch, R. The Effects of α Chain Mutations Cis and Trans to the B6 Mutation on the Polymerization of Sickle Cell Haemoglobin. *Nature* **1982**, 299 (5880), 231–234.
- (36) Rhoda, M. D.; Martin, J.; Blouquit, Y.; Garel, M. C.; Edelstein, S. J.; Rosa, J. Sickle Cell Hemoglobin Fiber Formation Strongly Inhibited by the Stanleyville II Mutation (Alpha 78 Asn Leads to Lys). *Biochem. Biophys. Res. Commun.* **1983**, 111 (1), 8–13.
- (37) Shah, F.; Dwivedi, M. Pathophysiology and Recent Therapeutic Insights of Sickle Cell Disease. *Ann. Hematol.* **2020**, 99 (5), 925–935.

- (38) Hofrichter, J.; Ross, P. D.; Eaton, W. A. Kinetics and Mechanism of Deoxyhemoglobin S Gelation: A New Approach to Understanding Sickle Cell Disease. *Proc. Natl. Acad. Sci. U. S. A.* **1974**, *71* (12), 4864–4868.
- (39) Piel, F. B.; Steinberg, M. H.; Rees, D. C. Sickle Cell Disease. *New England Journal of Medicine*. Massachusetts Medical Society April 20, 2017, pp 1561–1573.
- (40) Hebbel, R. P.; Osarogiagbon, R.; Kaul, D. The Endothelial Biology of Sickle Cell Disease: Inflammation and a Chronic Vasculopathy. *Microcirculation*. March 2004, pp 129–151.
- (41) Pawloski, J. R.; Hess, D. T.; Stamler, J. S. Impaired Vasodilation by Red Blood Cells in Sickle Cell Disease. *Proc. Natl. Acad. Sci. U. S. A.* **2005**, *102* (7), 2531–2536.
- (42) De Franceschi, L. Pathophysiology of Sickle Cell Disease and New Drugs for Treatment. *Mediterr. J. Hematol. Infect. Dis.* **2009**, *1*, e2009024.
- (43) Akinsheye, I.; Klings, E. S. Sickle Cell Anemia and Vascular Dysfunction: The Nitric Oxide Connection. *J. Cell. Physiol.* **2010**, *224* (3), 620–625.
- (44) Hassell, K. L. Population Estimates of Sickle Cell Disease in the U.S. *American Journal of Preventive Medicine*. April 2010, pp S512-21.
- (45) Piel, F. B.; Hay, S. I.; Gupta, S.; Weatherall, D. J.; Williams, T. N. Global Burden of Sickle Cell Anaemia in Children under Five, 2010-2050: Modelling Based on Demographics, Excess Mortality, and Interventions. *PLoS Med.* **2013**, *10* (7), e1001484.
- (46) Hulihan, M.; Hassell, K. L.; Raphael, J. L.; Smith-Whitley, K.; Thorpe, P. CDC Grand Rounds: Improving the Lives of Persons with Sickle Cell Disease. *MMWR. Morb. Mortal. Wkly. Rep.* **2017**, *66* (46), 1269–1271.
- (47) Lubeck, D.; Agodoa, I.; Bhakta, N.; Danese, M.; Pappu, K.; Howard, R.; Gleeson, M.; Halperin, M.; Lanzkron, S. Estimated Life Expectancy and Income of Patients With Sickle

- Cell Disease Compared With Those Without Sickle Cell Disease. *JAMA Netw. open* **2019**, 2 (11), e1915374.
- (48) Platt, O. S. Hydroxyurea for the Treatment of Sickle Cell Anemia. *N. Engl. J. Med.* **2008**, 358, 1362–1369.
- (49) FDA New Release. FDA approves new treatment for sickle cell disease | FDA <https://www.fda.gov/news-events/press-announcements/fda-approves-new-treatment-sickle-cell-disease> (accessed May 29, 2019).
- (50) Blair, H. A. Crizanlizumab: First Approval. *Drugs* **2020**, 80 (1), 79–84.
- (51) Metcalf, B.; Chuang, C.; Dufu, K.; Patel, M. P.; Silva-Garcia, A.; Johnson, C.; Lu, Q.; Partridge, J. R.; Patskovska, L.; Patskovsky, Y.; et al. Discovery of GBT440, an Orally Bioavailable R-State Stabilizer of Sickle Cell Hemoglobin. *ACS Med. Chem. Lett.* **2017**, 8 (3), 321–326.
- (52) Pule, G. D.; Mowla, S.; Novitzky, N.; Wiysonge, C. S.; Wonkam, A. A Systematic Review of Known Mechanisms of Hydroxyurea-Induced Fetal Hemoglobin for Treatment of Sickle Cell Disease. *Expert Review of Hematology*. Taylor and Francis Ltd September 3, 2015, pp 669–679.
- (53) Bauer, D. E.; Kamran, S. C.; Orkin, S. H. Reawakening Fetal Hemoglobin: Prospects for New Therapies for the β -Globin Disorders. *Blood*. American Society of Hematology October 11, 2012, pp 2945–2953.
- (54) Cokic, V. P.; Smith, R. D.; Beleslin-Cokic, B. B.; Njoroge, J. M.; Miller, J. L.; Gladwin, M. T.; Schechter, A. N. Hydroxyurea Induces Fetal Hemoglobin by the Nitric Oxide-Dependent Activation of Soluble Guanylyl Cyclase. *J. Clin. Invest.* **2003**, 111 (2), 231–239.

- (55) Nahavandi, M.; Tavakkoli, F.; Wyche, M. Q.; Perlin, E.; Winter, W. P.; Castro, O. Nitric Oxide and Cyclic GMP Levels in Sickle Cell Patients Receiving Hydroxyurea. *Br. J. Haematol.* **2002**, *119* (3), 855–857.
- (56) Hillery, C. A.; Du, M. C.; Wang, W. C.; Scott, J. P. Hydroxyurea Therapy Decreases the in Vitro Adhesion of Sickle Erythrocytes to Thrombospondin and Laminin. *Br. J. Haematol.* **2000**, *109* (2), 322–327.
- (57) Sinha, C. B.; Bakshi, N.; Ross, D.; Krishnamurti, L. From Trust to Skepticism: An in-Depth Analysis across Age Groups of Adults with Sickle Cell Disease on Their Perspectives Regarding Hydroxyurea. *PLoS One* **2018**, *13* (6), e0199375.
- (58) Niihara, Y.; Zerez, C. R.; Akiyama, D. S.; Tanaka, K. R. Oral L-Glutamine Therapy for Sickle Cell Anemia: I. Subjective Clinical Improvement and Favorable Change in Red Cell NAD Redox Potential. *Am. J. Hematol.* **1998**, *58* (2), 117–121.
- (59) Quinn, C. T. L-Glutamine for Sickle Cell Anemia: More Questions than Answers. *Blood* **2018**, *132* (7), 689–693.
- (60) Niihara, Y.; Matsui, N. M.; Shen, Y. M.; Akiyama, D. A.; Johnson, C. S.; Sunga, M. A.; Magpayo, J.; Embury, S. H.; Kalra, V. K.; Cho, S. H.; et al. L-Glutamine Therapy Reduces Endothelial Adhesion of Sickle Red Blood Cells to Human Umbilical Vein Endothelial Cells. *BMC Blood Disord.* **2005**, *5* (4).
- (61) Minniti, C. P. L -Glutamine and the Dawn of Combination Therapy for Sickle Cell Disease. *N. Engl. J. Med.* **2018**, *379* (3), 292–294.
- (62) Niihara, Y.; Razon, R.; Majumdar, S.; Claggett, B.; Onyekwere, O. C.; Ikeda, A.; Singleton, T.; Wood, A. K.; Singh, R.; Tran, L.; et al. Phase 3 Study of L-Glutamine in Sickle Cell Disease: Analyses of Time to First and Second Crisis and Average Cumulative Recurrent

- Events. *Blood* **2017**, *130* (1), 685.
- (63) Niihara, Y.; Miller, S. T.; Kanter, J.; Lanzkron, S.; Smith, W. R.; Hsu, L. L.; Gordeuk, V. R.; Viswanathan, K.; Sarnaik, S.; Osunkwo, I.; et al. A Phase 3 Trial of L-Glutamine in Sickle Cell Disease. *N. Engl. J. Med.* **2018**, *379* (3), 226–235.
- (64) Ortiz de Montellano, P. R. A New Step in the Treatment of Sickle Cell Disease. *Biochemistry* **2018**, *57* (5), 470–471.
- (65) L-Glutamine (Endari) for Sickle Cell Disease. *Med. Lett. Drugs Ther.* **2018**, *60* (1539), 21–22.
- (66) Kaufman, M. B. L-Glutamine Oral Powder (Endari). *Pharm. Ther.* **2017**, *42* (10), 620.
- (67) Kutlar, A.; Embury, S. H. Cellular Adhesion and the Endothelium: P-Selectin. *Hematol. Oncol. Clin. North Am.* **2014**, *28* (2), 323–339.
- (68) Matsui, N. M.; Borsig, L.; Rosen, S. D.; Yaghmai, M.; Varki, A.; Embury, S. H. P-Selectin Mediates the Adhesion of Sickle Erythrocytes to the Endothelium. *Blood* **2001**, *98* (6), 1955–1962.
- (69) Ataga, K. I.; Kutlar, A.; Kanter, J.; Liles, D.; Cancado, R.; Friedrich, J.; Guthrie, T. H.; Knight-Madden, J.; Alvarez, O. A.; Gordeuk, V. R.; et al. Crizanlizumab for the Prevention of Pain Crises in Sickle Cell Disease. *N. Engl. J. Med.* **2017**, *376* (5), 429–439.
- (70) Kutlar, A.; Kanter, J.; Liles, D. K.; Alvarez, O. A.; Cançado, R. D.; Friedrich, J. R.; Knight-Madden, J. M.; Bruederle, A.; Shi, M.; Zhu, Z.; et al. Effect of Crizanlizumab on Pain Crises in Subgroups of Patients with Sickle Cell Disease: A SUSTAIN Study Analysis. *Am. J. Hematol.* **2019**, *94* (1), 55–61.
- (71) Hutchaleelaha, A.; Patel, M.; Silva, A.; Oksenberg, D.; Metcalf, B. GBT440 Demonstrates High Specificity for Red Blood Cells in Nonclinical Species. *Blood* **2015**, *126* (23), 2172.

- (72) Hoppe, C. C.; Inati, A. C.; Brown, C.; Wang, W.; Gordeuk, V. R.; Liem, R.; Woods, G.; Piccone, C. M.; Fong, E.; Balaratnam, G.; et al. Initial Results from a Cohort in a Phase 2a Study (GBT440-007) Evaluating Adolescents with Sickle Cell Disease Treated with Multiple Doses of GBT440, a HbS Polymerization Inhibitor. *Blood* **2017**, *130* (Suppl 1).
- (73) Vichinsky, E.; Hoppe, C. C.; Ataga, K. I.; Ware, R. E.; Nduba, V.; El-Beshlawy, A.; Hassab, H.; Achebe, M. M.; Alkindi, S.; Brown, R. C.; et al. A Phase 3 Randomized Trial of Voxelotor in Sickle Cell Disease. *N. Engl. J. Med.* **2019**, *381*, 509–519.
- (74) Blair, H. A. Voxelotor: First Approval. *Drugs* **2020**, *80* (2), 209–215.
- (75) Patel, M.; Cabrales, P.; Dufu, K.; Metcalf, B.; Sinha, U. GTx011, an Anti-Sickling Compound, Improves SS Blood Rheology By Reduction of HbS Polymerization Via Allosteric Modulation of O₂ Affinity. *Blood* **2014**, *124* (21), 1370.
- (76) Oksenberg, D.; Dufu, K.; Patel, M. P.; Chuang, C.; Li, Z.; Xu, Q.; Silva-Garcia, A.; Zhou, C.; Hutchaleelaha, A.; Patskovska, L.; et al. GBT440 Increases Haemoglobin Oxygen Affinity, Reduces Sickling and Prolongs RBC Half-Life in a Murine Model of Sickle Cell Disease. *Br. J. Haematol.* **2016**, *175* (1), 141–153.
- (77) Lehrer-Graiwer, J.; Howard, J.; Hemmaway, C. J.; Awogbade, M.; Telfer, P.; Layton, M.; Mant, T.; Dufu, K.; Hutchaleelaha, A.; Koller, T.; et al. GBT440, a Potent Anti-Sickling Hemoglobin Modifier Reduces Hemolysis, Improves Anemia and Nearly Eliminates Sickle Cells in Peripheral Blood of Patients with Sickle Cell Disease. *Blood* **2015**, *126* (23), 542.
- (78) Dufu, K.; Oksenberg, D.; Zhou, C.; Hutchaleelaha, A.; Archer, D. GTx011, a Potent Allosteric Modifier of Hemoglobin Oxygen Affinity, Prevents RBC Sickling in Whole Blood and Prolongs RBC Half-Life in Vivo in a Murine Model of Sickle Cell Disease. *Blood* **2014**, *124* (21), 217.

- (79) Sankaran, V. G.; Orkin, S. H. The Switch from Fetal to Adult Hemoglobin. *Cold Spring Harb. Perspect. Med.* **2013**, *3* (1), a011643.
- (80) Watson, J.; Albert, S. P.; Francis, B. P. The Significance of the Paucity of Sickle Cells in Newborn Negro Infants. *Am. J. Med. Sci.* **1948**, *215* (4), 419–423.
- (81) Akinsheye, I.; Alsultan, A.; Solovieff, N.; Ngo, D.; Baldwin, C. T.; Sebastiani, P.; Chui, D. H. K.; Steinberg, M. H. Fetal Hemoglobin in Sickle Cell Anemia. *Blood*. The American Society of Hematology July 7, 2011, pp 19–27.
- (82) Benesch, R. E.; Edalji, R.; Benesch, R.; Kwong, S. Solubilization of Hemoglobin S by Other Hemoglobins. *Proc. Natl. Acad. Sci. U. S. A.* **1980**, *77* (9 II), 5130–5134.
- (83) Lavelle, D.; Engel, J. D.; Sauntharajah, Y.; Douglas Engel, J.; Sauntharajah, Y. Fetal Hemoglobin Induction by Epigenetic Drugs. *Semin. Hematol.* **2018**, *55* (2), 60–67.
- (84) Ginder, G. D. Epigenetic Regulation of Fetal Globin Gene Expression in Adult Erythroid Cells. *Transl Res* **2015**, *165* (1), 115–125.
- (85) Koshy, H. Augmentation of Fetal Hemoglobin (HbF) Levels by Low Dose Short Duration 5-Aza-2'-Deoxycytidine (Decitabine) Administration in Sickle Cell Anemia Patients Who Had No HbF Elevation Following Hydroxyurea Therapy. *Blood* **1998**, *92* (1), 30b-30b.
- (86) Lavelle, D.; Chin, J.; Vaitkus, K.; Redkar, S.; Phiasivongsa, P.; Tang, C.; Will, R.; Hankewych, M.; Roxas, B.; Singh, M.; et al. Oral Decitabine Reactivates Expression of the Methylated γ -Globin Gene in Papio Anubis. *Am. J. Hematol.* **2007**, *82* (11), 981–985.
- (87) DeSimone, J.; Koshy, M.; Dorn, L.; Lavelle, D.; Bressler, L.; Molokie, R.; Talischy, N. Maintenance of Elevated Fetal Hemoglobin Levels by Decitabine during Dose Interval Treatment of Sickle Cell Anemia. *Blood* **2002**, *99* (11), 3905–3908.
- (88) Kutlar, A.; Ataga, K.; Reid, M.; Vichinsky, E. P.; Neumayr, L.; Blair-Britt, L.; Labotka, R.;

- Glass, J.; Keefer, J. R.; Wargin, W. A.; et al. A Phase 1/2 Trial of HQK-1001, an Oral Fetal Globin Inducer, in Sickle Cell Disease. *Am. J. Hematol.* **2012**, *87* (11), 1017–1021.
- (89) Bradner, J. E.; Mak, R.; Tanguhuri, S. K.; Mazitschek, R.; Haggarty, S. J.; Ross, K.; Chang, C. Y.; Bosco, J.; West, N.; Morse, E.; et al. Chemical Genetic Strategy Identifies Histone Deacetylase 1 (HDAC1) and HDAC2 as Therapeutic Targets in Sickle Cell Disease. *Proc. Natl. Acad. Sci.* **2010**, *107* (28), 12617–12622.
- (90) Shearstone, J. R.; Golonzhka, O.; Chonkar, A.; Tamang, D.; van Duzer, J. H.; Jones, S. S.; Jarpe, M. B. Chemical Inhibition of Histone Deacetylases 1 and 2 Induces Fetal Hemoglobin through Activation of GATA2. *PLoS One* **2016**, *11* (4), e0153767.
- (91) Chonkar, A.; Jarpe, M.; Bhol, K.; Jones, S. S.; Shearstone, J. R. The Histone Deacetylase 1 and 2 (HDAC1/2) Inhibitor ACY-957: Impact of Dosing Schedule on Pharmacokinetics (PK), Pharmacodynamics (PD), Hematopoietic Toxicity, and Gamma Globin (HBG, γ) Expression in Monkey. *Blood* **2016**, *128* (22), 323.
- (92) Atadja, P. Development of the Pan-DAC Inhibitor Panobinostat (LBH589): Successes and Challenges. *Cancer Lett.* **2009**, *280* (2), 233–241.
- (93) Moutouh-de Parseval, L. A.; Verhelle, D.; Glezer, E.; Jensen-Pergakes, K.; Ferguson, G. D.; Corral, L. G.; Morris, C. L.; Muller, G.; Brady, H.; Chan, K. Pomalidomide and Lenalidomide Regulate Erythropoiesis and Fetal Hemoglobin Production in Human CD34+ Cells. *J. Clin. Invest.* **2008**, *118* (1), 248–258.
- (94) Meiler, S. E.; Wade, M.; Kutlar, F.; Yerigenahally, S. D.; Xue, Y.; Moutouh-de Parseval, L. A.; Corral, L. G.; Swerdlow, P. S.; Kutlar, A. Pomalidomide Augments Fetal Hemoglobin Production without the Myelosuppressive Effects of Hydroxyurea in Transgenic Sickle Cell Mice. *Blood* **2011**, *118* (4), 1109–1112.

- (95) Dulmovits, B. M.; Appiah-Kubi, A. O.; Papoin, J.; Hale, J.; He, M.; Al-Abed, Y.; Didier, S.; Gould, M.; Husain-Krautter, S.; Singh, S. A.; et al. Pomalidomide Reverses γ -Globin Silencing through the Transcriptional Reprogramming of Adult Hematopoietic Progenitors. *Blood* **2016**, *127* (11), 1481–1492.
- (96) Cui, S.; Lim, K.-C.; Shi, L.; Lee, M.; Jearawiriyapaisarn, N.; Myers, G.; Campbell, A.; Harro, D.; Iwase, S.; Trievel, R. C.; et al. The LSD1 Inhibitor RN-1 Induces Fetal Hemoglobin Synthesis and Reduces Disease Pathology in Sickle Cell Mice. *Blood* **2015**, *126* (3), 386–396.
- (97) Rivers, A.; Vaitkus, K.; Ibanez, V.; Ruiz, M. A.; Jagadeeswaran, R.; Sauntharajah, Y.; Cui, S.; Engel, J. D.; DeSimone, J.; Lavelle, D. The LSD1 Inhibitor RN-1 Recapitulates the Fetal Pattern of Hemoglobin Synthesis in Baboons (*P. Anubis*). *Haematologica* **2016**, *101* (6), 688–697.
- (98) Rivers, A.; Jagadeeswaran, R.; Lavelle, D. Potential Role of LSD1 Inhibitors in the Treatment of Sickle Cell Disease: A Review of Preclinical Animal Model Data. *Am. J. Physiol. Integr. Comp. Physiol.* **2018**, *315* (4), R840–R847.
- (99) Rivers, A.; Vaitkus, K.; Ruiz, M. A.; Ibanez, V.; Jagadeeswaran, R.; Kouznetsova, T.; DeSimone, J.; Lavelle, D. RN-1, a Potent and Selective Lysine-Specific Demethylase 1 Inhibitor, Increases γ -Globin Expression, F Reticulocytes, and F Cells in a Sickle Cell Disease Mouse Model. *Exp. Hematol.* **2015**, *43* (7), 546-553.e3.
- (100) Rivers, A.; Vaitkus, K.; Jagadeeswaran, R.; Ruiz, M. A.; Ibanez, V.; Ciceri, F.; Cavalcanti, F.; Molokie, R. E.; Sauntharajah, Y.; Engel, J. D.; et al. Oral Administration of the LSD1 Inhibitor ORY-3001 Increases Fetal Hemoglobin in Sickle Cell Mice and Baboons. *Exp. Hematol.* **2018**, *67*, 60-64.e2.

- (101) Shi, L.; Cui, S.; Engel, J. D.; Tanabe, O. Lysine-Specific Demethylase 1 Is a Therapeutic Target for Fetal Hemoglobin Induction. *Nat. Med.* **2013**, *19* (3), 291–294.
- (102) Kutlar, A.; Patel, N.; Ustun, C.; Natarajan, K.; Jillella, A.; Clair, B.; Kutlar, F.; Chandler, R.; Meiler, S. E.; Bhalla, K. N. LBH589 (Panobinostat): A Potential Novel Anti-Switching Therapy. *Blood* **2009**, *114* (22), 2568–2568.
- (103) Kutlar, A.; Swerdlow, P. S.; Meiler, S. E.; Natrajan, K.; Wells, L. G.; Clair, B.; Shah, S.; Knight, R. Pomalidomide In Sickle Cell Disease: Phase I Study Of a Novel Anti-Switching Agent. *Blood* **2013**, *122* (21), 777.
- (104) Carden, M. A.; Little, J. Emerging Disease-Modifying Therapies for Sickle Cell Disease. *Haematologica* **2019**, *104* (9), 1710–1719.
- (105) Molokie, R.; Lavelle, D.; Gowhari, M.; Pacini, M.; Krauz, L.; Hassan, J.; Ibanez, V.; Ruiz, M. A.; Ng, K. P.; Woost, P.; et al. Oral Tetrahydrouridine and Decitabine for Non-Cytotoxic Epigenetic Gene Regulation in Sickle Cell Disease: A Randomized Phase 1 Study. *PLoS Med.* **2017**, *14* (9), e1002382.
- (106) Brugnara, C. Sickle Cell Disease: From Membrane Pathophysiology to Novel Therapies for Prevention of Erythrocyte Dehydration. *J. Pediatr. Hematol. Oncol.* **2003**, *25* (12), 927–933.
- (107) Franco, R. S.; Barker-Gear, R.; Green, R. Inhibition of Sickling After Reduction of Intracellular Hemoglobin Concentration With an Osmotic Pulse: Characterization of the Density and Hemoglobin Concentration Distributions . *Blood Cells* **1993**, *19* (2), 475–488.
- (108) Tosteson, D. C.; Shea, E.; darling, R. C. Potassium and Sodium of Red Blood Cells in Sickle Cell Anemia. *J. Clin. Invest.* **1952**, *31* (4), 406–411.
- (109) Gardos, G. The Role of Calcium in the Potassium Permeability of Human Erythrocytes .

- Acta Physiol. Hung.* **1959**, *15* (2), 121–125.
- (110) Eaton, J. W.; Jacob, H. S.; Skelton, T. D.; Swofford, H. S.; Kolpin, C. E. Elevated Erythrocyte Calcium in Sickle Cell Disease. *Nature* **1973**, *246* (5428), 105–106.
- (111) Brugnara, C.; De Franceschi, L.; Alper, S. L. Inhibition of Ca²⁺-Dependent K⁺ Transport and Cell Dehydration in Sickle Erythrocytes by Clotrimazole and Other Imidazole Derivatives. *J. Clin. Invest.* **1993**, *92* (1), 520–526.
- (112) Brugnara, C.; Gee, B.; Armsby, C. C.; Kurth, S.; Sakamoto, M.; Rifai, N.; Alper, S. L.; Platt, O. S. Therapy with Oral Clotrimazole Induces Inhibition of the Gardos Channel and Reduction of Erythrocyte Dehydration in Patients with Sickle Cell Disease. *J. Clin. Invest.* **1996**, *97* (5), 1227–1234.
- (113) Stocker, J. W.; De Franceschi, L.; McNaughton-Smith, G. A.; Corrocher, R.; Beuzard, Y.; Brugnara, C. ICA-17043, a Novel Gardos Channel Blocker, Prevents Sickled Red Blood Cell Dehydration in Vitro and in Vivo in SAD Mice. *Blood* **2003**, *101* (6), 2412–2418.
- (114) Ataga, K. I.; Smith, W. R.; De Castro, L. M.; Swerdlow, P.; Sauntharajah, Y.; Castro, O.; Vichinsky, E.; Kutlar, A.; Orringer, E. P.; Rigdon, G. C.; et al. Efficacy and Safety of the Gardos Channel Blocker, Senicapoc (ICA-17043), in Patients with Sickle Cell Anemia. *Blood* **2008**, *111* (8), 3991–3997.
- (115) Ataga, K. I.; Stocker, J. Senicapoc (ICA-17043): A Potential Therapy for the Prevention and Treatment of Hemolysis-Associated Complications in Sickle Cell Anemia. *Expert Opin. Investig. Drugs* **2009**, *18* (2), 231–239.
- (116) De Franceschi, L.; Bachir, D.; Galacteros, F.; Tchernia, G.; Cynober, T.; Alper, S.; Platt, O.; Beuzard, Y.; Brugnara, C. Oral Magnesium Supplements Reduce Erythrocyte Dehydration in Patients with Sickle Cell Disease. *J. Clin. Invest.* **1997**, *100* (7), 1847–1852.

- (117) Hankins, J. S.; Wynn, L. W.; Brugnara, C.; Hillery, C. A.; Li, C. S.; Wang, W. C. Phase I Study of Magnesium Pidolate in Combination with Hydroxycarbamide for Children with Sick Cell Anaemia. *Br. J. Haematol.* **2008**, *140* (1), 80–85.
- (118) Ferrone, F. A. Polymerization and Sick Cell Disease: A Molecular View. *Microcirculation* **2004**, *11* (2), 115–128.
- (119) Benesch, R. E.; Kwong, S.; Benesch, R.; Edalji, R. Location and Bond Type of Intermolecular Contacts in the Polymerisation of Haemoglobin S. *Nature* **1977**, *269* (5631), 772–775.
- (120) Dykes, G.; Crepeau, R. H.; Edelstein, S. J. Three-Dimensional Reconstruction of the Fibres of Sick Cell Haemoglobin. *Nature* **1978**, *272* (5653), 506–510.
- (121) Elbaum, D.; Nagel, R. L.; Bookchin, R. M.; Herskovits, T. T. Effect of Alkylureas on the Polymerization of Hemoglobin S. *Proc. Natl. Acad. Sci. U. S. A.* **1974**, *71* (12), 4718–4722.
- (122) Elbaum, D.; Roth, E. J.; Neumann, G.; Jaffe, E.; Bookchin, R.; Nagel, R. Molecular and Cellular Effects of Antisickling Concentrations of Alkylureas. *Blood* **1976**, *48* (2), 273–282.
- (123) Elbaum, D.; Harrington, J. P.; Bookchin, R. M.; Nagel, R. L. Kinetics of Hb S Gelation Effect of Alkylureas, Ionic Strength and Other Hemoglobins. *Biochim. Biophys. Acta - protein Struct.* **1978**, *534* (2), 228–238.
- (124) Schoenborn, B. P. Dichloromethane as an Antisickling Agent in Sick Cell Hemoglobin. *Proc. Natl. Acad. Sci. U. S. A.* **1976**, *73* (11), 4195–4199.
- (125) Poillon, W. N. Noncovalent Inhibitors of Sick Hemoglobin Gelation: Effects of Aryl-Substituted Alanines. *Biochemistry* **1400**, *21*, 1400–1406.
- (126) Behe, M. J.; Englander, S. W. Quantitative Assessment of the Noncovalent Inhibition of Sick Hemoglobin Gelation by Phenyl Derivatives and Other Known Agents. *Biochemistry*

- 1979**, *18* (19), 4196–4201.
- (127) Noguchi, C. T.; Ackerman, S.; DiMaio, J.; Schiller, P. W.; Schechter, A. N. The Effect of Phenylalanine Derivatives on the Solubility of Deoxyhemoglobin S. A Model Class of Gelation Inhibitors. *Mol. Pharmacol.* **1983**, *23* (1), 100–103.
- (128) Kumpati, J. Liposome-Loaded Phenylalanine or Tryptophan as Sickling Inhibitor: A Possible Therapy for Sickle Cell Disease. *Biochem. Med. Metab. Biol.* **1987**, *38* (2), 170–181.
- (129) Eaton, W. A.; Bunn, H. F. Treating Sickle Cell Disease by Targeting HbS Polymerization. *Blood* **2017**, *129* (20), 2719–2726.
- (130) Noguchi, C. T.; Luskey, And, K. L.; Pavone², V. Dipeptides as Inhibitors of the Gelation of Sickle Hemoglobin. *Mol. Pharmacol.* **1985**, *28*, 40–44.
- (131) Danish, E. H.; Lundgren, D. W.; Harris, J. W. Inhibition of Hemoglobin S Polymerization by N-terminal Band 3 Peptides: New Class of Inhibitors: Solubility Studies. *Am. J. Hematol.* **1994**, *47* (2), 106–112.
- (132) Olubiyi, O. O.; Olagunju, M. O.; Strodel, B. Rational Drug Design of Peptide-Based Therapies for Sickle Cell Disease. *Molecules* **2019**, *24* (24), 4551.
- (133) Oder, E.; Safo, M. K.; Abdulmalik, O.; Kato, G. J. New Developments in Anti-Sickling Agents: Can Drugs Directly Prevent the Polymerization of Sickle Haemoglobin in Vivo? *Br. J. Haematol.* **2016**, *175* (1), 24–30.
- (134) Omar, A. M.; Abdulmalik, O.; Ghatge, M. S.; Muhammad, Y. A.; Paredes, S. D.; El-Araby, M. E.; Safo, M. K. An Investigation of Structure-Activity Relationships of Azolylacryloyl Derivatives Yielded Potent and Long-Acting Hemoglobin Modulators for Reversing Erythrocyte Sickling. *Biomolecules* **2020**, *10* (11), 1508.

- (135) Beddell, C. R.; Goodford, P. J.; Kneen, G.; White, R. D.; Wilkinson, S.; Wootton, R. Substituted Benzaldehydes Designed to Increase the Oxygen Affinity of Human Haemoglobin and Inhibit the Sickling of Sickle Erythrocytes. *Br. J. Pharmacol.* **1984**, *82* (2), 397–407.
- (136) Keidan, A. J.; Sowter, M. C.; Johnson, C. S.; Marwah, S. S.; Stuart, J. Pharmacological Modification of Oxygen Affinity Improves Deformability of Deoxygenated Sickle Erythrocytes: A Possible Therapeutic Approach to Sickle Cell Disease. *Clin. Sci. (Lond)*. **1989**, *76* (4), 357–362.
- (137) Safo, M. K.; Abdulmalik, O.; Danso-Danquah, R.; Burnett, J. C.; Nokuri, S.; Joshi, G. S.; Musayev, F. N.; Asakura, T.; Abraham, D. J. Structural Basis for the Potent Antisickling Effect of a Novel Class of Five-Membered Heterocyclic Aldehydic Compounds. *J. Med. Chem.* **2004**, *47* (19), 4665–4676.
- (138) Abdulmalik, O.; Ghatge, M. S.; Musayev, F. N.; Parikh, A.; Chen, Q.; Yang, J.; Nnamani, I.; Danso-Danquah, R.; Eseonu, D. N.; Asakura, T.; et al. Crystallographic Analysis of Human Hemoglobin Elucidates the Structural Basis of the Potent and Dual Antisickling Activity of Pyridyl Derivatives of Vanillin. *Acta Crystallogr. D. Biol. Crystallogr.* **2011**, *67* (11), 920–928.
- (139) Arya, R.; Rolan, P. E.; Wootton, R.; Posner, J.; Bellingham, A. J. Tucaresol Increases Oxygen Affinity and Reduces Haemolysis in Subjects with Sickle Cell Anaemia. *Br. J. Haematol.* **1996**, *93* (4), 817–821.
- (140) Abdulmalik, O.; Safo, M. K.; Chen, Q.; Yang, J.; Brugnara, C.; Ohene-Frempong, K.; Abraham, D. J.; Asakura, T. 5-Hydroxymethyl-2-Furfural Modifies Intracellular Sickle Haemoglobin and Inhibits Sickling of Red Blood Cells. *Br. J. Haematol.* **2005**, *128* (4),

- 552–561.
- (141) Ataga, K. I.; Desai, P. C. Advances in New Drug Therapies for the Management of Sickle Cell Disease. *Expert Opin. orphan drugs* **2018**, *6* (5), 329–343.
- (142) Nnamani, I. N.; Joshi, G. S.; Danso-Danquah, R.; Abdulmalik, O.; Asakura, T.; Abraham, D. J.; Safo, M. K. Pyridyl Derivatives of Benzaldehyde as Potential Antisickling Agents. *Chem. Biodivers.* **2008**, *5* (9), 1762–1769.
- (143) Deshpande, T. M.; Pagare, P. P.; Ghatge, M. S.; Chen, Q.; Musayev, F. N.; Venitz, J.; Zhang, Y.; Abdulmalik, O.; Safo, M. K. Rational Modification of Vanillin Derivatives to Stereospecifically Destabilize Sickle Hemoglobin Polymer Formation. *Acta Crystallogr. Sect. D Struct. Biol.* **2018**, *74* (Pt 10), 956–964.
- (144) Pagare, P. P.; Ghatge, M. S.; Musayev, F. N.; Deshpande, T. M.; Chen, Q.; Braxton, C.; Kim, S.; Venitz, J.; Zhang, Y.; Abdulmalik, O.; et al. Rational Design of Pyridyl Derivatives of Vanillin for the Treatment of Sickle Cell Disease. *Bioorg. Med. Chem.* **2018**, *26*, 2530–2538.
- (145) Pagare, P. P.; Ghatge, M. S.; Chen, Q.; Musayev, F. N.; Venitz, J.; Abdulmalik, O.; Zhang, Y.; Safo, M. K. Exploration of Structure-Activity Relationship of Aromatic Aldehydes Bearing Pyridinylmethoxy-Methyl Esters as Novel Antisickling Agents. *J. Med. Chem.* **2020**, *63* (23).
- (146) Abdulmalik, O.; Pagare, P. P.; Huang, B.; Xu, G. G.; Ghatge, M. S.; Xu, X.; Chen, Q.; Anabaraonye, N.; Musayev, F. N.; Omar, A. M.; et al. VZHE-039, a Novel Antisickling Agent That Prevents Erythrocyte Sickling under Both Hypoxic and Anoxic Conditions. *Sci. Rep.* **2020**, *10* (1).
- (147) Nakagawa, A.; Lui, F. E.; Wassaf, D.; Yefidoff-Freedman, R.; Casalena, D.; Palmer, M. A.;

- Meadows, J.; Mozzarelli, A.; Ronda, L.; Abdulmalik, O.; et al. Identification of a Small Molecule That Increases Hemoglobin Oxygen Affinity and Reduces SS Erythrocyte Sickling. *ACS Chem. Biol.* **2014**, *9* (10), 2318–2325.
- (148) Nakagawa, A.; Ferrari, M.; Schleifer, G.; Cooper, M. K.; Liu, C.; Yu, B.; Berra, L.; Klings, E. S.; Safo, R. S.; Chen, Q.; et al. A Triazole Disulfide Compound Increases the Affinity of Hemoglobin for Oxygen and Reduces the Sickling of Human Sickle Cells. *Mol. Pharm.* **2018**, *15* (5), 1954–1963.
- (149) Kassa, T.; Brad Strader, M.; Nakagawa, A.; Zapol, W. M.; Alayash, A. I. Targeting Bcys93 in Hemoglobin S with an Antisickling Agent Possessing Dual Allosteric and Antioxidant Effects. *Metallomics* **2017**, *9* (9), 1260–1270.
- (150) Poillon, W. N.; Kim, B. C.; Labotka, R. J.; Hicks, C. U.; Kark, J. A. Antisickling Effects of 2,3-Diphosphoglycerate Depletion. *Blood* **1995**, *85* (11), 3289–3296.
- (151) Kalfa, T. A.; Kuypers, F. A.; Telen, M. J.; Malik, P.; Konstantinidis, D. G.; Estep, J. H.; Kim, H. J.; Saraf, S. L.; Wilson, L.; Ribadeneira, M. D.; et al. Phase 1 Single (SAD) and Multiple Ascending Dose (MAD) Studies of the Safety, Tolerability, Pharmacokinetics (PK) and Pharmacodynamics (PD) of FT-4202, an Allosteric Activator of Pyruvate Kinase-R, in Healthy and Sickle Cell Disease Subjects. *Blood* **2019**, *134* (Supplement_1), 616–616.
- (152) Reynolds, C. H. Activation of Human Erythrocyte 2,3-Bisphosphoglycerate Phosphatase at Physiological Concentrations of Substrate. *Arch. Biochem. Biophys.* **1986**, *250* (1), 106–111.
- (153) Mendz, G. L.; Kuchel, P. W. Stimulation of Human Erythrocyte 2,3-Bisphosphoglycerate Phosphatase by Vanadate. *Arch. Biochem. Biophys.* **1990**, *276*, 160–171.
- (154) Rose, Z. B.; Liebowitz, J. 2,3-Diphosphoglycerate Phosphatase from Human Erythrocytes.

- General Properties and Activation by Anions. *J. Biol. Chem.* **1970**, *245* (12), 3232–3241.
- (155) Poillon, W. N.; Robinson, M. D.; Kim, B. C. Deoxygenated Sickle Hemoglobin. Modulation of Its Solubility by 2,3-Diphosphoglycerate and Other Allosteric Polyanions. *J. Biol. Chem.* **1985**, *260* (26), 13897–13900.
- (156) Knee, K. M.; Barakat, A.; Tomlinson, L.; Ramaiah, L.; Wenzel, Z.; Kapinos, B.; Ahn, Y.; Lintner, N. G.; Field, S. D.; Jasuja, R.; et al. Sickle Cell Disease Model Mice Lacking 2,3-Dpg Show Reduced RBC Sickling and Improvements in Markers of Hemolytic Anemia. *Blood* **2020**, *136* (1), 27–28.
- (157) Fothergill-Gilmore, L. A.; Watson, H. C. The Phosphoglycerate Mutases. *Advances in enzymology and related areas of molecular biology*. John Wiley & Sons, Ltd November 22, 1989, pp 227–313.
- (158) Pritlove, D. C.; Gu, M.; Boyd, C. A. R.; Randeva, H. S.; Vatish, M. Novel Placental Expression of 2,3-Bisphosphoglycerate Mutase. *Placenta* **2006**, *27* (8), 924–927.
- (159) Garel, M.-C.; Joulin, V.; Le Boulchf, P.; Calvin, M.-C.; Prehu, M.-O.; Arous, N.; Longinll, R.; Rosa, R.; Rosa, J.; Cohen-Sola1, M. Human Bisphosphoglycerate Mutase. *J. Biol. Chem.* **1989**, *264* (32), 18966–18972.
- (160) Wang, Y.; Wei, Z.; Bian, Q.; Cheng, Z.; Wan, M.; Liu, L.; Gong, W. Crystal Structure of Human Bisphosphoglycerate Mutase. *J. Biol. Chem.* **2004**, *279*, 39132–39138.
- (161) Wang, Y.; Liu, L.; Wei, Z.; Cheng, Z.; Lin, Y.; Gong, W. Seeing the Process of Histidine Phosphorylation in Human Bisphosphoglycerate Mutase *. *J. Biol. Chem.* **2006**, *291*, 39642–39648.
- (162) Sasaki, R.; Chiba, H. Role and Induction of 2,3-Bisphosphoglycerate Synthase. *Mol. Cell. Biochem.* **1983**, *53*, 247–256.

- (163) Sasaki, R.; Ikura, K.; Sugimoto, E.; Chiba, H. Purification of Bisphosphoglyceromutase, 2, 3-Bisphosphoglycerate Phosphatase and Phosphoglyceromutase from Human Erythrocytes: Three Enzyme Activities in One Protein. *Eur. J. Biochem.* **1975**, *50* (3), 581–593.
- (164) Rosa, R.; Audit, I.; Rosa, J. Evidence for Three Enzymatic Activities in One Electrophoretic Band of 3-Phosphoglycerate Mutase from Red Cells. *Biochimie* **1975**, *57* (9), 1059–1063.
- (165) Hass, L. F.; Miller, K. B. A Reassessment of the Phosphoglycerate Bypass Enzymes in Human Erythrocytes. *Biochem. Biophys. Res. Commun.* **1975**, *66* (3), 970–979.
- (166) Rose, Z. B. The Purification and Properties of Diphosphoglycerate Mutase from Human Erythrocytes. *J. Biol. Chem.* **1968**, *243* (18), 4810–4820.
- (167) Rose, Z. B. Effects of Salts and PH on the Rate of Erythrocyte Diphosphoglycerate Mutase. *Arch. Biochem. Biophys.* **1973**, *158* (2), 903–910.
- (168) Sasaki, R.; Chiba, H. Functions and Metabolism of 2,3-Bisphosphoglycerate in Erythroid Cells. *Tanpakushitsu Kakusan Koso.* **1983**, *28* (8), 957–973.
- (169) Rosa, R.; Blouquit, Y.; Calvin, M.-C.; Promeq, D.; Promeq, J.-C.; Rosa, J. Isolation, Characterization, and Structure of a Mutant 89 Arg + Cys Bisphosphoglycerate Mutase. *J. Biol. Chem.* **1989**, *264* (14), 7837–7843.
- (170) Calvin, M. C. C.; Blouquit, Y.; Garel, M. C. C.; Prehu, M. O. O.; Cohen-Solal, M.; Rosa, J.; Rosa, R. Human Bisphosphoglycerate Mutase Expressed in E Coli: Purification, Characterization and Structure Studies. *Biochimie* **1990**, *72* (5), 337–343.
- (171) Garel, M. C.; Arous, N.; Calvin, M. C.; Craescu, C. T.; Rosa, J.; Rosa, R. A Recombinant Bisphosphoglycerate Mutase Variant with Acid-Phosphatase Homology Degrades 2,3-Diphosphoglycerate. *Proc. Natl. Acad. Sci. U. S. A.* **1994**, *91* (9), 3593–3597.
- (172) Garel, M.-C.; Lemarchandel, V.; Calvin, M.-C.; Arous, N.; Craescu, C. T.; Prehu, M.-O.;

- Rosa, J.; Rosa, R. Amino Acid Residues Involved in the Catalytic Site of Human Erythrocyte Bisphosphoglycerate Mutase. Functional Consequences of Substitutions of His10, His187 and Arg89. *Eur. J. Biochem.* **1993**, *213* (1), 493–500.
- (173) Harkness, D. R.; Thompson, W.; Roth, S.; Grayson, V. The 2,3-Diphosphoglyceric Acid Phosphatase Activity of Phosphoglyceric Acid Mutase Purified from Human Erythrocytes. *Arch. Biochem. Biophys.* **1970**, *138* (1), 208–219.
- (174) Ravel, P.; Craescu, C. T.; Arous, N.; Rosa, J.; Garel, M. C. Critical Role of Human Bisphosphoglycerate Mutase Cys 22 in the Phosphatase Activator-Binding Site*. *J. Biol. Chem.* **1997**, *272*, 14045–14050.
- (175) Rose, Z. B.; Dube, S. The Purification and Kinetic Properties of Bisphosphoglycerate Synthase from Horse Red Blood Cells. *Arch. Biochem. Biophys.* **1976**, *177* (1), 284–292.
- (176) Chu, W. T.; Zheng, Q. C.; Zhang, H. X. Insights into the Phosphatase and the Synthase Activities of Human Bisphosphoglycerate Mutase: A Quantum Mechanics/Molecular Mechanics Simulation. *Phys. Chem. Chem. Phys.* **2014**, *16* (9), 3946–3954.
- (177) Dufu, K.; Patel, M.; Oksenberg, D.; Cabrales, P. GBT440 Improves Red Blood Cell Deformability and Reduces Viscosity of Sickle Cell Blood under Deoxygenated Conditions. *Clin. Hemorheol. Microcirc.* **2018**, *70* (1), 95–105.
- (178) Poillon, W. N.; Kim, B. C.; Castro, O. Intracellular Hemoglobin S Polymerization and the Clinical Severity of Sickle Cell Anemia. *Blood* **1998**, *91* (5), 1777–1783.
- (179) Ravel, P.; Garel, M. C.; Toullec, D. New Procedures to Measure Synthase and Phosphatase Activities of Bisphosphoglycerate Mutase. Interest for Development of Therapeutic Drugs. *Comptes Rendus l'Academie des Sci. - Ser. III* **1997**, *320* (1), 27–33.
- (180) Poillon, W. N.; Kim, B. C. 2,3-Diphosphoglycerate and Intracellular PH as Interdependent

- Determinants of the Physiologic Solubility of Deoxyhemoglobin S. *Blood* **1990**, 76 (5), 1028–1036.
- (181) Rose, Z. B. A Procedure for Decreasing the Level of 2,3-Bisphosphoglycerate in Red Cells in Vitro. *Biochem. Biophys. Res. Commun.* **1976**, 73 (4), 1011–1017.
- (182) Phadke, M. Disruption of NAD + Binding Site in Glyceraldehyde 3-Phosphate Dehydrogenase Affects Its Intranuclear Interactions. *World J. Biol. Chem.* **2015**, 6 (4), 366.
- (183) Bartlett, G. R. Human Red Cell Glycolytic Intermediates*. *J. Biol. Chem.* **1958**, 234, 449–458.
- (184) Yu, K. T.; Pendley, C.; Herczeg, T.; Pendleton, R. G. 2,3-Diphosphoglycerate Phosphatase/Synthase: A Potential Target for Elevating the Diphosphoglycerate Level in Human Red Blood Cells. *J. Pharmacol. Exp. Ther.* **1990**, 252 (1), 192–200.
- (185) Rose, Z. B. The Enzymology of 2,3-Bisphosphoglycerate. *Adv. Enzymol. Relat. Areas Mol. Biol.* **1980**, 51, 211–253.
- (186) Rose, Z. B.; Salon, J. The Identification of Glycolate-2-P as a Constituent of Normal Red Blood Cells. *Biochem. Biophys. Res. Commun.* **1979**, 87 (3), 869–875.
- (187) Knight, J.; Hinsdale, M.; Holmes, R. Glycolate and 2-Phosphoglycolate Content of Tissues Measured by Ion Chromatography Coupled to Mass Spectrometry. *Anal. Biochem.* **2012**, 421 (1), 121–124.
- (188) Maveyraud, L.; Mourey, L. Protein X-Ray Crystallography and Drug Discovery. *Molecules* **2020**, 25 (1030).
- (189) Cherfilsl, J.; Rosa', R.; Garel, M.-C.; Calvin, M.-C.; Rosa, J.; Janin', J. Crystallization and Preliminary X-Ray Diffraction Studies of the Human Erythrocyte Bisphosphoglycerate Mutase. *J. Mol. Biol.* **1991**, 218 (2), 269–270.

- (190) Patterson, A.; Price, N. C.; Nairn, J. Unliganded Structure of Human Bisphosphoglycerate Mutase Reveals Side-Chain Movements Induced by Ligand Binding. *Struct. Biol. Cryst. Commun.* **2010**, *66*, 1415–1420.
- (191) Högman, C. F.; Knutson, F.; Lööf, H.; Payrat, J. M. Improved Maintenance of 2,3 DPG and ATP in RBCs Stored in a Modified Additive Solution. *Transfusion* **2002**, *42* (7), 824–829.
- (192) Venturas, F.; Rosa, J. L.; Ambrosio, S.; Pilkis, S. J.; Bartronsll, R. Bovine Brain 6-Phosphofructo-2-Kinase/Fructose-2,6-Bisphosphatase EVIDENCE FOR A NEURAL-SPECIFIC ISOZYME*. *J. Biol. Chem.* **1992**, *267* (25), 17939–17943.
- (193) Wang, Y.; Wei, Z.; Liu, L.; Cheng, Z.; Lin, Y.; Ji, F.; Gong, W. Crystal Structure of Human B-Type Phosphoglycerate Mutase Bound with Citrate. *Biochem. Biophys. Res. Commun.* **2005**, *331* (4), 1207–1215.
- (194) Winn, M. D.; Ballard, C. C.; Cowtan, K. D.; Dodson, E. J.; Emsley, P.; Evans, P. R.; Keegan, R. M.; Krissinel, E. B.; Leslie, A. G. W.; McCoy, A.; et al. Overview of the CCP4 Suite and Current Developments. *Acta Crystallogr. Sect. D Biol. Crystallogr.* **2011**, *67* (4), 235–242.
- (195) Echols, N.; Grosse-Kunstleve, R. W.; Afonine, P. V.; Bunkóczi, G.; Chen, V. B.; Headd, J. J.; McCoy, A. J.; Moriarty, N. W.; Read, R. J.; Richardson, D. C.; et al. Graphical Tools for Macromolecular Crystallography in PHENIX. *J. Appl. Crystallogr.* **2012**, *45* (3), 581–586.
- (196) Emsley, P.; Cowtan, K. Coot: Model-Building Tools for Molecular Graphics. *Acta Crystallogr. Sect. D Biol. Crystallogr.* **2004**, *60* (12 I), 2126–2132.
- (197) Afonine, P. V.; Grosse-Kunstleve, R. W.; Echols, N.; Headd, J. J.; Moriarty, N. W.; Mustyakimov, M.; Terwilliger, T. C.; Urzhumtsev, A.; Zwart, P. H.; Adams, P. D. Towards

- Automated Crystallographic Structure Refinement with Phenix.Refine. *Acta Crystallogr. Sect. D Biol. Crystallogr.* **2012**, *68* (4), 352–367.
- (198) Brenke, R.; Kozakov, D.; Chuang, G. Y.; Beglov, D.; Hall, D.; Landon, M. R.; Mattos, C.; Vajda, S. Fragment-Based Identification of Druggable “hot Spots” of Proteins Using Fourier Domain Correlation Techniques. *Bioinformatics* **2009**, *25* (5), 621–627.
- (199) Kozakov, D.; Grove, L. E.; Hall, D. R.; Bohnuud, T.; Mottarella, S. E.; Luo, L.; Xia, B.; Beglov, D.; Vajda, S. The FTMap Family of Web Servers for Determining and Characterizing Ligand-Binding Hot Spots of Proteins. *Nat. Protoc.* **2015**, *10* (5), 733–755.
- (200) Kozakov, D.; Hall, D. R.; Napoleon, R. L.; Yueh, C.; Whitty, A.; Vajda, S. New Frontiers in Druggability. *Journal of Medicinal Chemistry*. American Chemical Society December 10, 2015, pp 9063–9088.
- (201) Winn, S. I.; Watson, H. C.; Harkins, R. N.; Fothergill, L. A. Structure and Activity of Phosphoglycerate Mutase. *R. Soc.* **1981**, *293*, 121–130.
- (202) Liu, S. E.; Hu, J. C.; Zhang, H.; Xu, P.; Wan, W.; Zheng, M. Y.; Yu, K. Q.; Ding, H.; Jiang, H. L.; Zhou, L.; et al. Conformation and Dynamics of the C-Terminal Region in Human Phosphoglycerate Mutase 1. *Acta Pharmacol. Sin.* **2017**, *38* (12), 1673–1682.
- (203) Rose, Z. B.; Dube, S. Phosphoglycerate Mutase. Kinetics and Effects of Salts on the Mutase and Bisphosphoglycerate Phosphatase Activities of the Enzyme from Chicken Breast Muscle. *J. Biol. Chem.* **1978**, *253* (23), 8583–8592.
- (204) Levitzki, A.; Stallcup, W. B.; Koshland, D. E. Half-of-the-Sites Reactivity and the Conformational States of Cytidine Triphosphate Synthetase. *Biochemistry* **1971**, *10* (18), 3371–3378.
- (205) Hurst, T. Flexible 3D Searching: The Directed Tweak Technique. *J. Chem. Inf. Comput. Sci*

- 1994**, 34, 190–196.
- (206) Chang, C.; Ekins, S.; Bahadduri, P.; Swaan, P. W. Pharmacophore-Based Discovery of Ligands for Drug Transporters. *Adv. Drug Deliv. Rev.* **2006**, 58 (12–13), 1431–1450.
- (207) Kim, K.-H.; Kim, N. D.; Seong, B.-L. Pharmacophore-Based Virtual Screening: A Review of Recent Applications. *Expert Opin. Drug Discov.* **2010**, 5 (3), 205–222.
- (208) Lipinski, C. A. Lead- and Drug-like Compounds: The Rule-of-Five Revolution. *Drug Discovery Today: Technologies*. Elsevier December 1, 2004, pp 337–341.
- (209) Jones, G.; Willett, P.; Glen, R. C.; Leach, A. R.; Taylor, R. Development and Validation of a Genetic Algorithm for Flexible Docking. *J. Mol. Biol.* **1997**, 267 (3), 727–748.
- (210) Jones, G.; Willett, P.; Glen, R. C. Molecular Recognition of Receptor Sites Using a Genetic Algorithm with a Description of Desolvation. *J. Mol. Biol.* **1995**, 245 (1), 43–53.
- (211) Hopkins, A. L.; Groom, C. R.; Alex, A. Ligand Efficiency: A Useful Metric for Lead Selection. *Drug Discovery Today*. Elsevier Ltd May 15, 2004, pp 430–431.
- (212) Hopkins, A. L.; Keserü, G. M.; Leeson, P. D.; Rees, D. C.; Reynolds, C. H. The Role of Ligand Efficiency Metrics in Drug Discovery. *Nat. Rev. Drug Discov.* **2014**, 13 (2), 105–121.
- (213) Wallach, I.; Dzamba, M.; Heifets, A. *AtomNet: A Deep Convolutional Neural Network for Bioactivity Prediction in Structure-Based Drug Discovery*; 2015.
- (214) Hitosugi, T.; Zhou, L.; Elf, S.; Fan, J.; Kang, H. B.; Seo, J. H.; Shan, C.; Dai, Q.; Zhang, L.; Xie, J.; et al. Phosphoglycerate Mutase 1 Coordinates Glycolysis and Biosynthesis to Promote Tumor Growth. *Cancer Cell* **2012**, 22 (5), 585–600.
- (215) Friesner, R. A.; Banks, J. L.; Murphy, R. B.; Halgren, T. A.; Klicic, J. J.; Mainz, D. T.; Repasky, M. P.; Knoll, E. H.; Shelley, M.; Perry, J. K.; et al. Glide: A New Approach for

- Rapid, Accurate Docking and Scoring. 1. Method and Assessment of Docking Accuracy. *J. Med. Chem.* **2004**, 47 (7), 1739–1749.
- (216) Halgren, T. A.; Murphy, R. B.; Friesner, R. A.; Beard, H. S.; Frye, L. L.; Pollard, W. T.; Banks, J. L. Glide: A New Approach for Rapid, Accurate Docking and Scoring. 2. Enrichment Factors in Database Screening. *J. Med. Chem.* **2004**, 47 (7), 1750–1759.
- (217) Bowers, K. J.; Bowers, K. J.; Chow, E.; Xu, H.; Dror, R. O.; Eastwood, M. P.; Gregersen, B. A.; Klepeis, J. L.; Kolossvary, I.; Moraes, M. A.; et al. Scalable Algorithms for Molecular Dynamics Simulations on Commodity Clusters. In *Proceedings of the 2006 ACM/IEEE Conference on Supercomputing* ; Tampa, 2006; pp 11–17.

Vita

Anfal S. Aljhdali was born on September 10, 1989, in Jeddah, Saudi Arabia. She received her Doctor of pharmacy (PharmD.) degree from King Abdulaziz University, Saudi Arabia in 2013. She joined the Medicinal Chemistry department in the School of Pharmacy at Virginia Commonwealth University in August 2015.

